Università degli Studi di Trieste

Dipartimento di Fisica

Corso di Laurea Magistrale in Fisica

Caratterizzazione approfondita di sensori al diamante per un aggiornamento del monitor di radiazione di Belle II

Candidato:
Alice Gabrielli

Relatore:
Prof. Lorenzo Vitale

Corelatore:
Dott. Mirco Dorigo

ANNO ACCADEMICO 2019–2020

Università degli Studi di Trieste

Dipartimento di Fisica

Corso di Laurea Magistrale in Fisica

In-depth characterization of diamond sensors for an update of the Belle II radiation monitor

Candidato:
Alice Gabrielli

Relatore:
Prof. Lorenzo Vitale

Corelatore:
Dott. Mirco Dorigo

ANNO ACCADEMICO 2019–2020

Sommario

Questo lavoro di tesi mira ad approfondire e migliorare i metodi di caratterizzazione di sensori al diamante, in vista di un aggiornamento del monitor di radiazione dell'esperimento di fisica delle particelle Belle II. Sono state utilizzate tre diverse sorgenti di radiazione: una sorgente α, una sorgente β e una sorgente di raggi X, quest'ultima utilizzata per la prima volta a questo scopo. Per caratterizzare la risposta dei diamanti a radiazione β e X, ho adottato un nuovo metodo che prevede l'uso di un diodo al silicio come rivelatore di riferimento, in modo da minimizzare le incertezze sistematiche legate alla scarsa conoscenza della sorgente di radiazione usata. Nella caratterizzazione con le particelle α, ho migliorato la simulazione dell'apparato sperimentale rispetto a quella precedentemente usata. I risultati che ho ottenuto rappresentano un importante passo in avanti nelle tecniche di caratterizzazione dei sensori al diamante da usare per l'aggiornamento del monitor di radiazione.

Abstract

This thesis aims at deepening and improving the methods to characterise the response of diamond detectors in view of an upgrade of the radiation monitor of the Belle II particle-physics experiment. Three types of radiation are used: α and β particles, and, for the first time in this kind of characterisation, X-rays. I employed a novel method to characterise the diamond-sensor response to β and X radiation, which exploits a silicon diode as a reference to minimise systematic uncertainties due to the poor knowledge of the radiation sources. I improved the simulation of the experimental setup over that previously used in the characterisation with α radiation. The results that I obtained represent important steps forward in the characterisation techniques for diamond sensors to be used for the radiation-monitor upgrade.

Contents

Introduction

The goal of my experimental particle-physics thesis is to deepen and improve the methods to characterise the response of diamond detectors in view of a forthcoming upgrade of the Belle II radiation monitor.

Belle II is a particle-physics experiment that studies electron-positron collisions produced by the SuperKEKB collider in Japan. It targets to measure with high precision the properties and the dynamic of the heavy quarks and the tau lepton. In the next decade, Belle II will be at the forefront of the intensity frontier, the experimental effort to accurately test the standard model of particle physics for discovering an anomaly that would signal unexpected physics. It will contribute to the search for new physics at colliders, a chief target of the high-energy physics community, complementing the effort at the Large-Hadron-Collider experiments.

The heart of Belle II is a state-of-the-art silicon vertex detector that finely samples the trajectories of charged particles. To keep good performances, essential for a successful physics programme, the silicon detector must operate in an environment with minimal high-radiation backgrounds from the accelerator. The SuperKEKB accelerator, a new-generation high-luminosity asymmetric e^+e^- collider, is supposed to reach the unprecedented peak luminosity of $8 \times 10^{35}\,\mathrm{cm}^{-2}\mathrm{s}^{-1}$, 40 times larger than that of its predecessor. On June 15th, the record luminosity of $2.22 \times 10^{34}\,\mathrm{cm}^{-2}\mathrm{s}^{-1}$, the world's highest value ever obtained from any collider, has been achieved, and the machine is keeping the pace toward the design value. High beam-intensities are needed to reach such luminosities, and as a drawback high-radiation backgrounds, which could permanently damage the silicon detector, are generated. In order to protect the detector, a system based on single-crystal artificial-diamond sensors has been designed, developed, and installed by the Belle II Trieste group. This system monitors the radiation doses near the interaction region, triggering protective actions when needed. It has been proving itself pivotal for a safe achievement of the excellent performance of the accelerator. Profiting from a long shut-down in 2022 to install a inner layer of the silicon detector, the Belle II collaboration intends to update the monitor system to increase the acceptance, such that additional regions of the detectors can be covered. Between eight and ten new diamond sensors must be assembled, characterised and installed.

My thesis consists of a preparatory work for the upgrade of the monitor system. In this work, I perform a in-depth characterisation of four diamond sensors similar to those employed in the monitor system. I test the response of these sensors and I compare the measurements with dedicated simulations. Three types of radiation are used: α and β particles, and, for the first time in this kind of characterisation, X-rays. With α radiation, I analyse the transport proprieties of charge carriers inside the diamond bulk, and I estimate the average energy to create an electron-hole pair. A constant flux of β and X radiation is used to test the stability of the output current from the sensor and to check hysteresis effects that are typical of diamond sensors. Finally, I employed a novel method, which involves the use of a silicon diode as a reference, to infer information on the specific feature of each diamond sensor, such as the photoconductive gain. This method allows to suppress uncertainties due to the poor knowledge of the radiation source.

The thesis is organised as follows. Chapter 1 gives a brief overview of the flavour sector of the standard model. Chapter 2 describes the SuperKEKB accelerator and the detectors of the Belle II experiment. In Chapter 3, the beam-induced background, its potential damage on the silicon detector, and the monitor systems are detailed. It also describes diamond-sensor features and the specific sensor characterised in this work. Chapter 4 reports the first type of characterisation, that using α radiation. In Chapter 5 the study with the β radiation is described. Chapter 6 details the characterisation with the X radiation. A summary of the results of the characterisations is given in Chapter 7, and a conclusion is drawn at the end of the document.

Chapter 1

Flavor physics to test the standard model

This chapter presents a brief overview of the standard model of particle physics, with a particular focus on the quark sector. The role of quark-flavour physics in the search for new physics is also shortly outlined.

1.1 An overview of the standard model of particle physics

Particle physics aims to explain the laws of Nature at its most fundamental level, *i.e.* the elementary particles and their interactions through the four fundamental forces summarized in Table 1.1. The standard model (SM) of particle physics is, at the current level of experimental precision, the best-tested theory of Nature at this fundamental level [1]. It is a gauge quantum field theory which includes three of the four fundamental forces: the strong, the electromagnetic, and weak force; indeed, at the energy scale probed so far, the gravitational force can be fully neglected.

The strong interaction is described by Quantum Chromodynamics (QCD) and characterized by a *color* charge of three different kinds. The mediators of this interaction are massless spin-1 bosons called gluons (g), which carry a combination of two color charges in eight different states. The electromagnetic interaction instead has two kinds of charge and is mediated by a massless spin-1 boson called photon (γ), which does not carry any charge. Finally, the weak interaction features three massive mediators, which are the two electrically charges bosons $W^{\pm}$ and the neutral boson Z^0.

Force	Strength	Gauge boson		Spin
Strong	1	Gluon	g	1
Electromagnetic	1/137	Photon	γ	1
Weak	10^{-8}	W boson	$W^{\pm}$	1
		Z boson	Z^0	1
Gravity	10^{-37}	Graviton?	G	2

Table 1.1: Summary of the four fundamental forces. The SM describes the first three: the strong, the electromagnetic, and the weak force. The strength is obtained comparing the forces at the proton mass scale.

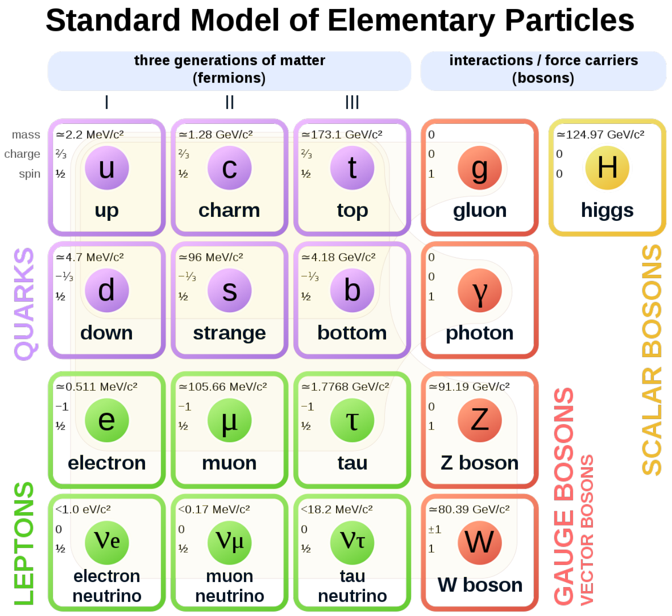

Figure 1.1: A schematic representation of the particles in the SM.

The SM is based on the symmetry group [2]

$$SU(3)_C \otimes SU(2)_L \otimes U(1)_Y \,,$$

where C stands for the color charge, L for the left-handed chirality and Y for the hypercharge. The fundamental matter particles, quarks and leptons, are represented by spin-$\frac{1}{2}$ fermion fields which transform under the symmetry group above and carry different charges. To each fermion corresponds an antiparticle with opposite charges. The gauge generators of the symmetry group are the bosons, mediators of the forces. The $SU(3)_C$ group have 8 generators that correspond to the gluons. The generators of the $SU(2)_L$ and $U(1)_Y$ groups are $W_{1,2,3}$ and the B, and the weak- and electromagnetic-force mediators are obtained through their linear combinations

$$W^{\pm} = \frac{1}{\sqrt{2}}(W_1 \mp iW_2)\,, \tag{1.1}$$

$$\begin{pmatrix} \gamma \\ Z^0 \end{pmatrix} = \begin{pmatrix} \cos\theta_{\mathrm{W}} & \sin\theta_{\mathrm{W}} \\ -\sin\theta_{\mathrm{W}} & \cos\theta_{\mathrm{W}} \end{pmatrix} \begin{pmatrix} B \\ W_3 \end{pmatrix}\,, \tag{1.2}$$

where θ_{W} is the Weinberg angle, or weak mixing angle. This mixing angle is related to the spontaneous breaking of the $SU(2)_L \otimes U(1)_Y$ symmetry, a mechanism related to the Higgs field that gives mass to the gauge bosons. The Higgs field is mediated by a spin-1 neutral boson (H). Fermion masses are generated by the coupling between the fermion fields and the Higgs field, named Yukawa coupling.

Quarks and leptons have a quantum number called *flavor*, which is conserved in strong and electromagnetic interactions but not in weak interactions. In the SM, there are six flavours of quarks and six flavours of leptons. The six flavours are split into three generations (or families), both for quarks and leptons, which are made of doublets of the weak isospin. The three generations of quarks are

$$\begin{pmatrix} u \\ d \end{pmatrix}, \begin{pmatrix} c \\ s \end{pmatrix}, \begin{pmatrix} t \\ b \end{pmatrix}.$$

Each weak-isospin doublet comprises an up-type quark with electric charge $+\frac{2}{3}e$ and a down-type quark with electric charge $-\frac{1}{3}e$, and couples to all interactions. Since only quarks carry the color charge, only the quarks feel the strong interaction. However, because of the nature of the QCD interaction, quarks are never observed as free particles, but are always confined to bounded states, called hadrons. The bound state of a quark and an anti-quark is called a *meson*, and that composed of three quarks (or three antiquarks) is called a *baryon*.

The three generations of leptons are

$$\begin{pmatrix} e \\ \nu_e \end{pmatrix}, \begin{pmatrix} \mu \\ \nu_\mu \end{pmatrix}, \begin{pmatrix} \tau \\ \nu_\tau \end{pmatrix},$$

each one composed of a weak-isospin doublet with a massive and negative charged lepton and a massless and neutral neutrino. Neutrinos couple only to the electroweak interaction. Each lepton has a quantum number called lepton family number, which is conserved in all SM processes (but not in neutrino oscillations). The sum of all these quantum numbers, *i.e.* the total lepton number, is also conserved in the SM.

Although the term “flavor physics” usually refers to the physics of both quarks and leptons, in what follows I will restrict the scope by referring solely to the quark interactions.

1.2 Charge-Parity violation and the CKM matrix

Symmetries are central to our current understanding of particle physics. Gauge symmetry is one of the base concepts of the SM structure. In addition, discrete symmetries are also relevant in the SM phenomenology. The SM has three related discrete symmetries:

- parity tranformation ($\mathcal{P}$) is the spatial inversion through the origin;
- charge conjugation ($\mathcal{C}$) transforms a particle into its antiparticle;
- time reversal ($\mathcal{T}$) inverts the direction of time.

The combination of these three symmetries is always conserved, *i.e.* the application of all three transformations do not change the laws of physics. Instead, each single transformation is found to be violated. The $\mathcal{P}$ symmetry is maximally violated in the weak interactions, while the combined $\mathcal{CP}$ [3–5] symmetry is violated by weak interactions only at the 0.1% level. The violation of the $\mathcal{CP}$ symmetry is also one of the fundamental conditions to generate the baryon-antibaryon asymmetry that leads to a matter dominated Universe.

The violation of the $\mathcal{CP}$ symmetry was first observed in 1964 [6], by Cronin and Fitch in the neutral kaon system. The understanding of the origin of $\mathcal{CP}$ violation had a pivotal role in the development of the quark sector of the SM. Indeed, the only place where $\mathcal{CP}$ violating effects can be accommodated in the SM is in the weak interaction of quarks. This was discovered between the ’60 and the ’70 of the last century. In 1963 Cabibbo [7] suggested the mixing between down-type quarks of the first two families, the d and s quarks, to preserve the universality of weak interaction, by introducing the Cabibbo mixing angle θ_c. At that time, only u, d and s quarks were known. The quark mixing can be represented by a 2×2 unitary real matrix , with the Cabibbo angle as the single parameter. However, to allow for $\mathcal{CP}$ violation, the quark-mixing matrix has to contain complex elements, satisfying the relation $V_{ij} \neq V_{ij}^{*}$, and this requires at least three families of quarks. In 1973, Kobayashi and Maskawa [8] suggested that the existence of a third generation of quarks could explain the observed $\mathcal{CP}$ violation. The 4^{th} quark, the charm quark c completing the quark pair of the second family, was only discovered a year later, in 1974, in the bounded state of the J/ψ resonance, although its prediction dates back in 1970 when Glashow, Illiopulos and Maiani postuled its existence to explain the suppressed rate of the $K^0 \to \mu^+\mu^-$ decay. The bottom quark b, the down-type quark of the third family, and the top quark t completing this family, were discovered in 1977 and 1994, respectively. In 2008, Kobayashi and Maskawa were awarded the Nobel prize for the understanding of the origin of $\mathcal{CP}$ violation, which predicts the existence of at least three families of quarks in Nature.

In the SM, the weak interactions of quarks are described in terms of the unitary Cabibbo-Kobayashi-Maskawa (CKM) matrix. The weak eigenstates are related to the mass (flavor) eigenstates by

$$\begin{pmatrix} d' \\ s' \\ b' \end{pmatrix} = \begin{pmatrix} V_{ud} & V_{us} & V_{ub} \\ V_{cd} & V_{cs} & V_{cb} \\ V_{td} & V_{ts} & V_{tb} \end{pmatrix} \begin{pmatrix} d \\ s \\ b \end{pmatrix} . \tag{1.3}$$

With three generations, there are four free parameters: three Euler angles θ_{12}, θ_{23} and θ_{13} and a complex phase δ. This last parameter allows for the presence of $\mathcal{CP}$ violation. The off-diagonal terms in the CKM matrix are relative small. This implies that the rotation angles between the flavor eigenstates and the weak eigenstates are also small, and the the matrix has a near diagonal form. Consequently, the weak interactions of quarks of different generations are suppressed relative to those of the same generation. Therefore, it is convenient to express the matrix as an expansion in a relative small parameter, $\lambda = \sin\theta_c = 0.225$, where θ_c is the Cabibbo angle. Using the Wolfenstein parametrisation, in terms of four real parameters, λ, A, ρ and η, the CKM matrix up to order $\mathcal{O}(\lambda^3)$ can be written as

$$\begin{pmatrix} V_{ud} & V_{us} & V_{ub} \\ V_{cd} & V_{cs} & V_{cb} \\ V_{td} & V_{ts} & V_{tb} \end{pmatrix} = \begin{pmatrix} 1-\frac{\lambda^2}{2} & \lambda & A\lambda^3(\rho - i\eta) \\ -\lambda & 1-\frac{\lambda^2}{2} & A\lambda^2 \\ A\lambda^3(1-\rho-i\eta) & -A\lambda^2 & 1 \end{pmatrix} . \tag{1.4}$$

For $\mathcal{CP}$ to be violated, η must be non-zero.

The CKM matrix is unitary, which implies that $V_{\text{CKM}}^{\dagger} V_{\text{CKM}} = \mathbb{1}$and leads to the following relations:

$$\begin{array}{rcc} |V_{ud}|^2 + |V_{cd}|^2 + |V_{td}|^2 = 1 & V_{us}^* V_{ud} + V_{cs}^* V_{cd} + V_{ts}^* V_{td} = 0 & V_{ud} V_{cd}^* + V_{us} V_{cs}^* + V_{ub} V_{cb}^* = 0 \ , \\ |V_{us}|^2 + |V_{cs}|^2 + |V_{ts}|^2 = 1 & V_{ub}^* V_{ud} + V_{cb}^* V_{cd} + V_{tb}^* V_{td} = 0 & V_{ud} V_{td}^* + V_{us} V_{ts}^* + V_{ub} V_{tb}^* = 0 \ , \\ |V_{ub}|^2 + |V_{cb}|^2 + |V_{tb}|^2 = 1 & V_{ub}^* V_{us} + V_{cb}^* V_{cs} + V_{tb}^* V_{ts} = 0 & V_{cd} V_{td}^* + V_{cs} V_{ts}^* + V_{cb} V_{tb}^* = 0 \ . \end{array}$$

The six vanishing combinations can be represented as a triangle in a complex plane, each triangle with the same area. The most commonly used unitary triangle is given by

$$V_{ub}^* V_{ud} + V_{cb}^* V_{cd} + V_{tb}^* V_{td} = 0 \, . \tag{1.5}$$

Figure 1.2 shows the triangle with the sides normalised to $V_{cb}^* V_{cd}$. The angle of the unitarity triangle are

$$\phi_1 = \beta \equiv \arg\left(\frac{V_{td}^* V_{tb}}{V_{cd}^* V_{cb}}\right), \ \phi_2 = \alpha \equiv \arg\left(\frac{V_{ud}^* V_{ub}}{V_{td}^* V_{tb}}\right), \ \phi_3 = \gamma \equiv \arg\left(\frac{V_{cd}^* V_{cb}}{V_{ud}^* V_{ub}}\right),$$

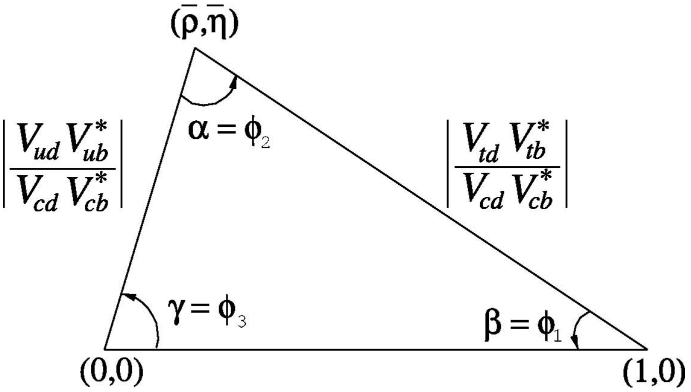

Figure 1.2: Unitarity triangle.

which are convention independent, since any phase added to a specific quark field or any rotation of the triangle do not affect them.

Experimentally, the unitarity triangle can be over-constrained by multiple, redundant measurements of its sides and angles, exploiting processes involving different amplitudes of weak decays of mesons and baryons. The consistency of the CKM mechanism implies that all measurements must agree and result in the same values of the apex of the unitarity triangle. The current status is presented on the left-hand side of Fig. 1.3: at the current level of precision, the CKM paradigm provides an excellent description of all measurements represented as confidence regions which overlap at $\bar\rho + i\bar\eta = -V_{ud}^* V_{ub}/(V_{cd}^* V_{cb})$.

1.3 New physics search through flavour physics

Despite this extraordinary accuracy of the CKM description, there is still room for inconsistencies at 10-15% level with the current precision. If deviations are found by decreasing the uncertainties of the different measurements, this might signal the existence of processes beyond the SM not accounted for by the CKM mechanism. In this respect, quark-flavour processes are used as an indirect probe of new physics.

To increase the reach of this indirect search, it is necessary to improve over current measurements, which are, for the major part, limited by the statistical uncertainty. To give an idea of the possible reach, on the right-hand side of Fig. 1.3, a plot shows the unitarity triangle as obtained from simulated measurements exploiting the full Belle II

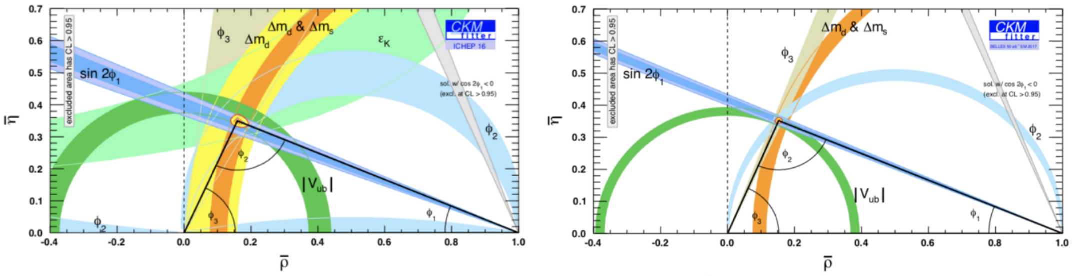

Figure 1.3: The current constrains on the values of CKM Unitary Triangle [9] (right) and the ones extrapolated to the 50 ab^{-1} luminosity for an SM-like scenario [10].

data set at the end of the foreseen experiment operations, which is expected to overpass by 50 times the sample collected by Belle, its predecessor. The improvement over the current status, showed in the left-hand side of the figure, is striking. In addition, along with Belle II, the upgraded LHCb experiment [11] is expected to contribute in this sector from early 2022.

Belle II and LHCb are the two major experiments that are expected to lead the experimental endeavour in the heavy flavour sector. One feature that make Belle II attractive and complementary to the LHCb experiment is the much lower background produced at lepton colliders with respect to hadron colliders, implying lower track multiplicity and detector occupancy, and better spatial resolution of neutral particle detectors, with flavor tagging of more than one neutral particle. In addition, the kinematic constrains on the initial states due to the point-like nature of the colliding particles, leads to an higher reconstruction efficiencies for decays with missing energy.

Search for new physics is a chief target of high-energy experiments nowadays. Even if the SM is one of the best verified physics theories, many fundamental questions remain unanswered within this model. Just to mention one open issue, the observed $\mathcal{CP}$ violation within the quark sector that originates from the complex phase of the CKM matrix is many orders of magnitude too small to explain the dominance of matter in the universe. Hence, there must exist undiscovered sources of the $\mathcal{CP}$ asymmetry responsible for a matter-dominated Universe.

The indirect searches carried out at the Belle II or LHCb experiments complement the direct searches at the energy frontier. At the energy frontier, new particles are searched by exploring new energy scale, *i.e.* by increasing the centre-of-mass energy of particle colliders. An example of this approach is given by the Large Hadron Collider (LHC), where proton–proton collisions at a centre-of mass energy of 13 TeV, the largest value of energy achieved so far, are produced. Experiments at the LHC like CMS and ATLAS search for the direct production of new physics, whose sensitivity depends on the cross section of the new particles at the energy produced in the proton-proton collisions. These searched have excluded large portions of the parameter space for several proposed SM extensions up to energies of a few TeV, and showed no conclusive evidence of non-SM physics so far. On the contrary, the sensitivity of the indirect approach to NP is not limited by the energy produced in the laboratory, but depends on the strength of the flavor-violating couplings of the NP. The mass reach for a new particle or process can be as high as $\mathcal{O}(100\,\mathrm{TeV})$ if the couplings are not as suppressed as in the SM. Since different plans for a higher-energy collider in the near future are still under developments, indirect searched for new physics through flavor physics emerges as a very promising asset to search for non-SM physics in the next decade. In this respect, the Belle II experiment, which is described in detail in the next chapter, will play a key role.

Chapter 2

Belle II experiment

This chapter outlines the main features of the Belle II experiment at the SuperKEKB accelerator.

2.1 The SuperKEKB collider

SuperKEKB is a high-luminosity electron-positron (e^+e^-) energy-asymmetric collider [12], designed to produce nearly 1000 $B\overline{B}$ pairs ($B^0\overline{B^0}$ and B^+B^- in approximately equal proportions) per second via decays of $\Upsilon(4S)$ mesons produced at threshold. Such colliders are called "B-factories", and were proposed in the 1990's for $\mathcal{CP}$-violation measurements in B mesons. The main goal of B-factories is to produce low-background quantum-correlated $B\overline{B}$ pairs at high rates.

Intense beams of electrons and positrons are brought to collision at the energy corresponding to the $\Upsilon(4S)$ meson mass, which is just above the $B\overline{B}$ production kinematic threshold. Such finely tuned collision energy is key. The enhancement in production rate of $\Upsilon(4S)$ mesons, which decay in $B\overline{B}$ pairs 96% of the times with little available energy to produce additional particles, suppresses backgrounds, which are mainly due to competing non-resonant hadron production. In addition, beams of point-like particles allow knowing precisely the collision energy, which sets stringent constraints on the final-state kinematic properties, resulting in further background suppression. Since bottom mesons are produced in a strong-interaction decay, flavor is conserved, and the null net bottom content of the initial state implies production of a $B\overline{B}$ pair, which has null net bottom flavor; even though B^0 and $\overline{B^0}$ undergo flavor oscillations, their time-evolution is quantum-correlated in such a way that no B^0B^0 or $\overline{B^0B^0}$ pairs are present at any time. In fact, angular-momentum conservation implies that the decay of a spin-1 meson in two spin-0 mesons yields final states with total angular momentum L=1. Because the simultaneous presence of two identical particles in an antisymmetric state would violate Bose statistics, the system evolves coherently as an oscillating $B^0\overline{B^0}$ particle-antiparticle pair until either one decays. This allows identification of the bottom (or antibottom) content of one meson at the time of decay of the other, if the latter decays in a final state accessible only by either bottom or antibottom states (flavor-specific decay). This feature is called "flavor tagging" and is fundamental because it allows measurements of flavor-dependent decay rates, as needed in determinations of $\mathcal{CP}$-violating quantities. Not just $\Upsilon(4S)$ mesons are produced in 10 GeV e^+e^- collisions; Figure 2.1 shows the hadron-production cross-section in e^+ e^- collisions as a function of the final-state mass. The various peaks are excitations of the Υ meson and the nearly uniform baseline at $\approx 4\,\text{nb}$ represents the so-called continuum ($e^+e^- \to q\overline{q}$) production, which exceeds $\Upsilon(4S)$ production in rate.

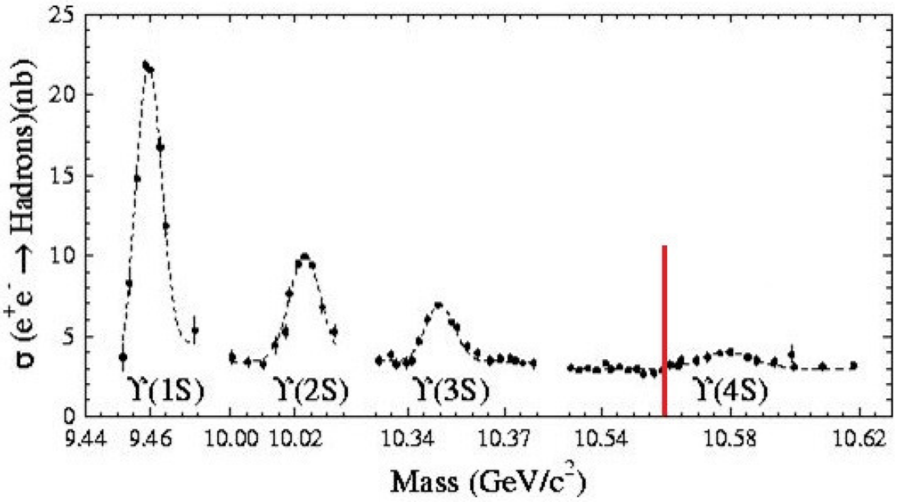

Figure 2.1: Hadron production cross section from e^+e^- collisions as a function of the final-state mass.

Because the $\Upsilon(4S)$ mesons are produced at threshold, in an energy-symmetric collider they would be nearly at rest in the laboratory frame. Hence, the resulting B mesons would too be produced with low momentum ($\approx 10\,\mathrm{MeV}/c$) in the laboratory, because of the $21\,\mathrm{MeV}/c^2$ difference between $\Upsilon(4S)$ and $B\overline{B}$ pair masses. With such low momenta they would travel approximately $1\,\mu$m before decaying. The 10 μm typical spatial resolution of vertex detectors would not be sufficient to separate B-decay vertices and study the decay time evolution for measurements involving mixing. Asymmetric beam energies are used to circumvent this limitation, because they boost the collision center-of-mass along the beam in the laboratory frame, thus achieving B-decay vertices separation. SuperKEKB (Fig. 2.3) implements a 7-4 GeV energy-asymmetric double-ring design, which achieves a vertex displacement of about 150 µm. SuperKEKB is designed to reach, by 2025, $50\,\mathrm{ab}^{-1}$ of integrated luminosity, corresponding $\approx 5.28 \times 10^{10}$ $B\overline{B}$ pairs, about 40 times the amount collected by its predecessor KEKB.

Electrons are produced via photoelectric effect by targeting a cold cathode with a pulsed laser, then accelerated to 7 GeV with a linear accelerator (Linac) and injected in the High-Energy Ring (HER). Positrons are produced by colliding electrons on tungsten; they are first injected in a damping ring to reduce their emittance (spread in position and momentum), then accelerated to 4 GeV with the Linac and injected in the Low-Energy Ring (LER). When sufficiently intense beams circulate in the LER and HER, they are brought to collision. The collision products fly from the interaction point (IP) trough the volume of the detector, where various final states (Table 2.1) can be detected.

To achieve high luminosities, a nano-beam, large crossing-angle collision scheme is implemented [13]. This is an innovative configuration based on keeping small horizontal and vertical emittance and large crossing angle, as shown in Figure 2.2. This is obtained with a final-focus superconducting-quadrupole-magnet system (QCS), made of magnets, corrector coils, and compensation solenoids; a QCS magnet is installed at each longitudinal end of the interaction region. Conceptually the nano-beam scheme mimics a collision with many short micro-bunches, allowing great advantages in luminosity with respect to previous standard schemes. The reduction of the luminous volume size to about 5% with respect to the predecessor KEKB, combined with doubling of beam currents, is expected to yield a factor 40 gain in intensity.

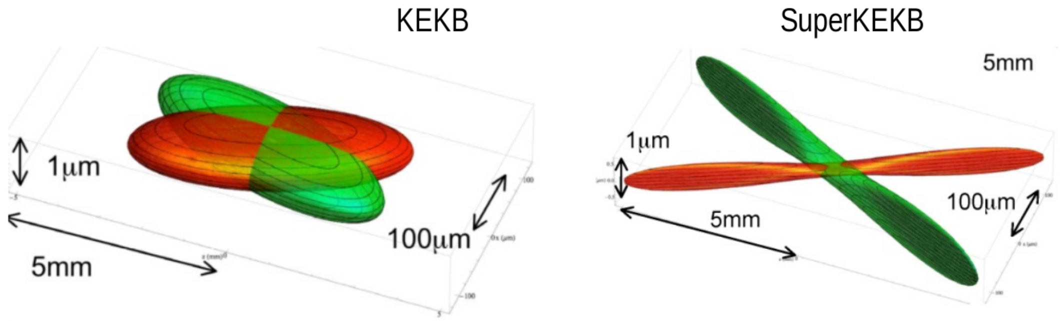

Figure 2.2: Three dimensional sketch of the bunch geometry at the interaction point for KEKB (left) and SuperKEKB (right).

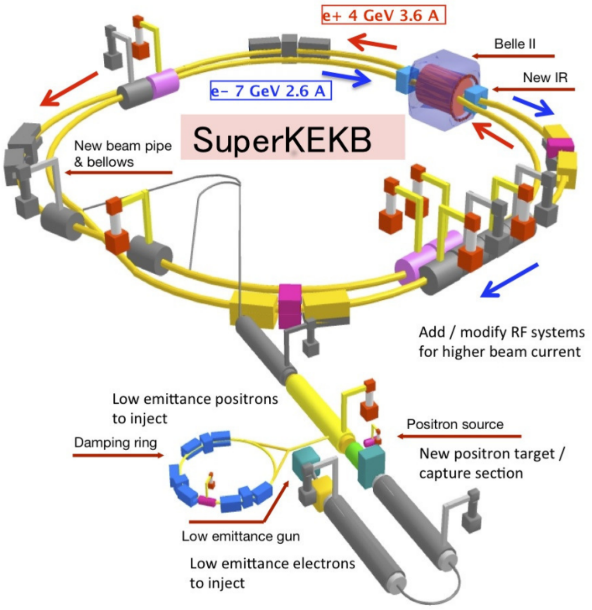

Figure 2.3: Scheme of the SuperKEKB collider.

2.2 Belle II detector overview

The Belle II detector main purpose is to maintain Belle performance in an environment with considerably higher background levels. Compared to Belle, the Belle II detector will be taking data at an accelerator with a 40 times higher luminosity, and thus has to be able to operate at 40 times higher event rates, as well as with background rates higher by a factor of 10 to 20. To maintain the excellent performance of the spectrometer, the critical issue is to mitigate the effects of higher background levels, which lead to an increase in occupancy

Final state	Cross section (nb)
$\Upsilon(4S)$	1.05
$c\bar{c}(\gamma)$	1.30
$s\bar{s}(\gamma)$	0.38
$\overline{dd(\gamma)}$	0.40
$u\bar{u}(\gamma)$	1.61
$e^{+}e^{-}(\gamma)$	300
$\mu^{+}\mu^{-}(\gamma)$	1.148
$\tau^{+}\tau^{-}(\gamma)$	0.919
$\nu\bar{\nu}(\gamma)$	0.25×10^{-3}
$\gamma\gamma(\gamma)$	4.99

Table 2.1: Cross sections of the main final states produced in e^{+} e^{-} collision at the $\Upsilon(4S)$ centre-of-mass energy [14].

and radiation damage, as well as to fake hits and pile-up noise in the electromagnetic calorimeter, and to neutron-induced hits in the muon detection system. Belle II provides an excellent vertex resolution and a very high reconstruction efficiency for charged particles, very good momentum resolution over the whole kinematic range of the experiment, precise measurements of photon energy and direction, highly efficient particle identification system to separate pions, kaons, protons, electrons, and muons over the full kinematic range of the experiment. In addition, a hermeticity at least as good as the original Belle detector is required. A fast and efficient trigger system, as well as a data acquisition system capable of storing large quantities of data, ensures Belle II to work with higher event rates. Belle II detector [15] has a cylindrical geometry with a central body, named barrel, and two endcap sections that close the two side of the interaction region. From the interaction point to the outer regions, as shown in Fig.2.4, the apparatus consists of various detector layers:

- The vertex detector (VXD) which main purpose is the reconstruction of charged particles two dimensional position, providing a better vertex resolution. It is comprised of two devices, the silicon pixel detector (PXD) and silicon vertex detector (SVD), with a total of six layers around the beam pipe.
- The central drift chamber (CDC) involved in tracking at large radii and particle identification. Information from the CDC are used for the trigger signal.
- The charge particle identification system, composed of a time of propagation (TOP) counter and an aerogel ring imaging Cherenkov (ARICH) counter, both designed to discriminate pions, muons and electrons using Cherenkov light.
- The electromagnetic calorimeter (ECL) to measure energy of photons and electrons and to separate electrons from hadrons.
- The $\mathrm{K}_{\mathrm{L}}^{0}$ and muon system that detect muons and $\mathrm{K}_{\mathrm{L}}^{0}$ escaping from the internal region.

A superconductive solenoid is located between the ECL and the KLM providing an axial magnetic field of 1.5 T. All the Belle II components and their specifications are summarised in Table 2.2.

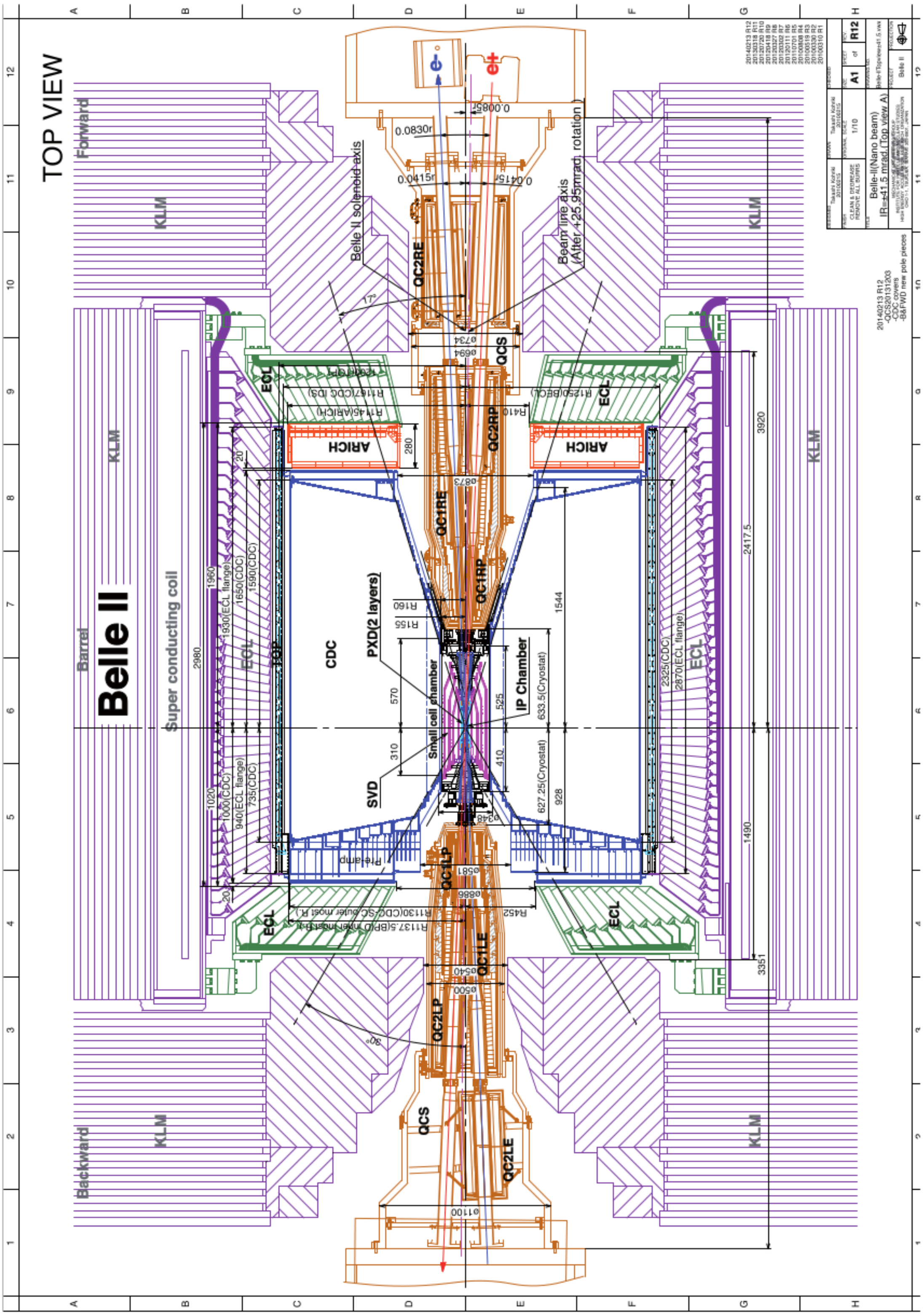

Figure 2.4: Belle II top view [15].

Purpose	Name Performance	Component	Configuration	Readout channels	θ coverage
Beam pipe	Beryllium		Cylindrical, inner radius 10 mm, 10 μm Au, 0.6 mm Be, 1 mm paraffin, 0.4 mm Be		
Tracking	PXD	Silicon pixel (DEPFET)	Sensor size: 15×(L1 136, L2 170) mm^2, Pixel size: 50×(L1a 50, L1b 60, L2a 75, L2b 85) μm^2; two layers at radii: 14, 22 mm	10M	[17°;150°]
	SVD	Silicon strip	Rectangular and trapezoidal, strip pitch: 50(p)/160(n) - 75(p)/240(n) μm, with one floating intermediate strip; four layers at radii: 38, 80, 115, 140 mm	245k	[17°;150°]
	CDC	Drift chamber with He-C_2H_6 gas	14336 wires in 56 layers, inner radius of 160mm outer radius of 1130 mm	14k	[17°;150°]
Particle ID	TOP	RICH with quartz radiator	16 segments in ϕ at $r \approx$ 120 cm, 275 cm long, 2cm thick quartz bars with 4×4 channel MCP PMTs	8k	[31°;128°]
	ARICH	RICH with aerogel radiator	2×2 cm thick focusing radiators with different n, HAPD photodetectors	78k	[14°;30°]
Calorimetry	ECL $\frac{\sigma E}{E} = \frac{0.2\%}{E} \oplus \frac{1.6\%}{\sqrt[4]{E}} \oplus 1.2\% \approx 1.7\%$	CsI(Tl)	Barrel: $r = 125 -$ 162cm, end-cap: $z =$ $-102 - +196$cm	6624 (Barrel), 1152 (FWD), 960 (BWD)	[12.4°;31.4°], [32.2°;128.7°], [130.7°;155.1°]
Muon ID	KLM	barrel:RPCs and scintillator strips	2 layers with scintillator strips and 12 layers with 2 RPCs	θ 16k, ϕ 16k	[40°;129°]
	KLM	end-cap: scintillator strips	12 layers of (7-10)×40 mm^2 strips	17k	[25°;40°], [129°;155°]

Table 2.2: Summary of the Belle II components and specifications.

2.3 Tracking system

The main purpose of the Belle II tracking system is to measure the two B decay vertices and to reconstruct charge particle trajectory, measuring particle positions inside the detector. The Belle II tracking system is composed of two detectors, a silicon vertex detector, close to the beam pipe, and a central drift chamber. Both the tracking detectors are immersed in a 1.5 T magnetic field parallel to the beam axis, which curves the charged-particle trajectories, allowing to infer the particle momentum from the reconstructed curvature of the trajectory. Magnetic field is provided by a cylindrical superconductive solenoid with a 3.4 m diameter and 4.4 m of length.

2.3.1 Vertex detector (VXD)

The vertex detector consists of two devices, the silicon pixel detector (PXD) and the silicon vertex detector (SVD), arranged altogether on six layers (Fig.2.5). It is designed to sample the trajectories of charged particles in the vicinity of the IP and therefore infer the decay position of long-lived particles. However, due to the small distance from the IP, the vertex detector has to withstand high backgrounds. A smaller distance from the interaction point helps vertex reconstruction, but it involves harsher operation conditions, of which an higher background and an increased occupancy, *i.e.* the fraction of channels hit in each triggered event.

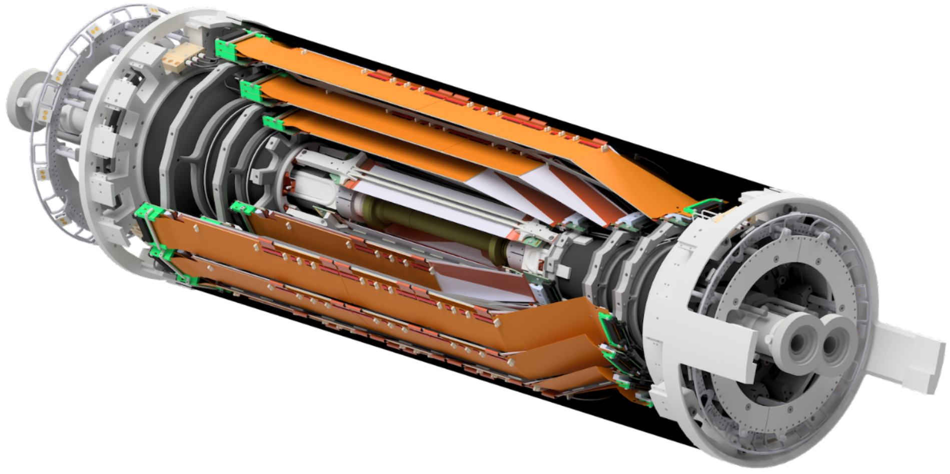

Figure 2.5: The Belle II vertex detector (VXD), composed of the pixel (PXD) and silicon strip (SVD) detectors. [16]

Pixel Detector

The PXD primary goal is to reconstruct charged particle trajectories while sustaining high hit rates. PXD is based on the DEPFET (Depleted Field Effect Transistor) technology [17]: a p-channel MOSFET is integrated onto a silicon substrate, which is fully depleted applying a suitable voltage. Incident particles generate electron-hole pairs within the fully depleted bulk. During readout the holes drift to the back contact, while electrons modulate the channel current through the MOSFET.

Belle II has adopted 75-μ thick pixel detector, with part of the electronic integrated with the sensor, allowing the amplification of the signal charge just above the position of its generation. The remaining readout electronics, which needs cooling, are located out-side the acceptance region and will not contribute to the multiple scattering material budget. This detector is a low power device, since the pixels are "on" only during the readout, and no active cooling is necessary for the pixel itself. Moreover, these sensors have a very small capacitance, resulting in a very low noise performance even at room temperature.

The PXD is composed of two coaxial layers of sensors with radii at 14mm and 22mm, as shown is Fig.2.6, for a total of around 8 million pixels.

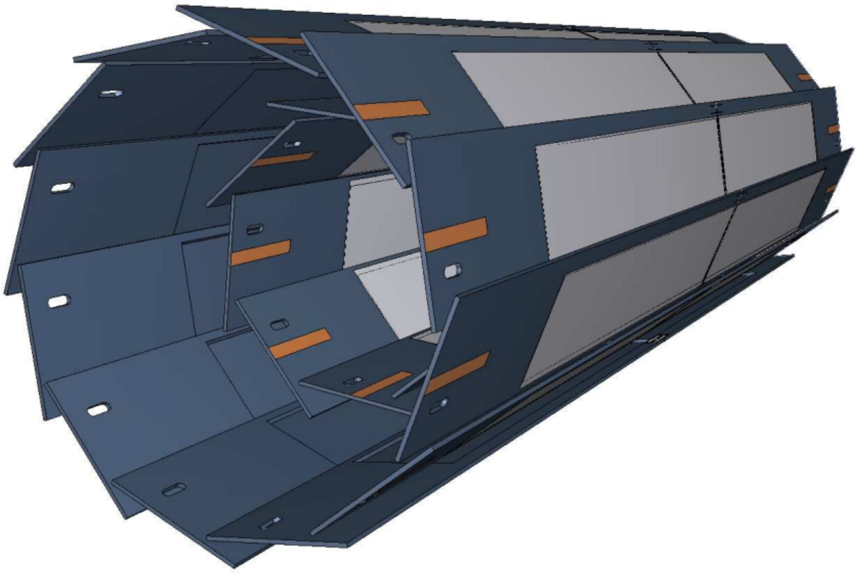

Figure 2.6: Schematic view of the geometrical arrangement of the sensors for PXD. The light grey surfaces are sensitive DEPFET pixels [15].

The inner radius leaves sufficient space for possible variation of the beampipe layout.

The pixel dimensions vary from $50\times(50-55)\mu\text{m}^2$ for the inner layer to $50\times(70-85)\mu\text{m}^2$ for the outer layer. The polar acceptance ranges from 17° to 150°.

The spatial resolution is 20 μm. To reach that, the position of the traversing charged particle is obtained by weighting the different amounts of charge measured in neighbouring pixels. The smaller separation between B vertices in an event due to the smaller Belle II boost with respect to Belle is compensated by a reduced radius of the first detector layer. Large backgrounds associate with high data rate, about 20 Gbit/s for 3% of occupancy. Data is reduced using information from other detectors, especially SVD. The distinction between physics and background hits relies on the extrapolation of tracks reconstructed in the SVD and propagated back to the PXD. Around each intersection point of a track with the PXD, a region of interest is defined. If a fired PXD pixel lies inside the region, it is kept; otherwise, it is discarded.

Silicon Vertex Detector

The SVD [16] primary goal is to reconstruct interaction vertices and low momentum charged particle tracks efficiently and with high resolution. SVD is based on double-sided silicon strip technology: each SVD sensor works as a reverse-biased p-n junction. The bulk of the silicon layer is n-doped and on one side of the silicon layer a highly doped p-implant is realized. By applying a bias voltage the depletion region is increased on the p-n junction.

Inside the depleted region, the intrinsic carriers are removed so the e-h pairs produced by charged particles are detected. They drift, following the electric field, to the edge of the depleted region where charge collection electrodes are located.

The Belle II SVD consists of four layers at 39 mm, 80 mm, 104 mm, and 135mm from the beam, with a mechanically stable structure. The four layer are made respectively of 7, 10, 12 and 16 modules (ladders), as shown in Fig.**??**. Each sensor is 300 μm thick and the strip pitch d_p, i.e. the space between consecutive strips, ranges across sensors and sides from 50 μm to 240 μm. The polar angular acceptance ranges from 17° to 150°. It is asymmetric to account for the forward boost of the centre-of-mass frame.

The SVD spatial resolution is a function of the polar angle, but is expected to range around 20 μm, typically. SVD is segmented and has a reduced readout latency to deal with the high hit rate. The material is kept as low as possible to interfere the least with low momentum particles, minimising the multiple scattering. The two-dimensional position reconstruction has resolution of $d_p/\sqrt{12}$. However usually the charge is not collected on a single strip but it is distributed over several strips allowing an improved position resolution by interpolation.

2.3.2 Radiation monitor system

The radiation monitor system is based on artificial single crystal diamond sensors. Its main goal is to protect the silicon vertex detector from high radiation doses that would deteriorate its performances. A critical feature of the radiation monitor system is the generation of beam abort requests to SuperKEKB if the radiation doses near the interaction region are higher than a certain threshold. The other main goal of the diamond system is to constantly measure the radiation level near the interaction point. These measurements are used to estimate the total dose absorbed by the silicon detector and to monitor the background evolution as the accelerator conditions change. The original plan for the monitor system consists of up to 20 sensors: eight located on the beam pipe, as close as possible to the interaction region and the PXD layers, the others on the support cones of the SVD. After

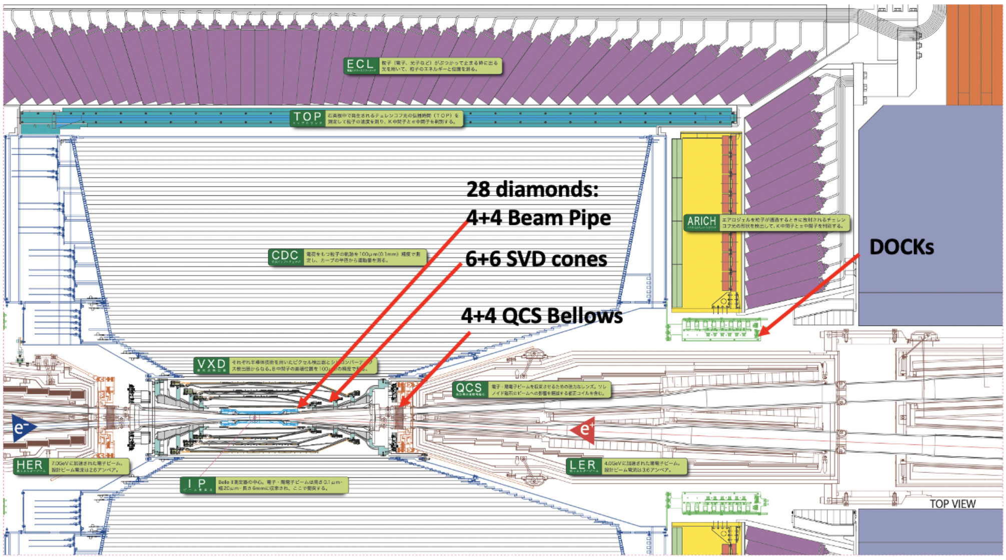

Figure 2.7: Part of the longitudinal section of the Belle II detector, with the positions of the 28 diamond detectors composing the Belle II radiation monitor system.

the accelerator pilot run in 2018, on request of SuperKEKB, eight more diamonds were installed on bellows, up- and down-stream of the interaction region, close to the final-focus QCS superconducting magnets. In these positions, they help protecting the QCS magnets from quenches in case of large beam losses, thus extending the original purpose of the system. The entire set-up is sketched in Figure 2.7.

2.3.3 Central drift chamber (CDC)

One of the core instruments of the Belle II spectrometer is the central tracking device, a large-volume drift chamber with small drift cells [18]. The central drift chamber (CDC) plays three important roles:

- it reconstructs charged particles by sampling their trajectories at large radii;
- it identifies them by using measurements of specific energy loss;
- it provides trigger signals for charged particles.

CDC is a gaseous detector: a charged particle, crossing the CDC volume, lose energy in the gaseous medium producing electrons and ions for ionization of the gas atoms. These charged carries, moved by an external electric field, drift to the cathodes, multiplying when the electric field is sufficiently high. The time between the collision and the CDC signal allow to infer the particle position. The CDC radius ranges from 160 mm to 1130 mm, extending to a larger radius compared to Belle (1130mm instead of 880 mm), due to a much thinner particle identification (PID) device in the barrel region. The azimuthal acceptance rangesfrom 17° to 180°.

To be able to operate at high event rates with increased background levels, the chamber increases the occupancy using smaller drift cells than the one used in Belle. In total, the CDC contains 14 336 sense wires arranged in 56 layers, either in "axial" orientation (aligned with the solenoidal magnetic field) or "stereo" (skewed with respect to the axial wires). By combining information from the axial and stereo layers it is possible to reconstruct a full three-dimensional (3D) helix track. The chamber gas is comprised of a He–C_2H_6 50:50 mixture with an average drift velocity of 3.3 cmμs^{-1} and a maximum drift time of about 350 ns for a 17 mm cell size. Ethane has low radiation length, good position resolution, good energy loss resolution, low cross section for synchrotron radiation X-rays, and suffers little radiation damage.

The spatial resolution is about 100 μm and the specific ionisation, dE/dx, resolution for an incident angle of 90° is 11.9%.

Figure 2.8 shows a reconstructed cosmic ray track in the CDC.

2.4 Particle Identification

Identification of charged particles over the full kinematic range is one of the basic requirements for Belle II. The Belle II particle identification (PID) system consists of two main detectors: the time of propagation (TOP) counter in the barrel region and the Aerogel ring imaging Cherenkov (ARICH) counter in the forward endcaps. These two detectors have been designed to separate kaons from pions and to provide discrimination between pions, muons and electrons, both using Cherenkov light. In Figure 2.9 is outlined the different angle of reflection of Cherenkov photons produced by two different particles, which forms the basis of the particle identification procedure.

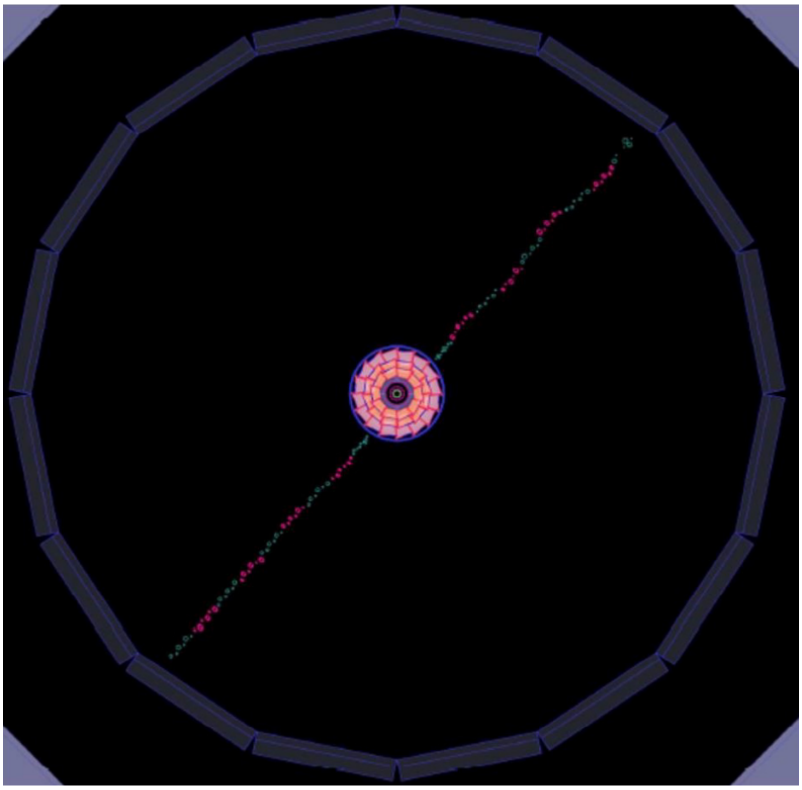

Figure 2.8: A cosmic ray muon recorded by the Belle II Central Drift Chamber(CDC) [15].

An upgrade of the system has been compulsory both to operate in higher background environment and to improve the calorimeter response to electromagnetic particles, reducing the amount of PID material.

2.4.1 Time Of Propagation counter

The TOP [19] measures the time of propagation of the Cherenkov photons produced by charged particles and internally reflected inside a quartz radiator. A three-dimensional image is reconstructed from the x and y coordinates of the photon hits and from the propagation time. A photon originated from a heavy charged particle would, on average, arrive at a later time than one that originated from a light one. This is due to the mass difference and the inverse proportionality between the cosine of the Cherenkov angle and the particle velocity.

The TOP is made of 16 quartz bars mounted on the barrel at 1.2 m from the interaction point. Each bar is a photon radiator and has three main components. A long bar for radiating Cherenkov light and propagating it to the bar end; a spherical mirror mounted on the forward end of the bar for focusing the light; a prism attached to the backward end of the bar that drives the light to micro-channel plate photomultipliers. The polar angular acceptance ranges from 31° to 128°. Figure 2.10 shows a scheme of a quartz bar. The time resolution is about 100 ps. TOP is expected to achieve a good separation of pions and kaons from 0.4 GeV/c up to 4 GeV/c.

For the precision timing required in this type of counter, custom-made waveform sampling readout electronics are used. Note that for this identification method the starting (particle production) time has to be known with a precision of about 50 ps; this is indeed

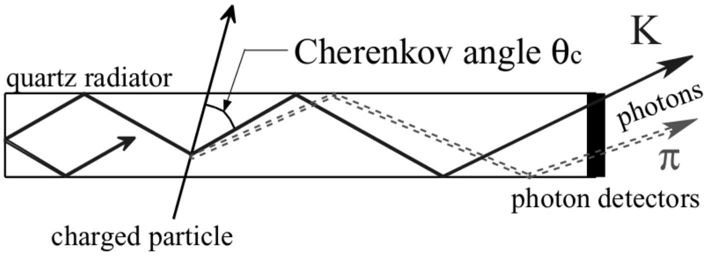

Figure 2.9: Schematic side-view of a quartz radiator and internal reflecting Cherenkov photons.

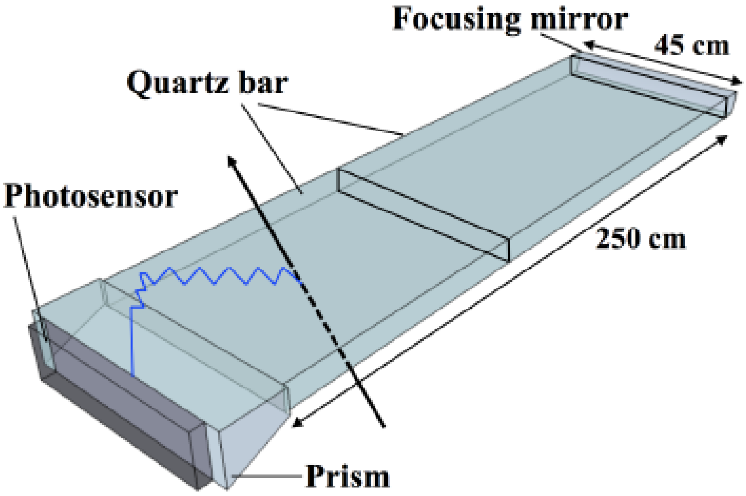

Figure 2.10: Representation of a TOP counter. The figure shows a charged particle that crosses the radiator and emits Cherenkov light. Light is absorbed by a photomultiplier and converted into an electric signal.

challenging, but was already achieved for the time-of-flight (TOF) counter of Belle.

2.4.2 Aerogel Ring-Imaging Cherenkov counter

The primary goal of the aerogel ring-imaging Cherenkov counter (ARICH) [20] is to separate kaons from pions over most of their momentum spectrum. It is used also to provide discrimination between pions, muons and electrons below 1 GeV/c. An aerogel radiator produces Cherenkov photons as a charged particle crosses it. In front of the radiator, an expansion volume allows Cherenkov photons to form rings on the photon detector surface. These photons are then collected by an array of position-sensitive photo-diodes. A photocathode is used to generate photoelectrons that are accelerated using an electric field and multiplied in an avalanche. A readout system provide the photon hit positions.

Figure 2.11 shows the main parts of the ARICH detector. Two consecutive aerogel radiator layers with different refraction indices are used to generate enough photons to maintain sufficient resolution.

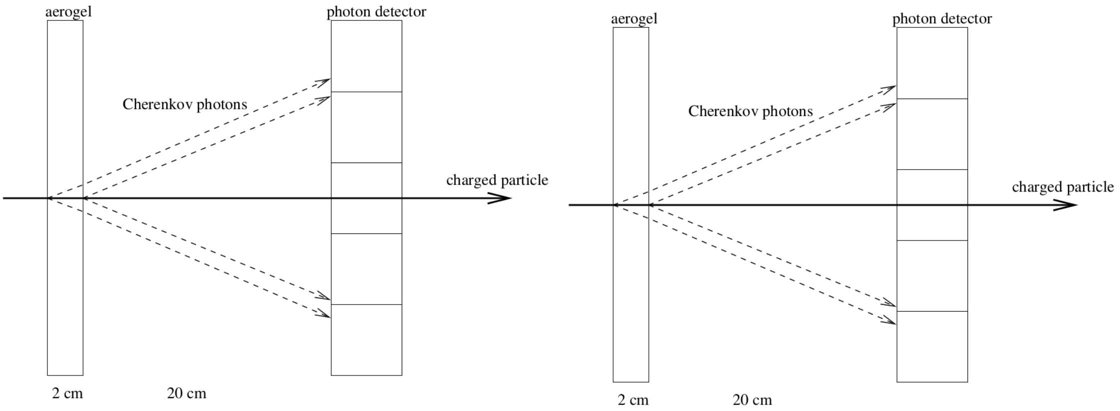

Figure 2.11: Scheme of ARICH detector showing the proximity focusing principle (left) and of the inhomogeneous configuration of the aerogel radiatior (right).

The ARICH container consists of two cylinders with inner and outer radii of 410 mm and 1140 mm, respectively. The polar angular acceptance ranges from 14° to 30°. The expected ARICH performances would enable better than $5\,\sigma$ pion-kaon separation at the kinematic limit of GeV/c. Pions would be separated by $4\,\sigma$ from electrons up to about 1 GeV/c.

2.5 Electromagnetic calorimeter

The electromagnetic calorimeter (ECL) [21] is used to detect gamma rays as well as to identify electrons, i.e. separate electrons from hadrons, in particular pions. It is a highly segmented array of thallium doped caesium iodide CsI(Tl) crystals assembled in a projective geometry (Fig.2.4). The ECL working principle is based on scintillation: the energy released in particular scintillating materials by an impinging particle is partially converted into light that is collected by photodiodes. The ECL consists of a 3 m long barrel section with an inner radius of 1.25 m, annular endcaps are at $z = 1.96$ m (forward) and $z = -1.02$ m (backward) from the interaction point. All three detector regions, the barrel as well as the forward and backward endcaps, are instrumented with a total of 8736 crystals, covering about 90% of the solid angle in the centre-of-mass system. The CsI(Tl) crystals, preamplifiers, and support structures have been reused from Belle, whereas the readout electronics and reconstruction software have been upgraded. In the Belle experiment, the energy resolution observed with the same calorimeter was $\sigma_E/E = 4\%$ at 100MeV, 1.6% at 8 GeV, and the angular resolution was 13 mrad (3 mrad) at low (high) energies; π_0 mass resolution was 4.5 MeV/c^2 [21]; in the absence of background a very similar performance would also be expected for Belle II. In the presence of considerably elevated background levels as compared to the operation in Belle, the relatively long decay time of scintillations in CsI(Tl) crystals will considerably increase the overlapping of pulses from neighboring (background) events. To mitigate the resulting large pile-up noise, scintillator photo-sensors were equipped with wave-form-sampling readout electronics. In the forward region of the detector, close to the beam pipe, much higher background rates are expected, such that even with the new wave-form-sampling electronics the pile-up noise will degrade the performance. Some further degradation could come from a reduction of the light yield due to radiation damage, although this effect seems to be less significant than originally anticipated. In this region CsI(Tl) crystals are replaced with considerably faster and radiation tolerant pure CsI crystals, which have a lower scintillation decay time allowing the reduction of background photons due to the high luminosity..

2.6 K_L^0 and muon detector

The K_L^0 and muon detector (KLM) [22] contributes to the identification of muons and detects neutral particles that do not interact with the inner detectors, such as K_L^0.

The working principle is based on scintillators in the inner layers and glass-electrode resistive-plate chambers in the outer layers. A gas mixture fills the space between the chambers electrodes. After applying an appropriate voltage, the charge produced by a traversing charged particle is collected. Charged particles can be produced by K_L^0 mesons through hadronic showers interacting with the iron plates. The KLM is made of alternating pattern of 4.7-cm thick iron plates and active detector elements. The iron plates serve as the magnetic flux return for the solenoid and they also provide 3.9 interaction lengths in which K_L^0 mesons can shower hadronically. The barrel section of the detector covers 45° to 125° in polar angle. The endcaps cover 20° to 45° and 125° to 155°. The muon and K_L^0 reconstruction efficiencies are higher than 80% if the momentum is larger than 1 GeV/c and 3 GeV/c respectively. Muons are identified by extrapolating outwards the particle track and calculating a predicted range. If the predicted and actual ranges agree the particle is identified as a muon.

2.7 Online event selection

Various processes may occur in 10 GeV e^+e^- collisions (Tab. 2.1). Since the events of physical interest are a fraction of the total cross section, the goal of the online event selection (trigger) is to identify them in real time while rejecting background events, to reduce the data-writing rate. The trigger must be efficient for recording hadronic event from $\Upsilon(4S) \to B\overline{B}$ and for the continuum to a manageable level, up to a maximum accept rate of about 30 kHz, due to data acquisition restrictions. $B\overline{B}$ events have distinctive high-track multiplicity, and therefore are relatively straightforward to select; events containing τ decays are harder, since they have fewer tracks in the final state and can therefore be misclassified as backgrounds. The trigger must also reject processes that are not interesting for Belle II physics, like $e^+e^- \to e^+e^-$ or $e^+e^- \to \mu^+\mu^-$.

The trigger is composed by a hardware trigger called Level1 (L1) [15] followed by a software high level trigger (HLT) [15]. The L1 decision is mainly based on informations from CDC and ECL, but also TOP and KLM informations can be used. The L1 decision feeds the global decision logic [15], that sends out the final trigger based on the informations it receives from the detector. HLT is based on a more complete software reconstruction of the event similar to the offline reconstruction, using charged particles from the CDC and energy deposits in the ECL. It selects events on the base of tracking multiplicity, vertex position and total energy deposition. HLT is expected to achieve a 30% event rate reduction without efficiency loss for signal processes.

Chapter 3

Beam background and monitoring systems

In this chapter the main sources of accelerator beam losses and backgrounds are discussed, highlighting their dependencies on the accelerator conditions. Possible damage to the silicon vertex detector associated with such backgrounds is also described. Finally this chapter presents the main features and capabilities of diamond sensors used as radiation monitors, and that I characterised.

3.1 Accelerator backgrounds

While beams are circulating, various processes may perturb the motion of the beam particles. These processes often generate backgrounds that need to be understood and controlled in order to safely operate the machine and the detector [23].

Touschek scattering is a single electromagnetic scattering between two particles of the same bunch. The momentum transferred in the collision may deviate one or both particles outside the momentum acceptance [24], resulting in their loss. Touschek collisions are possible because, due to the momentum and energy spread of particles within the same bunch, particles undergo betatron and synchrotron oscillations during their motion. Given the Touschek scattering probability [25], the total scattering rate (r_T) is proportional to the number of filled bunches (n_b), the square of the bunch current (I_b), the inverse of the horizontal and vertical bunch sizes (σ_x and σ_y), the inverse of the bunch length (σ_z), and the inverse third power of accelerated-particle energy (E),

$$r_T \propto \frac{n_b I_b^2}{\sigma_x \sigma_y \sigma_z E^3} \,. \tag{3.1}$$

Higher beam currents along with a smaller beam size imply a large increase of Touschek scattering in SuperKEKB with respect to its predecessor KEKB. Particles lost due to Touschek scattering hit the beam-pipe inner wall, producing electromagnetic showers. If this occurs near the interaction point, the shower products can reach the detector, generating signals not related to collisions. Movable metallic blocks mounted inside the beam pipe (collimators) are used to mitigate the effects of Touschek scattering. These devices stop off-trajectory particles, not allowing them to reach the interaction region. During the accelerator design it has been decided to increase the LER energy to 4 GeV: this choice reduces the Touschek LER background.

Beam-gas scattering is a scattering of beam particles with residual gas molecules in the beam pipe. The particle-molecule interaction may occur through two different processes: Coulomb scattering, which changes the direction of the beam particle; and bremsstrahlung scattering, which also reduces the energy of the beam particle, through photon emission. Beam-gas scattered particles are lost by hitting the beam pipe inner wall while they propagate around the ring. The beam-gas scattering rate (r_{BG}) is proportional to the beam current (I) and to the pressure (P) inside the beam pipe.

$$r_{BG} \propto IP = p_0 I + p_1 I^2 \tag{3.2}$$

Two components contribute to the pressure, a pressure without beams (p_0), and a dynamical component that depends on the total beam current (p_1). This second term is related to desorption effects: previously absorbed gas molecules can be re-emitted by the beam pipe walls. An improvement of the vacuum quality is usually achieved by *baking* and *vacuum-scrubbing.* During *baking*, sections of the beam pipe are heated up and the released gas molecules are extracted using vacuum pumps. *Vacuum-scrubbing* consists in letting the beams circulate without collisions to stimulate the re-emission of molecules absorbed by the beam-pipe walls and their extraction by vacuum pumps. The beam-gas background is reduced by tuning the collimator positions.

Synchrotron radiation is the emission of photons by accelerated charged particles. The power emitted (W_S) is proportional to the beam energy (E) squared, the magnetic field strength (B) squared, the inverse fourth power of the mass (m), and the inverse square of the curvature radius (ρ).

$$W_S \propto \frac{E^2 B^2}{m^4 \rho^2} \tag{3.3}$$

Given the proportionality to the beam energy squared, the HER beam is the main source of this background. Since the sources of SR background are the accelerated particles, the photon emission rate is proportional to the beam current. The energy spectrum of SR photons ranges from a few keV to tens of keV. In order to protect the vertex detector from SR-induced damage, the shape of the beam pipe in the interaction region is designed to avoid direct SR hits at the detector and its inner surface is coated with a gold layer to absorb SR photons. However, during the accelerator commissioning we observed a SR-component in the particle energy spectrum detected by dedicated sensors placed around the IP. Beam-pipe materials irradiated by SR were found to emit fluorescence photons that interact with surrounding detectors.

Radiative Bhabha process is an electron-positron scattering process where a photon is present in the final state, in addition to the initial particles, $e^+e^- \to e^+e^-\gamma$ (Fig.3.1). Radiative Bhabha photons can interact with the iron of the accelerator magnets, producing low-energy gamma rays and neutrons. Low-energy gamma rays contribute to the background for the CDC and for the barrel particle identification systems. Neutrons are the main background source for the outermost detectors like KLM. Neutron shielding is used in the accelerator tunnel to reduce their flux. By emitting a photon, electrons and positrons lose energy and may then hit the beam pipe walls, producing electromagnetic showers in turn. Bhabha scattering is also important for luminosity measurements. The Bhabha cross section is large and dominated by electromagnetic interactions. Therefore it is possible to use perturbative QED and predict the cross section with high accuracy. Luminosity is calculated starting

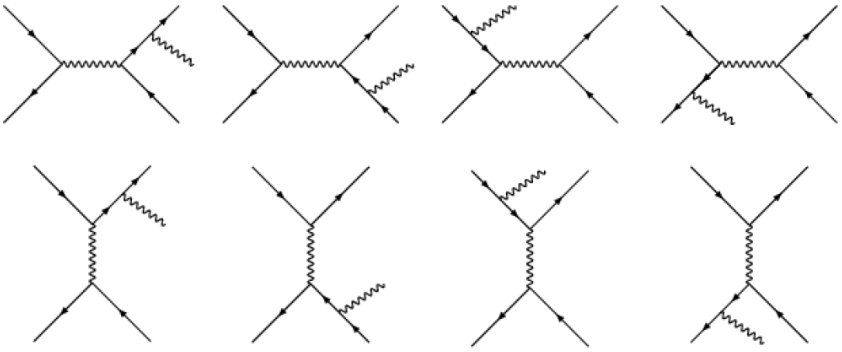

Figure 3.1: Leading-order Feynman diagrams that contribute to the radiative Bhabha process.

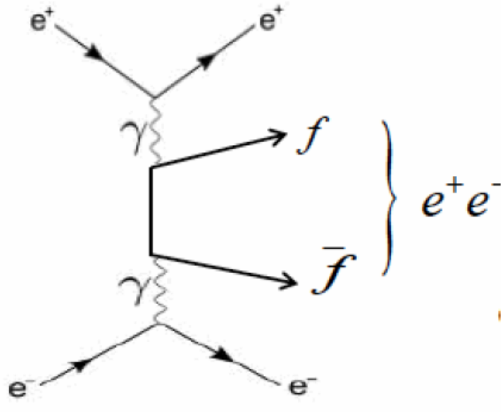

Figure 3.2: Leading-order Feynman diagram for the two-photon process.

from the known cross section by determining the Bhabha rate in a region of known acceptance.

Two photon process is the QED process $e^+e^- \to e^+e^-e^+e^-$. Low momentum electron-positron pairs can spiral around the magnetic field lines of the Belle II solenoid leaving multiple hits in the inner Belle II detectors. The primary particles that lose a large amount of energy or scatter at large angles can be lost inside the detector, as with radiative Bhabha. As the background particles interact with the inner detector, they increase the hit multiplicity, making tracking more difficult.

Injection background is caused by charge injection in a circulating beam bunch. The main difference between the stored particles and injected particles is the oscillation amplitude around the bunch center. Injected particles oscillate with larger amplitudes and they can be lost in Belle II detector. After each injection the bunch is perturbed and a higher background rate is observed in the detector for few milliseconds after the injection. A veto signal is applied to PXD detector to prevent the detector readout during each injection.

All these backgrounds strongly depend on the beam optics. According to preliminary estimates, the PXD total integrated dose may range from about 150 to about 180 kGy (15 to 18 Mrad) during the projected lifetime of Belle II at the design integrated luminosity

(50 ab^{-1}). For the inner and less exposed layers of the SVD approximately 4.5 Mrad are expected to be integrated during the same Belle II activity period [26]. We used these estimates to approximately determine the radiation dose-rate thresholds for beam abort requests, needed to prevent the vertex detector from integrating radiation doses significantly higher than the design values.

3.2 Radiation damage to silicon detectors

All background sources described in Section 3.1 can damage the VXD sensors, deteriorating its tracking performances as the absorbed dose increases. For proper charged particle pattern recognition the signal-to-noise ratio of the silicon vertex detector has to remain in excess of 10 during the whole duration of Belle II data taking. In order to protect the inner detectors, whose tracking capabilities are essential for the Belle II physics program, a radiation monitoring and interlock system has to be mounted near the IR. In this section the main sources of damage related to radiation in semiconductor devices are presented. Changes in the macroscopic behavior are traced back to microscopical lattice structure changes [27].

3.2.1 Radiation-induced defects

Depending on radiation type and energy, the interaction may involve the electrons of the silicon crystal or the Si nuclei in the lattice. Typically, the interaction with the electrons is a transient effect and it is used for detecting particles. On the other hand, the interaction with the nuclei may lead to permanent damage. Lattice atom displacement generates interstitials (atoms between regular lattice sites) and vacancies (empty lattice sites). These defects are unstable, they can mitigate, partially anneal or combine with other defects to form more stable defects, which may change the electrical properties of the semiconductor. Displaced lattice atoms with enough energy can cause secondary cascade processes. An impinging particle has to transfer at least 15 eV to a silicon atom to displace it from its lattice site. For recoil energies below 2 keV, isolated defects are created. At higher energies defect clusters can also be generated, where a cluster is a dense agglomeration of point defects that appear at the end of a recoil silicon-atom track. The type and energy of the impinging radiation determine the probability of forming a primary knock-on atom, which is a silicon atom displaced from its original lattice position. The so-called "non-ionizing energy-loss" is used to measure and compare radiation damage from different sources [28] since ionizing energy-loss does not produce crystal defects. On a microscopic scale, defects have several consequences. They act as recombination-generation centers as they can capture and emit electrons and holes; they are also trapping centers, where electrons and holes are captured and re-emitted with some time delay; they can also be charged, affecting the space charged density in the depletion region. Beside displaced silicon atoms, radiation can also affect the dielectric layers present in silicon devices and the interfaces between them and the silicon. The main effects are a charge build up in the oxide and an increase in the interface trap density.

3.2.2 Effects on detector properties

The microscopic lattice defects induce several changes in the properties and operating parameters of a detector.

Operating voltage: radiation damage may change the space charge density in the silicon depletion region. As a consequence, the bias voltage necessary to deplete the bulk changes. Radiation-originated defects can interact with dopants such as phosphorus present in n-type substrates used for the SVD sensors, changing their charge state and preventing them from fulfilling their role as donors (donor removal). In addition they act as effective acceptors. The effective doping decreases as the impinging particle fluence (number of particles that intersect a unit area of the detector) increases until an intrinsic-like condition is achieved. Increasing furthermore the fluence brings to a type inversion of the n-type silicon substrate. During Belle II data taking, the SVD sensors are expected to suffer from donor removal, as the absorbed dose increases. Hence the applied voltage will be changed to obtain the best detector performances.

Reverse-bias current: defects can emit electrons and holes, causing the generation of a reverse-bias current in the depleted volume. The major contributions to this current come from defects whose energy levels are near the band-gap center. Since the defect generation is proportional to the impinging-particle fluence, a linear relation between the leakage current increase and the fluence exists. Bulk defects and interface traps increase the reverse-bias current in depleted volume and surface respectively. The reverse-bias current increases the detector noise level, deteriorating the tracking performances.

Trapping of signal charge: the trapping probability for charge carriers per unit time is approximately proportional to the trap concentration, which is increased by radiation-induced damage. Unlike reverse-bias current, where only energy levels close to midgap contribute significantly, all the defects are able to trap charge carriers. Trapped charge carriers are released after some time and only if they are released early enough they can fall in the time window needed for charge collection. Otherwise, trapping decreases the charge collection efficiency (CCE) of the detector, defined as the ratio between the collected and the created charge due to an impinging particle. Like reverse-bias current, charge trapping also lowers the detector SNR, this time by reducing the signal.

The damage sources described so far depend on the particle fluence accumulated over time on the detector. However spike-like intense and rapid energy releases may also produce additional damage. During short, intense irradiation, a very high density of carriers can be created. The silicon then behaves more like an electrical conductor, causing the applied voltage to drop across the dielectric layer of the AC coupling capacitors integrated in the SVD sensors. High voltage difference across the oxide can lead to dielectric breakdown, thus shorting the AC capacitors. Radiation damage not only affects sensors, but also their readout electronics which is located in the same volume. However, the use of thin high-quality gate oxides in CMOS technology has reduced the effects of radiation damage [29] on readout circuits, which makes these effects less relevant for sensors.

3.3 Diamond sensors for radiation monitoring

An efficient vertex detector tracking is fundamental to achieve the Belle II flavor physics goals and the construction of a new vertex detector takes up to three or four years, with significant effort and cost. An efficient and reliable protection system is therefore needed to keep the vertex detector safe from high radiation doses and to extend its operating life as much as possible with limited effects on its performance. As the protection system measures radiation levels, the same system is also essential for monitoring beam losses, correlating them with SuperKEKB parameters. The radiation system has to operate smoothly and without severe performance degradation for the entire Belle II operation: as the SuperKEKB parameters will be optimized to achieve high luminosities, the radiation system measurements will continue to be fundamental. Several options have been developed for radiation monitoring and beam loss detection at accelerator facilities over the years. Gas ionization chambers are the most widely used instrument whenever enough space is available without interference with the experimental apparatus, for example along the accelerator ring. Closer to the interaction region, where limited space is available, and the amount of material should be minimized, silicon PiN diodes have been frequently used [30–32]. These sensors have however some serious drawbacks: their reverse-bias current, that measures the instantaneous radiation dose rate, strongly depends on temperature. The dark leakage current, with no radiation present, strongly increases as the radiation damage accumulates with the integrated dose. As a result, they require frequent re-calibrations and the subtraction of a dominant dark leakage current term, that introduce large systematic errors. Belle II chose diamond sensors as radiation monitors due to their superior performances over concurrent technologies, such as silicon PiN diodes mentioned above. Table 3.1 shows a comparison between diamond and silicon main characteristics: high-purity diamond crystals can be considered as a "wide-gap intrinsic semiconductor" with interesting properties as compared to silicon.

Property	Diamond	Silicon
Number of atoms density N [10^{22} cm^{-3}]	17.7	5.0
Mass density ρ [g cm^{-3}]	3.53	2.33
Band gap E_g [eV]	5.47	1.12
Resistivity ρ_c [Ω cm]	$> 10^{12}$	2.3×10^5
Electron mobility μ_e [cm^2 V^{-1} s^{-1}]	1800	1350
Hole mobility μ_h [cm^2 V^{-1} s^{-1}]	1200	480
Electron saturation velocity v_e^s [10^6 cm s^{-1}]	26	10
Hole saturation velocity v_h^s [10^6 cm s^{-1}	16	7
Thermal conductivity k [W cm^{-1} K $^{-1}$]	21.9	1.5
Energy to create e-h pair $\epsilon_{e/h}$ [eV]	13	3.6
Displacement energy E_d [eV/atom]	42	15

Table 3.1: Comparison between diamond and silicon main properties at T=300K.

The high displacement energy and extreme thermal conductivity guarantee radiation resistance and a negligible temperature dependence of diamond sensors [33]. These properties are particularly suited for operations in high radiation environments. The wide band gap allows to operate with low leakage current. The high thermal conductivity makes the diamond an interesting material for applications where active detector cooling is impractical such as in the restricted volumes around collider experiment interaction-regions. The high charge carrier mobility enables fast signal collection. Despite these very interesting properties, a wide use of diamond for large-area applications in tracking devices has been limited by the difficulty of producing high-quality crystals and by the availability of a mature detector technology based on silicon wafers with microstrip or pixel electrodes [34,35]. The ratio between cost and sensor area is much higher in diamond detectors than in silicon.

Also the diamond wafer size is limited to few cm^2 , restricting the range of applications. One of the most effective techniques developed to grow detector-quality diamond crystals is the chemical vapor deposition (CVD) that is also used to grow diamonds used for Belle II [36].

An interesting and rather complex feature of the diamond sensors, common to all photoconductors, is the *photoconductive gain* $\mathcal{G}$ [37,38]. This is defined as the ratio between the charge collected at the electrodes and the charge generated by radiation inside the active volume of the detector. Commonly, in a semiconductor with photoconduction effects, $\mathcal{G}$ is greater than 1 and can reach very high values (up to 10^6) [38]. Instead, for the p-n junction photodiodes this values is $\mathcal{G} = 1$ or lower, as a function of the recombination of charge carriers while moving to the electrodes. Empirical studies show that the photoconductive gain differs for each diamond sensor and it increases monotonically as a function of the polarization bias. The simplest approach is to study $\mathcal{G}$ for each diamond sensor separately and at a given polarization bias $V_{\mathrm{bias}} = \pm 100\,\mathrm{V}$. This value is motivated by two considerations. Above $\approx 50\dot{\mathrm{V}}$, a full efficient charge collection is already expected for single crystal diamond. Too high voltages can induce instabilities or discharges. The calibration measurements performed with a β radiation source on the 28 diamond sensors of the radiation monitor system showed values of gain ranging from 1 to 5 for $V_{\mathrm{bias}} = \pm 100\,\mathrm{V}$ [39].

3.3.1 Chemical vapor deposition

Diamond crystals are formed by heating carbon under extreme pressure. This process forms the basis of the traditionally used high-pressure high-temperature growth technique that emulates the growing process of natural diamonds. More recently the possibility to grow diamond crystals at much lower pressures was developed and represented a fundamental technological breaktrough. The chemical vapor deposition (CVD) technique consists in adding carbon atoms one-at-a-time to an initial lattice template. The thermal decomposition of carbon-containing gases (precursor gases) under reduced pressure is used to grow diamond on pre-heated substrates. At room temperature and pressure, graphite is the thermodynamically stable allotrope of carbon. The growth of diamond (rather than graphite) requires that the precursor gas (usually CH_4) is diluted in excess of hydrogen, in a typical mixing ratio of 1% vol. The temperature of the substrate is usually greater than 700 °C to ensure the formation of diamond rather than amorphous carbon. The process gases diffuse toward the substrate surface, passing through an activation region (*e.g.*, a hot filament or electric discharge), which provides energy to the gaseous species. This activation is used to create reactive radicals and atoms that interact with the substrate surface to form diamond crystals. Atomic hydrogen is the most critical component in the gas phase mixture. It etches graphite-like sp^2 carbon bonds many times faster than diamond-like sp^3 carbon bonds. The growth rate depends on the crystal area and on the used technique but its typical value is around 10 to 100 μm/h. For more details see Ref. [40].

3.3.2 Detection of charged particles

The mechanism of charged-particle detection by diamond sensors is outlined in Fig. 3.3. The energy released in the diamond bulk by an impinging charged particle produces pairs of charge carriers, electrons (e) and holes (h), through ionization. The same mechanism is present in semiconductor materials, where an electron is promoted from the valence band to the conduction band after absorbing enough energy. This transition generates two oppositely charge carriers, an electron in the conduction band and a hole in the valence band [41]. The energy needed for the promotion from a lower to a higher band depends on

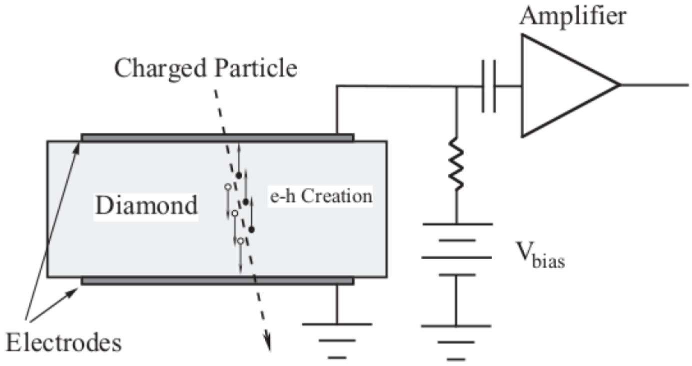

Figure 3.3: Schematic layout of a diamond sensor. The charge carriers produced by an impinging particle are collected by applying an external electric field via a bias voltage V_{bias}. The AC component of the signal is then amplified and read by an external readout system.

the forbidden energy gap that separates the two bands and on the fraction of transferred energy that excites other degrees of freedom. Electrons and holes are collected by applying an external electric field in which the charge carriers drift in opposite directions. The electric field in the diamond bulk is generated by applying to the metallic contacts a bias voltage V bias of a few hundred volts. The time-dependent component of the collected signal is decoupled from the constant bias voltage with a decoupling circuit with careful impedance matching and is then amplified and recorded by an external readout system. The measured time-dependent current is determined by several factors: the initial space distribution of charge carriers, the electric field and the resulting drift velocities.

3.3.3 Response to neutral particles

The capability of diamond sensors to measure backgrounds depends on the efficiency in detecting the different types of particles that constitute these backgrounds.

Photons Photon backgrounds are associated with several sources (Section 3.1). They produce primary and secondary particles that may reach the vertex detector. The physical process subtending photon detection in diamond sensors depends on the photon energy. Photons with energies $E_\gamma < 1$ MeV can be absorbed by shell electrons via photoelectric effect. Intermediate-energy photons ($0.1 < E_\gamma < 10$ MeV) can be indirectly detected by Compton scattering, that transfers part of their energy to an electron; the charged electron is in turn detected via the usual ionization and generation of electron-hole pairs. High energy γ rays can interact with carbon nuclei producing e^+e^- pairs [42]. The probability of this process is small, due to the small amount of material in the diamond sensor. These photons are detected with higher probability if they initiate an electromagnetic shower, with charged electrons and positrons, in the material surrounding the diamond sensor.

Neutrons Among the most harmful sources of damage for the vertex detector are neutrons. Neutrons can be produced by high-energy beam particles hitting the surrounding material and exciting nuclei. Even if diamond has the highest atomic density of any material, contributing to the detection efficiency per unit volume [43], the inter-

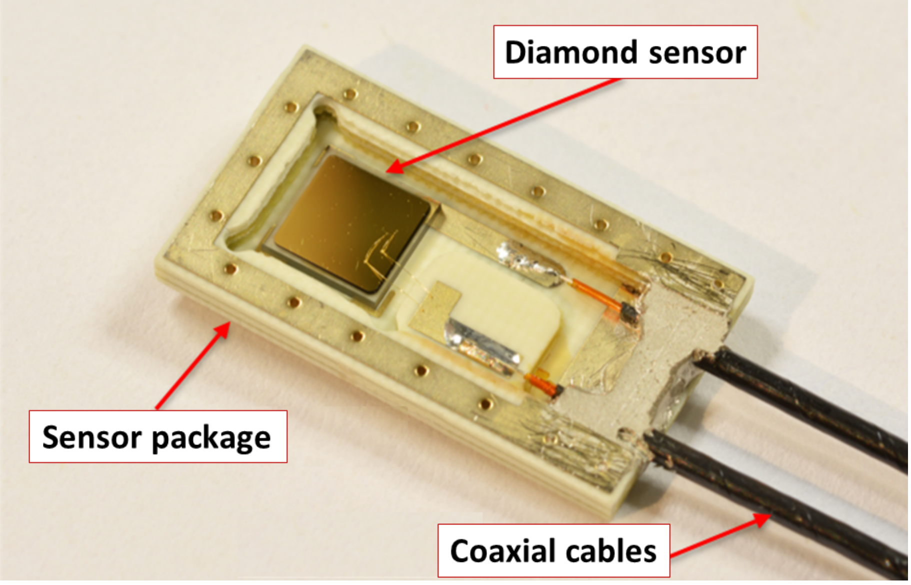

Figure 3.4: Picture of the diamond sensor, hosted on its ceramic package, and the coaxial cables connected to the diamond electrodes.

action probability with the tiny diamond volume is very small. Furthermore Belle II diamond detectors cannot distinguish between neutron and charged-particle interactions in an effective way.

3.4 Description of the sensors under study

In this work, I characterised four diamond sensors similar to those employed in the radiation monitor system. They are named with the acronyms DC00, DC01, DC15 and DC25. These sensors are $(4.5 \times 4.5 \times 0.5)$-mm^3 single crystals obtained by CVD. The full volume can be considered as active in term of energy deposition in the study presented in this work. Metallic electrodes are deposited on the top and bottom sides. These two electrodes, when polarised by a high-voltage bias, generate a uniform electric field in the diamond bulk that collect the charge carriers as described in Ref. [36]. The electrodes are (4.0×4.0)-mm^2-wide layers of titanium, platinum, and gold with thicknesses of 100, 120, and 250 nm, respectively. The electrodes are radiation-resistant, and temperature-resistant up to 400 ° C. The external gold layer on the electrodes ease wire-bonded connections to the electronics. The sensors are hosted on a compact shielding package as shown in Figure 3.4, conductively glued on the bottom and on the gold bonding on the top. Hereinafter, the electrode dubbed *back* is that glued on the diamond package, and the electrode dubbed *front* is that on the opposite side. The package hosting the diamond sensor is shielded with a thin aluminium cover, which is further thinned to 190-μm in front of the sensor. This cover has been glued to all sensors used in the experiment and in this work, except for the DC01 diamond (it can be removed or put back for tests). Figure 3.5 shows respectively the diamond package and the aluminium cover. The response of these sensors is compared to that of a silicon diode used as a reference. The diode has a volume of $(5.0 \times 5.0 \times 0.45)$ mm^3, and it is hosted in an aluminium package very close to that of the diamond sensors. Figure 3.6 shows the silicon diode in the package. The silicon diode is a p$^+$-n junction, which consists of a n bulk, a p$^+$ layer obtained by B ion implantation, and a n$^+$ layer

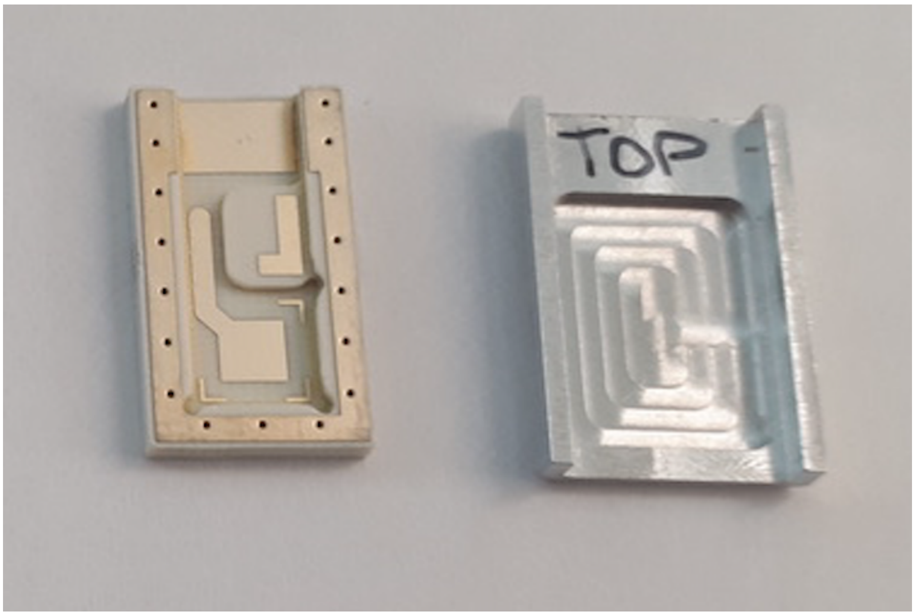

Figure 3.5: The ceramic package without the diamond sensor and the aluminium cover.

	A [cm^2]	Thickness [μm]
Diamond sensor	0.201	500 ± 5
Silicon diode	0.122 ± 0.001	450 ± 10
Aluminium cover	–	190 ± 5

Table 3.2: Values of area and thickness of the diamond sensors and the silicon diode. For the silicon diode the reported value is the effective area as defined in the text. The thickness of the aluminium cover is also reported.

for the ohmic contact. The p$^+$ square region is delimited by guard rings, which aim at reducing the electric field at the junction edges, to collect only the charge produced inside the active volume. This active volume is given by the effective area A_{eff} bounded by the guard rings, and the sensor depleted thickness. The silicon diode is used in reverse bias condition, applying a positive bias voltage to the n$^+$ contact, while both the p$^+$ and the guard rings are connected to ground. For bias voltages higher than 80 V, the diode is fully depleted and the active volume is given by the effective area and the sensor thickness. Table 3.2 reports the dimensions of the diamond sensors and the silicon diode.

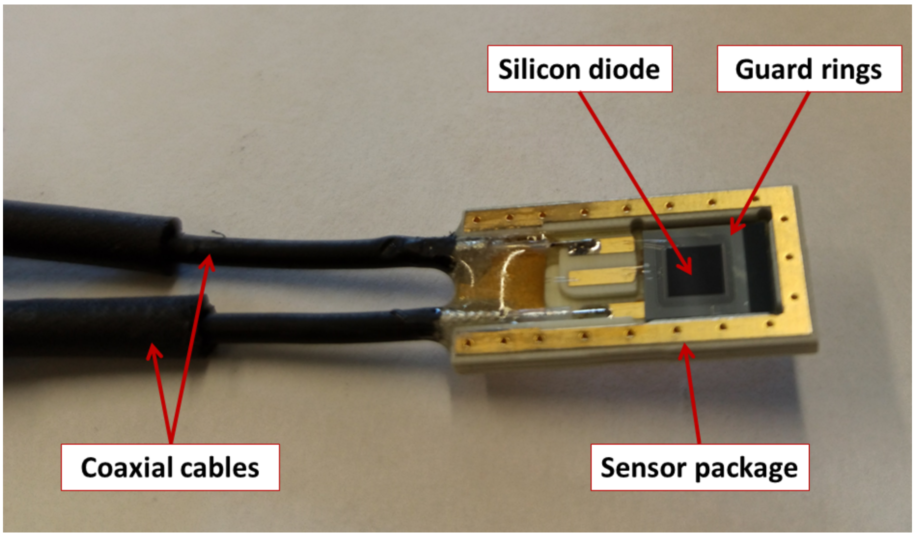

Figure 3.6: Picture of the silicon diode hosted on a package similar to the one of Fig. 3.5, and the coaxial cables connected to the diode electrodes.

Chapter 4

Characterisation with α radiation

This chapter describes the characterisation of the diamond sensor DC01 with a source of α radiation. The study makes use of the transient-current technique to analyse the transport proprieties of the charge carriers in the diamond bulk, separately for el electrons and holes. An estimate the average energy to create an electron-hole pair is reported.

4.1 Method and targets

The method employed for the characterisation with the α source is named transient-current technique (TCT) [44]. The TCT is based on the measurement of the shape of the current pulse induced by the drift of charge carriers, electrons and holes, moving in an uniform electric field generated by a bias voltage applied to the electrodes of the diamond sensor. The technique relies on the production of the charge carriers in a limited region of the sensor at a very small depth from the impinged surface, close to one electrode. According to the sign of the bias voltage, one type of charge carriers is immediately collected by the closer electrode, while the other type drifts through the whole detector bulk up to the back-side electrode. The current signal is almost entirely due to the charge-carrier drift through the detector. The pulse duration equals the time the charge carriers need to traverse the full detector thickness. Since only one type of carrier drifts along the whole bulk, transport properties of electrons and holes can be studied separately.

To stimulate the diamond sensor, I use α particles emitted by an Americium source with an activity of 5 kBq and a half-life of 432.2 years. The decay is

$$^{241}_{95}\mathrm{Am} \rightarrow ^{237}_{93}\mathrm{Np} + \alpha + \gamma\,. \tag{4.1}$$

The energy spectrum of the α radiation features five main monochromatic peaks, whose values and branching fractions are reported in Table 4.1. Since 5.5 MeV α particles have a range of about 15 μm in the diamond crystal, which is small compared to the 500 μm thickness of the sensor, all charge carriers are created close to the impinged surface. This

Energy [MeV]	5.389	5.443	5.486	5.513	5.544
$\mathcal{BR}$ [%]	1.3	12.8	85.2	0.12	0.35

Table 4.1: Energies and branching ratios of the five main peaks of the α-particle from the $^{241}_{95}$Am decay.

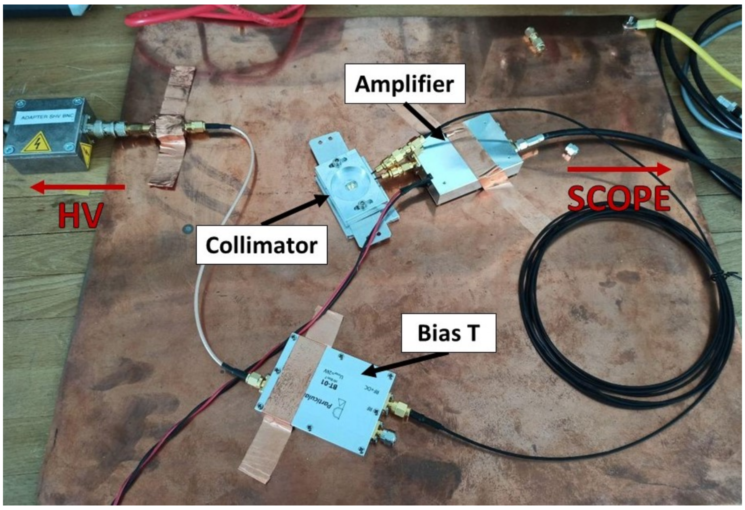

Figure 4.1: Experimental setup for the characterisation with the α radiation. The main components described in the text are identified.

source is perfectly suited for the TCT study because the energy spectrum is rather narrow and produces a large signal over the expected noise.

The targets of the characterisation with the α source are:

Signal-shape analysis to inspect the shape of the signal pulse and spot defects or imperfections of the sensor;

Charge-carrier analysis to measure transport proprieties of electrons and holes separately, such as the drift velocity and mobility, as functions of the bias voltage applied, and to determine featuring parameters like the saturation velocity and low field mobility;

Determination of $\epsilon_{e/h}$, the average energy to create an electron-hole pair. This is achieved by combining charge measurement with simulation and assuming a full charge-collection efficiency.

4.2 Experimental setup and measurement description

The characterisation is carried out only for the diamond sensor DC01. All other sensors are shielded by the aluminium cover glued on the surface, which absorbs all the α radiation. The experimental setup (Fig. 4.1) consists of:

- an aluminium support equipped with a plexiglas collimator, which keeps a minimum distance between the source and the detector, collimating the α particles on the sensor surface;
- a power supply [45] to provide a bias voltage ranging from $-800\,\mathrm{V}$ to $+800\,\mathrm{V}$ to the back-side electrode of the sensor;[1]
- a decoupling circuit that enables the connection of high voltage to the detector. This circuit consists of a low pass RC filter and a bias T [46]; the latter is connected to the diamond sensor through a 5 m cable;

---

[1] The other contact is connected to ground.

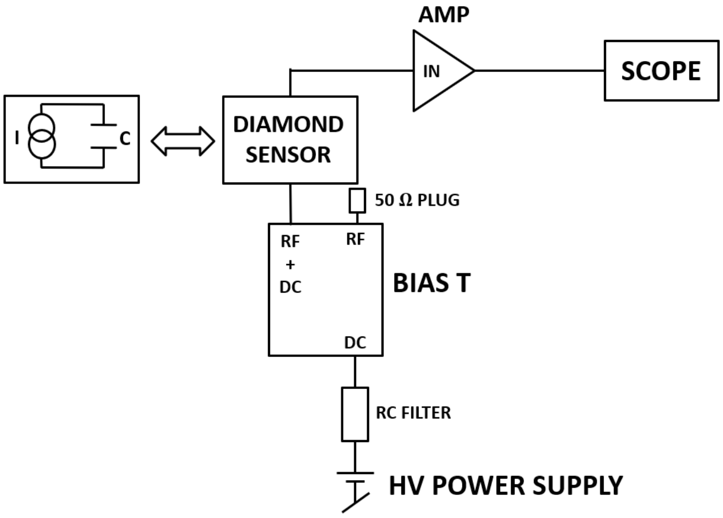

Figure 4.2: Schematic representation of the circuit used for the characterisation with the α radiation. The detector is sketched as a capacitance C and a current source I, the latter provided by the ionisation from the α radiation. The bias voltage is applied on the back-side of the diamond sensor using a bias T, connecting the other side to ground, while the output current is read from the front-side. The current is amplified and the signal is sent to the oscilloscope.

- a current amplifier [47] that amplifies the output current with a 53 dB gain and a bandwidth of 2 GHz;
- a digital oscilloscope [48], with a 3 GHz bandwidth that samples, stores and displays the electric signal at the output of the current amplifier.

The circuit diagram is shown in Fig. 4.2.

A custom collimator is designed in order to minimise the energy loss of the α particles in air and to confine the particle on a small portion of the sensor surface with the maximum incidence angle. The use of the plexiglas allows to get close to the diamond surface without the risk of generating electric arches between the electrodes and the source support. As a drawback, the signal rate is reduced.

The measurement is carried out for different values of bias voltages, V_{bias}. For each voltage, I first set the trigger threshold of the oscilloscope by looking at the noise pulses, without irradiating the diamond sensor. The threshold is chosen to mask the most probable noise-pulse amplitudes so that only signal pulses can be recorded. The trigger threshold is set to -59 mV for the positive polarities and to $+58$ mV for the negative ones. After placing the source to irradiate the sensor, the oscilloscope records the signal pulses generated from the α ionisation, an it averages the signal shapes of about 1000 pulses. The data of the average shape is saved in a file and used in the analysis described in next Section. Figure 4.3 reports an example of two different oscilloscope outputs, obtained with a positive and a negative bias voltage.

The noise amplitude may change during the measurement procedure, since the setup is very sensitive to other electrical devices powered near by. If a noise pulse is recorded and averaged with the signal, the resulting average shape is sculpted. To monitor the trigger threshold, I checked that the average signal area, which is proportional to the charge

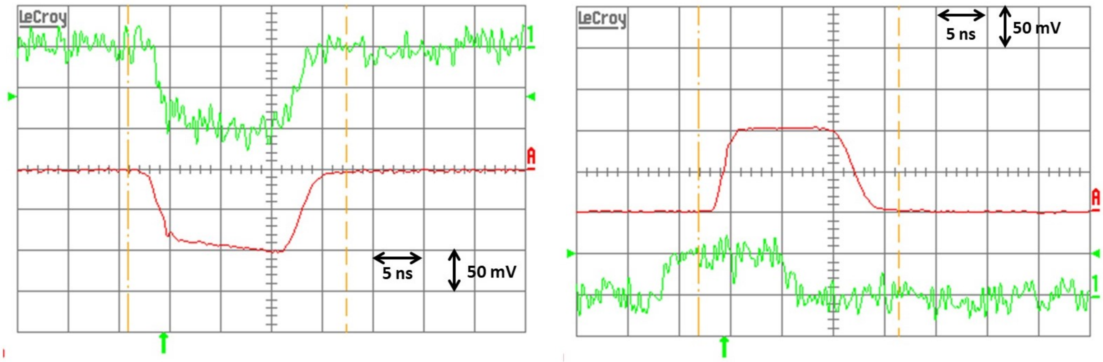

Figure 4.3: Average signal (red) and single signals (green) taken with (left) +200 V and (right) −200 V polarisation bias. In all the measurements the horizontal and vertical divisions are set to 5 ns and 50 mV, respectively.

released inside the diamond sensor, is the same for different measurements with the same polarisation bias.

4.3 Analysis of the signal shape

Figure 4.4 represents the time development of the average signals collected with twelve choices of the polarisation bias. When the back-side electrode is positively biased, holes are immediately collected and drifting electrons induce the electric signal, which has a negative value in output. *Vice versa* for a negative polarisation bias, electron are immediately collected and holes induce a positive output signal.

For an ideal crystal with an uniform electric field, charge carriers are expected to drift with constant velocity v_{drift} and the induced current, given by the Shockley-Ramo theorem [49] as

$$i(t) = -q\, v_{\text{drift}} E\,, \tag{4.2}$$

assumes a constant value as a function of time. The expected signal shape as a function of time should be rectangular, with very fast rise and fall time, corresponding to charge-carriers creation and collection, respectively, and a flat signal shape. However, the observed signals are not perfectly rectangular: they present finite rise and fall times, and a non flat bulk, described as follow.

The signal rise time is approximately constant for all bias voltages suggesting that the rise time is dominated by the time constants of the amplification and readout systems, which are independent from the bias value. An exception is the measurement with $V_{\text{bias}} = +150\,\text{V}$, that presents an higher rising time. In this case the, the rising time is affected by a time jitter, since the signal amplitude is closer to the trigger threshold and noise fluctuations have a significant impact.

The falling edge indicates the arrival of the charge carriers at the back electrode. A longer falling time at lower voltages is related to a wider diffusion of the charge carriers as the drift time increases. For bias voltages higher than 200 V the signals present a similar falling edge, since the carriers are faster collected by the electrodes, limiting their diffusion in the bulk. Due to the higher mobility, hole-induced signals are faster and higher with respect to those induced by electrons at the same bias voltage.

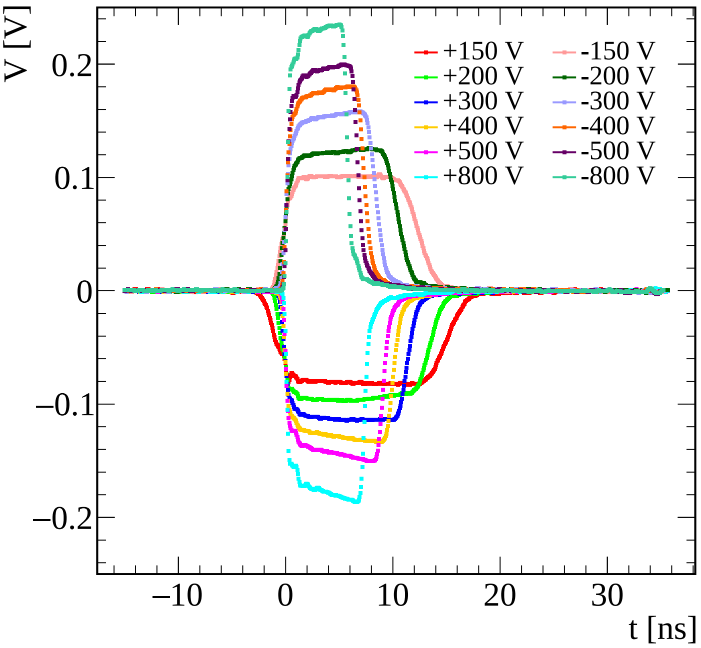

Figure 4.4: Time evolution of the signal pulse induced by charge carriers drifting inside the diamond bulk, for different bias voltages.

Increasing the bias voltage, signals show a non-flat signal core characterised by a significant decrease of the current during the drift for holes, and an increase for electrons. This non-flat signal core can be ascribed to a charge density inside the diamond bulk [44]. Assuming a simple case of an uniform distribution inside the diamond bulk, this charge density leads to a linear dependence of the electric field as a function of the position in the bulk, which causes an exponential increase or decrease of the induced current (*i.e.* of the drift velocities). In particular, an increasing slope is related to a positive charge density, while a decreasing slope to a negative charge density. This effect is called "trap polarisation" and it is related to the fluence, *i.e.* to the total charge collected, and bias voltage which generate the electric field into the detector bulk [50]. This effect can be explained by charge-carriers trapping at local defects of the crystal, which can occur either inside the whole diamond bulk or in the interface between the diamond and the metal electrode. The shape of the electric field varies according to the distribution of the charge density, which depend on the type and distribution of traps, the trapping and de-trapping times, and the rate at which charge carriers are created. If a polarity inversion of V_{bias} is performed between consecutive measurements, the electric field are restored and "trap polarisation" is suppressed. An example is reported in Fig. 4.3, which shows two consecutive measurements done with bias voltages of $+200\,\text{V}$ and $-200\,\text{V}$.

Table 4.2 reports the amplitude, the FWHM, and the area of all signal-shape averages, as a function of the applied bias voltage. These values are used in the following to estimate the charge-carrier proprieties and the average energy to create an electron-hole pair. Assuming similar charge-collection efficiency for each bias value, the area under the signal, which is proportional to the time-integral of the current, is expected to be constant, independently from the bias voltage. All values are indeed in agreement. There is

V_{bias}	Amplitude [mV]	FWHM [ns]	Area [V ns]
+150	-81.27 ± 0.59	16.20 ± 0.30	-1.320 ± 0.020
+200	-95.63 ± 0.58	13.85 ± 0.12	-1.326 ± 0.010
+300	-114.52 ± 0.59	11.55 ± 0.07	-1.323 ± 0.008
+400	-128.14 ± 0.60	10.20 ± 0.05	-1.337 ± 0.007
+500	-143.23 ± 0.60	9.20 ± 0.04	-1.348 ± 0.006
+800	-178.41 ± 0.67	7.35 ± 0.02	-1.348 ± 0.005
−150	100.77 ± 0.72	12.60 ± 0.15	1.285 ± 0.014
−200	122.15 ± 0.86	10.60 ± 0.06	1.328 ± 0.009
−300	154.85 ± 0.90	8.50 ± 0.06	1.332 ± 0.009
−400	175.81 ± 0.80	7.35 ± 0.02	1.321 ± 0.005
−500	196.23 ± 0.75	6.65 ± 0.02	1.326 ± 0.005
−800	231.36 ± 0.69	5.60 ± 0.02	1.325 ± 0.003

Table 4.2: Results of the signal-shape analysis for the different bias voltages.

a small deviation for the value measured at $V_{\text{bias}} = -150\,\text{V}$, that can be due to a smaller charge-collection efficiency. For that bias, the value of the are is about 3% smaller than the average of the value obtained for the other negative biases, where the charge-collection efficiency can be assumed 1.

4.4 Analysis of charge carriers proprieties

The aim of this analysis is to determine the charge-carrier drift properties as a function of the bias voltage. I consider the charge-cloud drifting time as the FWHM of those signals. Knowing the crystal thickness ($d = 500\,\mu\text{m}$), I calculate the drift velocity $v_{e(h)}$ for electrons (e) and holes (h) as

$$v_{e(h)}(E) = \frac{d}{\text{FWHM}} \tag{4.3}$$

Assuming a uniform electric field of strength $E = |V_{\text{bias}}|/d$ generated by the bias voltage, I calculate the charge-carriers mobility $\mu_{e(h)}$ as

$$\mu_{e(h)} = \frac{v_{e(h)}}{E}\,. \tag{4.4}$$

Left side of Fig. 4.5 shows the electron and hole mobilities as functions of the electric-field strength. All measurements present hole mobilities higher than those of electrons; in both cases, a decrease of the mobility is observed as the electric-field strength increases. This phenomenon is not universal [42]: for electric-field strengths lower than roughly $0.03\,\text{V}/\mu\text{m}$ or higher than about $10\,\text{V}/\mu\text{m}$, the electron mobilities are higher than those of holes. This phenomenon is ascribed to the band-structure population that is dependent on the field applied. The electron effective mass varies, hence its mobility.

Right side of Fig. 4.5 shows the drift velocity as a function of the electric-field strength, showing higher values for holes than for electrons. In both cases, the data do not present a linear relation and the drift velocity saturates as the electric-field strength increases. Such a saturation has also been observed in semiconductors like silicon. It has been related to

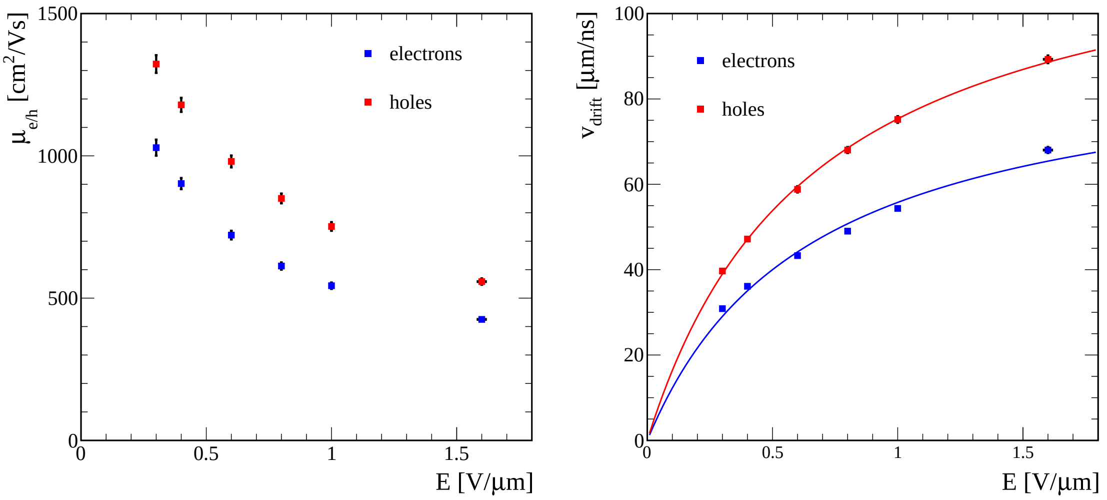

Figure 4.5: Electron and hole (left) mobilities and (right) drift velocities as a function of the electric-field strength. On the right plot, the fit functions defined by Eq. 4.5 are shown.

Drifting charges	μ_0 [cm^2/V s]	v_{sat} [μm/ns]
electrons	1415 ± 37	92.03 ± 1.95
holes	1886 ± 42	125.55 ± 2.40

Table 4.3: Zero-field mobility μ_0 and saturation drift velocity v_{sat} obtained by fitting the drift velocities in Fig. 4.5 with Eq. 4.5.

scattering processes of carriers with crystal defects, impurity atoms, and phonons. A linear relation between the velocity and electric-field strength holds until the drift velocity is less than the thermal velocity. When these velocities are comparable, the time between two collisions involving charge carriers is no longer constant. As the field strength increases, new energy-dissipation channels are opened and the charge carriers can interact with a wider range of normal modes represented by phonons. This leads to the decrease of the carrier mobilities as the field strength grows. When the drift velocity approaches the saturation velocity, it can be described for both electrons and holes by the following empirical expression [44]

$$v_{e(h)}(E) = \frac{\mu_0^{e(h)} E}{1 + \frac{\mu_0^{e(h)} E}{v_{\rm sat}}} , \tag{4.5}$$

where $\mu_0^{e(h)}$ denotes the low-field mobility for electrons and holes, respectively, and $v_{\rm sat}$ the saturation drift velocity. I fit the drift velocities of Fig. 4.5 (left side) with Eq. 4.5, obtaining the results reported in Table 4.3. Both the zero-field mobility and the saturation velocity of holes are higher than those of electrons. The values have the same order of magnitude of the ones obtained in [44], however are not compatible between them. The differences may be explained by differences in the crystal grow, which implies differences in the defects distribution inside the diamond bulk.

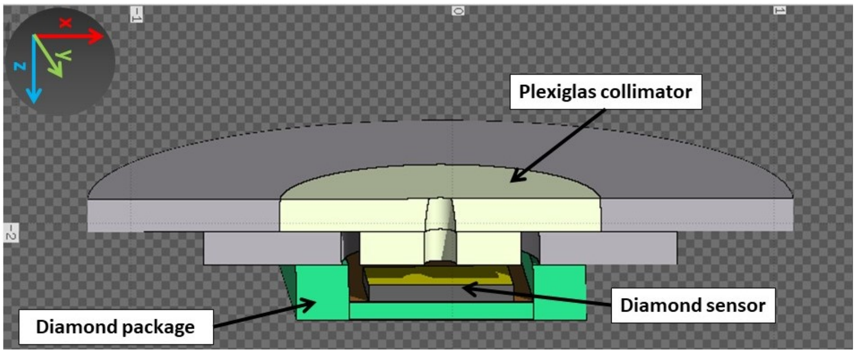

Figure 4.6: 3D section of the simulated setup geometry.

4.5 Average energy to create an electron-hole pair

To determine the average energy to create an electron-hole pair, the charge of the signal pulse is compared with the energy released by the α particle. In the first part of this section, I present the estimate of this energy with a simulation. Afterwards, the charge collected at each bias voltage is calculate, and the average energy to create an electron-hole pair is derived.

4.5.1 Mean released energy per α particle

A full simulation of the experimental setup is used to estimate the mean energy released per α particle in the diamond, taking into account the energy loss in air, the geometry of the collimator and the interaction with its material, and that with the electrodes. The simulation exploits the Monte-Carlo simulation package "Fluka" [51].

The geometry of the system as implemented in the simulation is represent in the 3D section in Fig. 4.6. The reference frame is chosen so that the x-y plane is parallel to the sensor surface. The diamond sensor is defined as a 500-μm thick diamond crystal with 3 metallic contact layers (see Sec. 3.4). The active part of the source is simulated as a 0.35 mm-radius disk placed at 0.6 mm from the plexiglas collimator. The α particles are generated with an isotropic angular distribution. A platinum disk is placed behind the source, to simulate the support and to take into account possible back-scattering of the α particle.

The energy spectrum of the α particles is simulated with five narrow peaks centred at the corresponding values of Tab. 4.1. For each of the five energy values in the spectrum, I generate a sample with 45×10^6 α particles. I sum the released energies from the 5 samples, each weighted with the branching ratio corresponding to the simulated energy peak, to obtain the total distribution of the released energy.

For each generated α particle, the simulation gives the energy released inside the detector volume, and also in all materials traversed by the particle along its path. Figure 4.7 shows the energy released in the two dimensional sections of the detector, obtained splitting the detector volume into $100 \times 100 \times 500$ volumes (bins) along x, y and z, respectively, and recording the total released energy density in each bin. The irradiated zone (x-y section on the left side of the figure) is limited to a circular area due to the focus of the collimator. In the longitudinal section (on the right side of the figure), the energy loss is limited to a depth of about 15 μm, which corresponds to the typical range of α particles in diamond. A fraction 93.4% of the total energy of the α particle is released on average in the diamond;

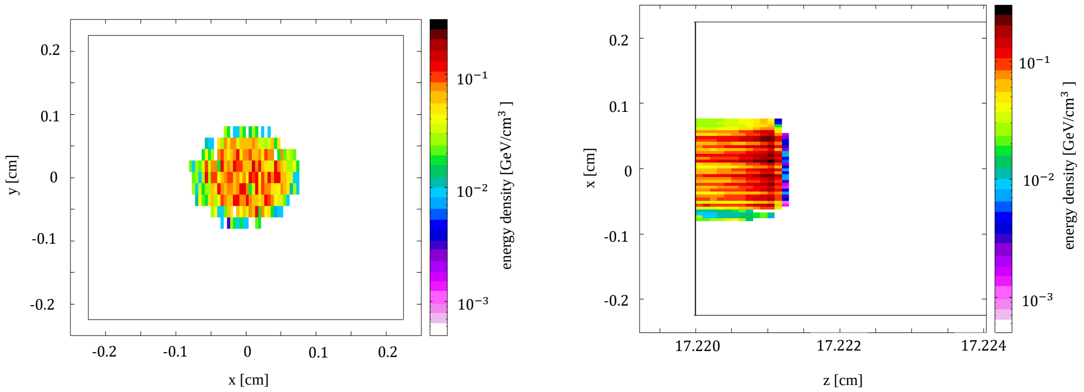

Figure 4.7: Two dimensional profile of the released energy per unit volume (color scale) in the diamond volume from simulation, (left) for a transverse section x-y and (right) a longitudinal section x-z of the diamond bulk. The distribution are obtained by the generation of 4.5×10^7 α particles of 5.486 MeV.

4.1% in the metallic contacts, and 2.5% in air.

The distribution of the released energy inside the diamond volume is reported in Fig. 4.8. The mean energy released in the diamond is obtained from this distribution. The spectrum presents a dominat peak around 4.9 MeV and long tail at energy lower than 4.8 MeV. The trigger threshold set on the scope must be considered to cut the distribution at a certain value of energy. Since for different bias voltages the signal amplitude change, the trigger level set in mV on the oscilloscope has a differnt cut value in MeV. A linear relation is assumed

$$T_{\mathrm{mV}} : A_{\mathrm{mV}} = T_{\mathrm{MeV}} : E_{\mathrm{dep}}^{\mathrm{mean}} , \tag{4.6}$$

where T_{mV} is the trigger threshold of the oscilloscope, A_{mV} is the signal amplitude and T_{MeV} is the cut in distribution. The cuts estimated for each bias voltage and the corresponding mean energy in the range $[T_{\mathrm{MeV}}, 5.5]$ MeV, are reported in Table. 4.4. These values are used in the following to determine the average energy required to generate an electron-hole pair.

4.5.2 Determination of the mean energy to create an electron-hole pair

The charge collected at the electrode is calculated from the signals-shape average, considering the data in Table 4.2. Given the area A under the signal (in V ns), a coupling impedance $R = 50\,\Omega$ and the amplifier gain $G = 53$ dB, the collected charge Q is given by

$$Q = 10^{-G/20} \frac{A}{R} , \tag{4.7}$$

The charges are reported as a function of the electric-field strength in Fig. 4.9 for electron- and hole-induced signals. The charge values saturate at electric fields higher than 0.4 V/μm. The average value of the charge is 60.01 ± 0.17 fC and 59.29 ± 0.13 fC for electron- and hole-induced signal, respectively. The fractional difference between the charges does not exceed 1.2%.

Assuming fully efficient-charge collection from the diamond bulk, I evaluate the energy needed to create an electron-hole pair $\epsilon_{e/h}$. This is determined by the ratio of the released

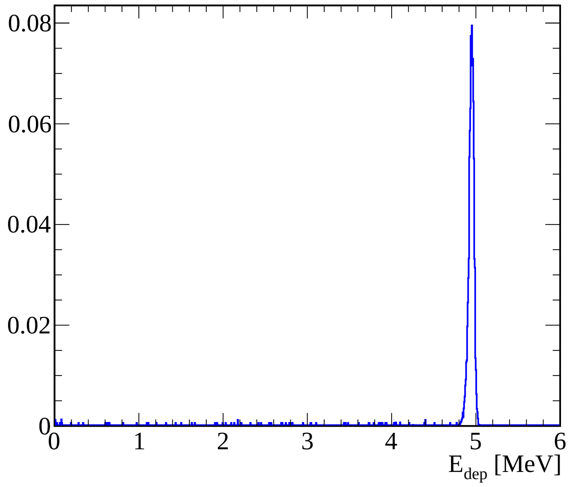

Figure 4.8: Distribution of the mean released energy of α particles from simulation.

energy $E_{\text{dep}}^{\text{mean}}$, estimated with simulation and reported Tab. 4.4, with the number of charge carriers, obtained from the ratio Q/e,

$$\epsilon_{e/h} = \frac{E_{\text{dep}}^{\text{mean}}\, e}{Q}\,, \tag{4.8}$$

where e is the elementary charge. The values of $\epsilon_{e/h}$ as a function of the electric-field strength are shown in Fig. 4.9 (right side), for electron- and hole-induced signals. The values are averaged to obtain

$$\epsilon_{e/h}^{e} = 13.06 \pm 0.04\,\text{eV} \tag{4.9}$$

$$\epsilon_{e/h}^{h} = 13.18 \pm 0.03\,\text{eV}\,, \tag{4.10}$$

respectively. The two values agree within 2.5 standard deviations. No systematic uncertainty is associated to these measurements and the overall uncertainty is perhaps underestimated. Nevertheless, these values are in very good agreement with the known value for diamond of about $\epsilon_{e/h} = 13\,\text{eV}$ [52], although different numbers have been reported in literature, spanning from 12 eV to 17 eV [42] depending on the crystal quality and possible systematic effects.

V_{bias} [V]	E [V/μm]	T_{MeV} [MeV]	$E_{\text{dep}}^{\text{mean}}$ [MeV]
+150	0.3	3.53	4.931 ± 0.003
+200	0.4	3.00	4.924 ± 0.004
+300	0.6	2.51	4.911 ± 0.005
+400	0.8	2.24	4.905 ± 0.006
+500	1.0	2.01	4.893 ± 0.007
+800	1.6	1.61	4.883 ± 0.008
−150	0.3	2.85	4.922 ± 0.004
−200	0.4	2.35	4.907 ± 0.006
−300	0.6	1.86	4.888 ± 0.008
−400	0.8	1.63	4.885 ± 0.008
−500	1.0	1.46	4.881 ± 0.009
−800	1.6	1.24	4.875 ± 0.009

Table 4.4: Mean released energy ($E_{\text{dep}}^{\text{mean}}$) of α particles from simulation. The trigger thresholds (T_{MeV}) to cut the distribution of released energy is calculated for each bias voltage.

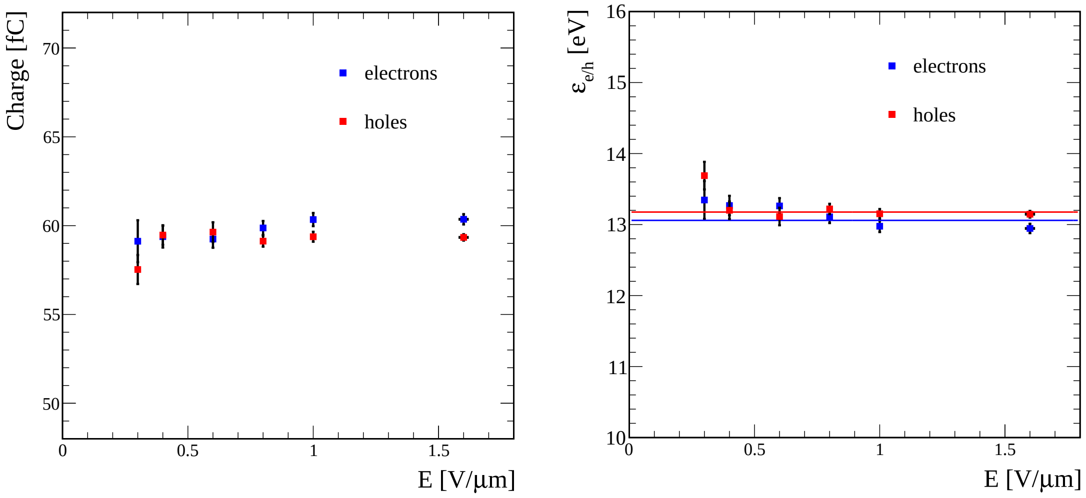

Figure 4.9: (Left) Charge as functions of the electric-field strength for electron- and hole-induced signals. (Right) Mean energy to create an electron-hole pair as a function of the electric-field strength for electron- and hole-induced signals. The lines are the average values.

Chapter 5

Characterisation with β radiation

This Chapter describes the characterisation of the diamond sensors using a source of β radiation in three steps. I study the stability of the output current generated by the ionisation of the diamond bulk by a constant flux of β particles. I verify the dependence of the output current on the radiation flux. Finally I compare the diamond current with that from a silicon diode, with the the same detector package and geometry. In this way the silicon diode can be used as a reference to characterise the response of the diamond sensors, minimizing the uncertainties of the β source itself. This is the first time that this comparison is employed to characterise our diamond-sensor response.

5.1 Source and analysis targets

To characterise the response of the diamond sensors to charged particles, I used a source of strontium-90, ^{90}Sr, that provides electrons from the chain of two subsequent β decays

$$^{90}_{38}\mathrm{Sr} \rightarrow ^{90}_{39}\mathrm{Y} + e^- + \bar{\nu}_e\,, \tag{5.1}$$

$$^{90}_{39}\mathrm{Y} \rightarrow ^{90}_{40}\mathrm{Zr} + e^- + \bar{\nu}_e\,, \tag{5.2}$$

with a nominal activity of 3.3 MBq. The decay of the strontium atom into a yttrium isotope has a half-life of 28.8 years and a Q-value energy of 546 keV. The second decay, involving the decay of the yttrium to a zirconium isotope, has a half-life of 64 hours and a Q-value energy of 2282 keV. Figure 5.1 shows the energy spectrum of the electrons from the decays. Two structures are visible, one related to the strontium decay into yttrium at lower energies, and one related to the yttrium decay into zirconium at higher energies. The extension in energy of these two structures is limited by the Q-value.

The characterisation with this source aims at:

- testing the stability of the response of the diamond sensors irradiated with high fluxes of charged particles;
- verifying the diamond sensors response for different intensities of the particle flux, performing measurement of output current varying the relative distance between the source and the detector;
- comparing the output current of the diamond sensors and that of a silicon diode, used as a reference, to characterise the response.

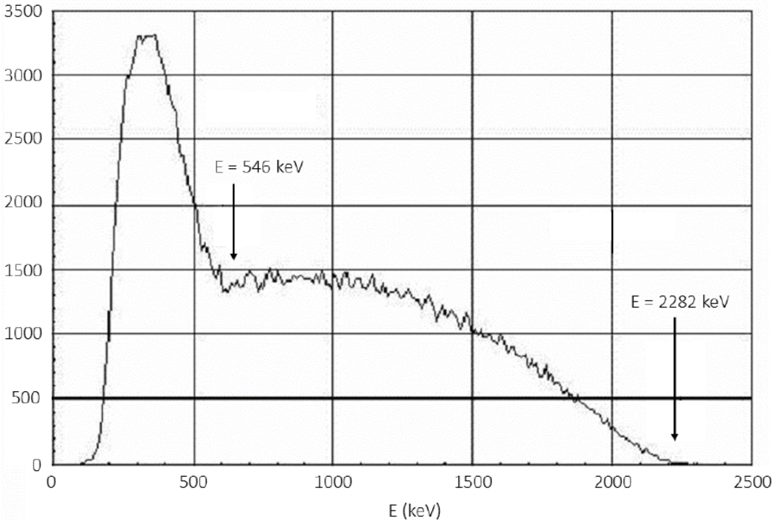

Figure 5.1: Electron energy spectrum from the strontium-90 decay

5.2 Experimental setup

All diamond sensors (DC00, DC01, DC15, and DC25) and the silicon diode described in Sect. 3.4, are used. In addition, the experimental setup consists of:

- a power supply [45] to provide a bias voltage to the diamond sensors and the silicon diode;
- a 4-channels picoamperometer (model AH501 provided by Sincrotrone Trieste) [53],that measures bipolar currents ranging from $\pm 2.5\,\text{nA}$ to $\pm 11\,\text{mA}$ and with a sampling frequency up to 23 kHz. This device is controlled via software to select several parameters, such as the current range (three ranges are available: $\pm 2.5\,\text{nA}$, $\pm 6.4\,\mu\text{A}$, $\pm 11\,\text{mA}$), number of input channels, sampling frequency and time interval for data averaging, yielding in output the mean value and the standard deviation of the downsampled current obtained averaging;
- an aluminium support to host the detector in the desired position aligned to the β-source;
- a stepper controlled via software with “Arduino”, which moves the source support to vary the distance between the source and the detector.

The detector and the source are placed in a shielding plexiglas box. The $(37 \times 22 \times 22)\,\text{cm}^3$ box has 1-cm-thick walls, which absorbs completely the radiation emitted by the β-source and avoids any accidental contact with the source itself. Figure 5.2 shows the experimental setup and the positioning of the source with respect to the detector surface. The moving source support plays a pivotal role in the calibration process, since it is possible to change the flux intensity of β radiation on the sensor surface by varying the relative distance between the source and the detector, kept fixed once hosted in its aluminium support.

5.3 Measurement methods

The characterisation features two sets of measurements, dubbed *stability* and *I-d* measurements. The stability measurements test whether the output current is stable as the

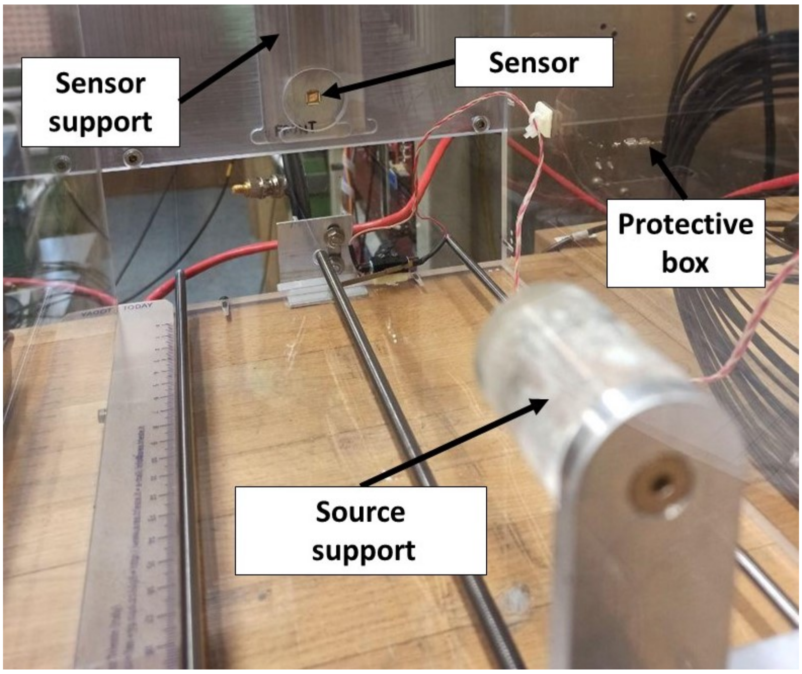

Figure 5.2: Experimental setup for the characterisation with β radiation.

radiation flux absorbed by the detector is constant. The I-d measurements targets to verify the relation between the sensor output current (I) and the relative distance between the source and the detector (d), *i.e.* the dependence of the current on the particle flux. The I-d measurements has been performed also with the silicon diode, to set a reference for the characterisation of the diamond sensors.

In all measurements two opposite bias voltages ±100 V are used. The bias is always applied to the back side of diamond sensors; the other side is set to ground. The measurements with opposite biases are done at the same source-detector distance, as to test the symmetric response of the sensors. The silicon diode is used only for I-d measurements with a 100 V bias applied. In this case the sensor is very stable, so a dedicated stability study is not needed; moreover a special care has been kept in order to avoid a long exposure to β radiation thay may damage the silicon bulk and increase the leakage current. The output current from the diamond sensors and the silicon diode are measured with the picoamperometer using a sampling time of 1 s.

The protective box in plexiglas shields the β radiation, but it is transparent to visible light. This light would produce undesired extra currents in the detectors without package cover if the environment is not properly darken. The measurements with the sensor DC01 and the silicon diode without the aluminium cover are thus carried out covering the full box with several black cloths, to reduce light contamination to a negligible level.

The procedure for the two sets of measurements are briefly outlined in the following.

Stability: I place the source at 4.0 mm from the diamond sensor, to guarantee the minimum space necessary to slide a 3.0mm thick copper shutter between the source and the sensor.[1] A dark current measurement is performed by sampling the output current for a period of 10 minutes, using the shutter to shield the β radiation. Afterwards, the shutter is removed, while I keep sampling the output current. The current

---

[1] The source is placed at a distance of 5.0 mm from the source only for the sensor DC01 without the aluminium cover, to avoid the saturation of the picoamperometer in its most accurate range ±2.5nA.

is measured for a period of 1-2 days in these conditions.

I-d measurement: After applying the bias voltage, a measurement of dark current is done placing the source at a distance of 25.5 cm from the sensor and sampling the output current from the sensor for a time period between 3 and 5 minutes.[2] Then, the source is moved close to the sensor at a distance of 4.5 mm, and the output current is measured for 1 minute; the measurement is repeated for by increasing the distances with steps of 1.0, 2.0, 5.0, and 10.0 mm. After the measurements, a second measurement of the dark current is performed, at a distance of 25.5 cm.

The stability measurements are carried out with all diamond sensors, DC01, DC00, DC15 and DC25. The I-d measurements are done with the sensor DC01 and the silicon diode without the aluminium cover. As a reminder, the aluminium cover is permanently glued to the detector package for all the other diamond sensors. The diamond sensors often suffer complex hysteresis effects due to trapping or un-trapping of the charge carriers [34]. These effects are particularly evident when their operation conditions are changed. In order to minimize such hysteresis effects due to bias-voltage changes and to operate in more stable conditions, the I-d measurements are performed always after a stability measurement for each diamond voltage.

5.4 Analysis of the stability measurement

The values of the measured output current, I_{diam}, are plotted as a function of the irradiation time, t, and they are shown in Figs. 5.3 and 5.4 for all diamond sensors. In these plots, the uncertainty associated to each value of the output current is measured from the distribution of the values of I_{diam} in the stabilisation range, where present, or in a range of roughly constant values of I_{diam}. The standard deviation of this distribution is preferred than the uncertainty associated by the picoamperometer because the fluctuations of the output current are dominated by electronic noise associated to the acquisition setup.

In all plots, an initial value of the output current distributed around zero, corresponding to the dark current measurements, is visible; after a certain time (between 500 and 1000 s, changing for each measurement), the output currents suddenly have nonzero values, and this corresponds to the removal of the copper shutter. The only exception is given by the measurements with the DC01 without cover, where the region with no current is not visible, because it was not possible to use the shutter to shield the sensor.

Different results are obtained for the sensors, and also for the different bias polarisation on the same sensor. The diamond sensor DC01 with the negative bias reaches a stable value of the output current (Fig. 5.3, top-right), while with a positive bias the sensor delivers an unstable output current (Fig. 5.3, top-left). This test highlights a preferred configuration with negative biases for this diamond sensor. Such an asymmetry might depend on subtle surface treatment or on crystal growing effects of the sensor, which vary from crystal to crystal. A diamond sensor may display a symmetric response for the two polarities, such as for the plots of the sensor DC00 shown in the second row of Fig. 5.3. The current profile is very close to that expected for an ideal crystal, where a stable output is reached in a very short time, and its absolute values is the same when changing the sign of the bias applied. This symmetric behaviour features a very steep transient time for each polarisation. Longer

---

[2] At this distance, the radiation flux on the sensor is below the measured sensitivity, since the output current does not present significant variations when the source is moved by ±1 cm. The major contributions to this current may be associated to residual visible light and to the leakage current.

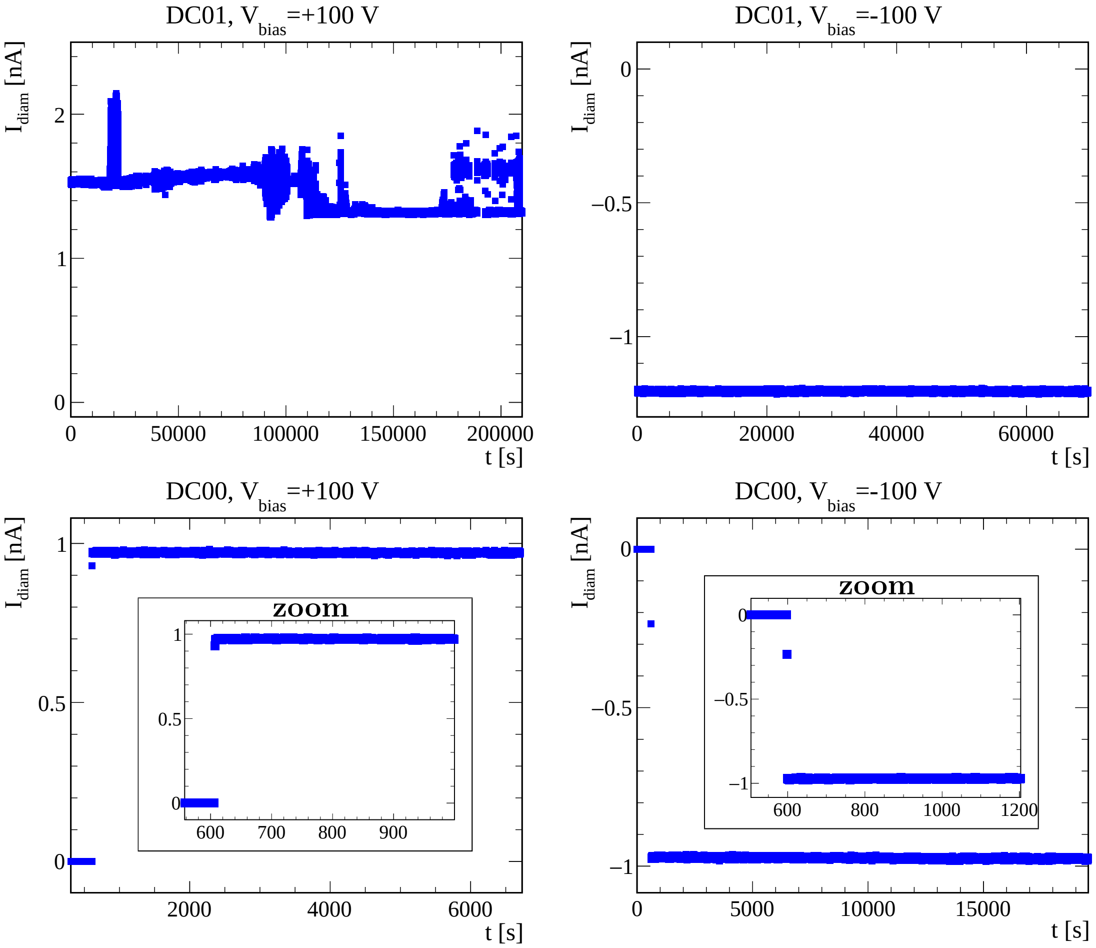

Figure 5.3: Output current I_{diam} as a function of the irradiation time t for (first row) the sensor DC01 and (second row) DC00, irradiated with a constant flux of β particles. On the left plots, a bias $V_{\text{bias}} = +100\,\text{V}$ is applied; on the right plots, the bias is $V_{\text{bias}} = -100\,\text{V}$. The box plots show a zoom of the transient region of the output current.

transients time to reach a stable output may be seen, as for the measurement in Fig. 5.4, top-left, which reports the case of the sensor DC15 with a positive bias. With opposite polarisation, the output current never reach a stable value, with fluctuations around 8%. Finally, on the second row of Fig. 6.4, the measurements show that the sensor DC25 does not present a good stability of the output current for the negative polarisation (left), while the positive polarisation shows more stable conditions.

An heuristic description of a long transient time in a diamond sensor is given by a model where the transient time is due to defects in the crystal lattice, which can introduce variations in the crystal energy levels. These defects, that are located in the band gap, are also named *traps*, because they can trap the charge carriers. Two types of traps are generally identified: the superficial traps, situated near the valence band or the conduction band, and the deep traps, situated in the central zone of the band gap. As the diamond crystal is irradiated, these energy levels trap electrons and holes, decreasing the output current. By filling the traps with charge carriers generated by continuous radiation, the output current rises, achieving a stable value when there are no empty traps anymore. This

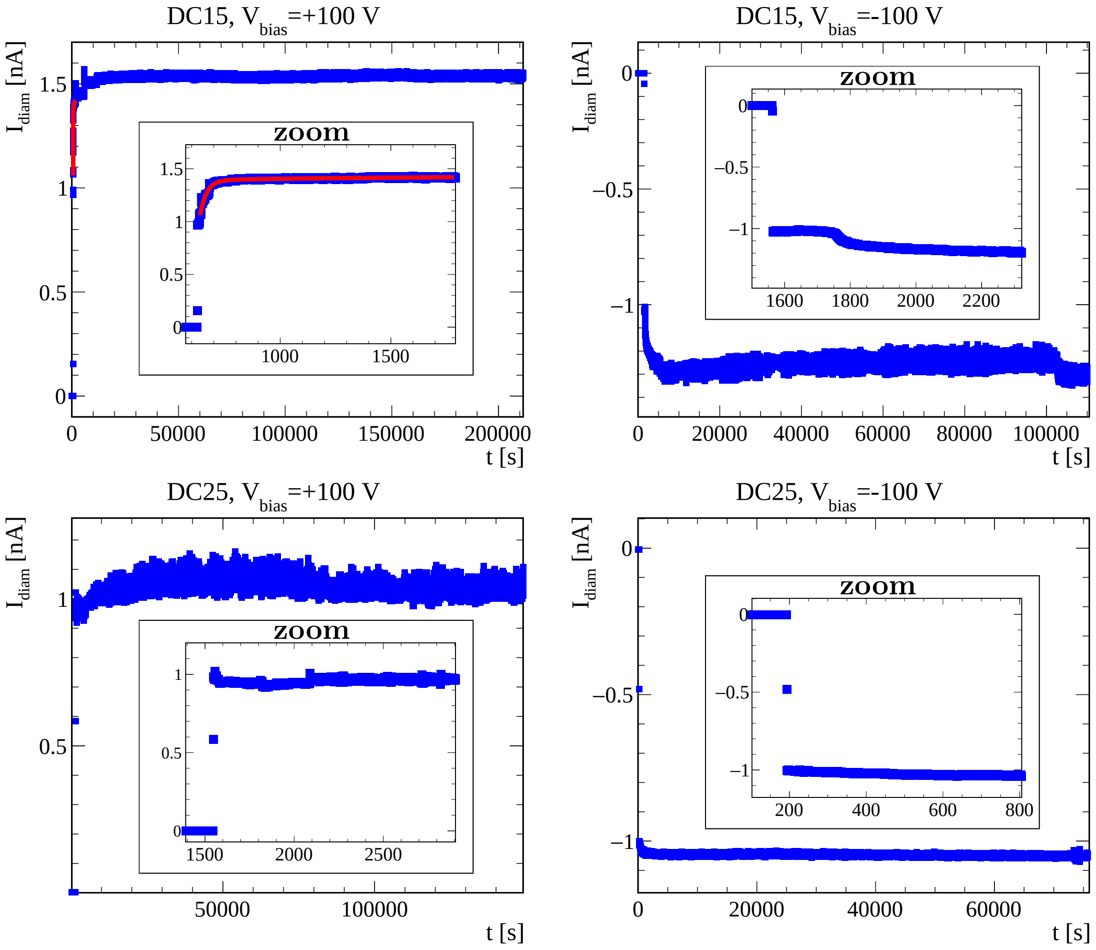

Figure 5.4: Output current I_{diam} as a function of the irradiation time t for (first row) the sensor DC15 and (second row) DC25, irradiated with the β source placed at 5 mm from the detector support. On the left plots, a bias $V_{\text{bias}} = +100\,\text{V}$ is applied; on the right plots, the bias is $V_{\text{bias}} = -100\,\text{V}$. The inset plots show a zoom of the transient region of the output current. The current profile of the sensor DC15 for the positive polarisation is fitted using Eq. 5.3.

phenomenon is empirically modelled by the following expression

$$I_{\text{diam}}(t) = I_0 \left(1 - w_s\, e^{-\frac{t-t_0}{\tau_s}} - w_d\, e^{-\frac{t-t_0}{\tau_d}} \right) , \tag{5.3}$$

where I_0 is the asymptotic current values; w_s and w_d are the proportions of superficial and deep traps; τ_s and τ_d the corresponding time constants to fill the two categories of traps; and t_0 is the origin time (start of the irradiation). The output-current profile of the sensor DC15 with positive polarisation if fitted using Eq. 5.3 as shown in the zoom of Fig. 5.4. The long-time constant takes a value of 700 s; the short-time constant of 30 s.

Summary

The results of the stability measurements are summarised as follows:

DC00 very stable output current and sharp transient time on both polarisation biases; very symmetric response; close to an ideal crystal;

DC01 negative bias preferred: sharp transient time and stable output current with this polarisation; unstable output current with a positive bias;

DC15 long transient time for both polarisation biases; positive bias reaches a stable output current, while negative bias presents unstable currents;

DC25 stable output current with negative bias; unstable output currents with negative bias polarisation.

5.5 Analysis of the I-d measurements

In the I-d measurements, the output current is measured for about 1 minute, yielding about 60 values of the current, for a given source-detector distance d. For each sample, the mean output current, I_{mean}, and the associated uncertainty, the error on the mean $\sigma_{I_{\text{mean}}}$, are calculated. With the same method, the mean dark current and its uncertainty, $I_{\text{dark}} \pm \sigma_{I_{\text{dark}}}$, are calculated from the output currents measured before and after the I-d measurements, at a distance $d = 25.5$ cm. This offset is subtracted to each value I_{mean}, to obtain the current I^*_{mis} and the associated uncertainty,

$$I^*_{\text{mis}} = I^*_{\text{mean}} - I^*_{\text{dark}} \tag{5.4}$$

$$\sigma_{I^*_{\text{mis}}} = \sqrt{\sigma^2_{I_{\text{mean}}} + \sigma^2_{I_{\text{dark}}}} \tag{5.5}$$

A note on the dark current for the silicon diode. The value of I_{dark} obtained before the set of I-d measurements is observed to be 52% smaller than that measured after them. This is because of the radiation damage from the β particles. I decided to subtract the dark current measured at the end of the I-d measurements, since the effect of the dark current is higher for the measurement at higher distances, those performed towards the end. For the diamond sensors, the value of dark current before and after the I-d measurements is the same.

The measured current I^*_{mis} are plotted as a function of d in Fig. 5.5 for the sensor DC01 and the silicon diode, both without aluminium cover. The data follows a relation typical for a dependence on the inverse square of the distance, d^2, which is expected from the variation of the flux with the distance. This can be parametrised as

$$I^*_{\text{mis}} = \frac{A}{(d - d_0)^2} + I_0\,, \tag{5.6}$$

where A is a normalisation constant, d_0 is a position offset, and I_0 is a current offset. Such a relation needs a correction to account for the fraction of solid angle subtended by the detector surface and a point-like source at small distances. This is calculated in Ref. [**?**]. Given such a correction, the output current depends on the distance as

$$I^*_{\text{mis}} = 4A' \arctan\left(\frac{A_{\text{eff}}}{2(r - d_0)\sqrt{4(r - d_0)^2 + 2A_{\text{eff}}}}\right) + I_0\,, \tag{5.7}$$

where A' is another normalisation constant, and A_{eff} is the effective surface of the detector. I fit the data using this function and the results are reported in Tab. 5.1.

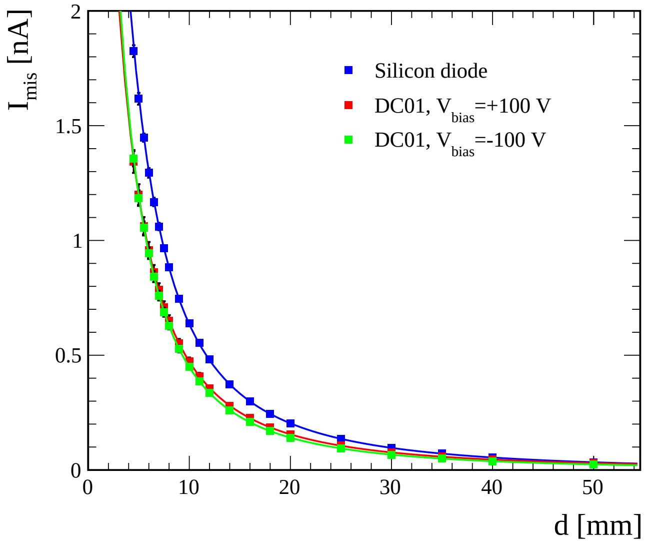

Figure 5.5: Measured current as a function of the detector-source distance d for the silicon diode (blue) and the sensor DC01 with opposite polarisation biases (red and green). The curves resulting from the fit with Eq. 5.7 are also drawn.

Detector	V_{bias}	Fit parameters		
		A' [nA mm^{-2}]	d_0 [mm]	I_0 [pA]
Silicon diode	+100 V	3760 ± 60	-3.37 ± 0.10	-6.5 ± 0.8
DC01	+100 V	1710 ± 70	-3.46 ± 0.21	0.2 ± 1.6
DC01	−100 V	1760 ± 50	-2.95 ± 0.10	-2.6 ± 1.2

Table 5.1: Results of the fit with the function of Eq. 5.7 to the I-d measurements for the silicon diode and the diamond sensor DC01.

The output currents measured from the sensor DC01 for the two polarisation biases presents similar values at the same source distance. The normalisation factors A' is found to have values compatible between each other for the sensor DC01 with different polarisation biases; that of the silicon diode is as twice as large, in agreement with the factor between the measured output currents.

The position offset d_0, which values are fount to be about 3 mm in all fits, are consistent with the distance from the detector surface and the zero-position from which the distance d is measured in the experimental setup. This offset takes into account also possible misalignment of the detector with respect to the source. The offset current I_0 takes values compatible with zero for the diamond sensor, while for the silicon diode it is significant larger. This is explained by the dark current.

The output current from the I-d measurements are combined with the simulation results described in the next Section to compare the diamond sensor response to the that of the silicon diode. Since the output current measured with the silicon diode at a source distance higher than 30 mm are comparable with the dark current, these measurements are not considered in the rest of the analysis.

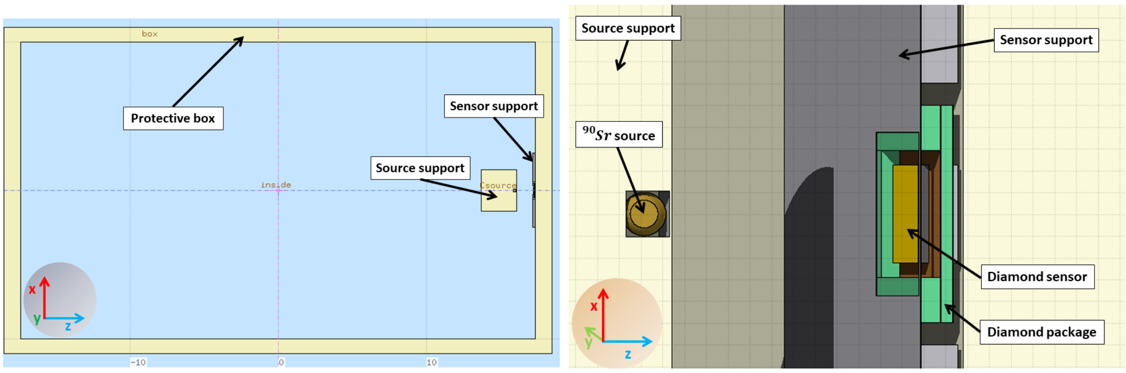

Figure 5.6: Sketch of the experimental setup implemented for the simulation (left) and magnified 3D sketch highlighting the source and the diamond sensor configuration (right).

5.6 Simulation of the released energy per decay

In this Section, I estimate the energy released by a β particle in the active volume of the diamond sensor and of the silicon diode, considering the geometry of the experimental setup. This energy is calculated per single β decay, hence it is called "released energy per decay" (REPD), such that the total energy absorbed by the sensor per second is the REPD multiplied by the source activity. The source activity is not know. However, by using the silicon diode as a reference, only an estimate of the REPD is needed. This is explained in Sect. 5.7, where the REPD is used to characterise the diamond sensor response.

To estimate the REPD I wrote a simulation by using the Fluka software [51] to model the experimental setup. Figure 5.6 shows a 3D section of the experimental setup, which includes the protective box, the aluminium support for the sensors and the plexiglas support for the source. The whole system is place in air. The diamond sensor is defined as in the simulation described in Sect.3.4, while the silicon diode is defined as a rectangular box of silicon with an area of $0.25\,\mathrm{cm}^2$ and a thickness of $450\,\mu$m. A layer of silicon oxide, which should be present on the surface of the detector, is not simulated, since the energy lose in its thickness does not affect in a significant way the electron energy.

The active part of the source is modelled as a 0.5 mm radius sphere of $^{90}_{38}$Sr. The strontium β decay is implemented in Fluka. It generates an electron energy spectrum as that shown in Fig.5.1, isotropically distributed over the solid angle. The strontium sphere is inserted in a support that, along with a cover, completes the source geometrical description.

I generated 4.5×10^7 decays at each source-detector distances of the I-d measurements. For each generated decay, the simulation accounts for the energy loss in the crossed materials implemented in the simulation. The comparison with the measurements is then done with an accurate definition of the energy released inside the detector active volume. While for the diamond sensor the active volume corresponds to the entire volume, for the silicon diode the active volume is bounded by the guard rings (see Sect. 3.4) and the depletion thickness. Since the silicon diode is operated in full depletion, the active volume is given by the product of the effective area ($A_{\mathrm{eff}} = 0.122\,\mathrm{cm}^2$) and the silicon diode thickness. The resulting distribution of released energies is normalised by dividing the integral with the total number of generated decays, such that it represents the REPD distribution. Figure 5.7 shows the REPD distributions in the silicon diode (left) and in the diamond sensor (right), for a source-detector distances of 4.5 mm (blue) and 30.0 mm (red). For both detectors, the integral, which represents the REPD flux, is attenuated by a factor 22 moving the source

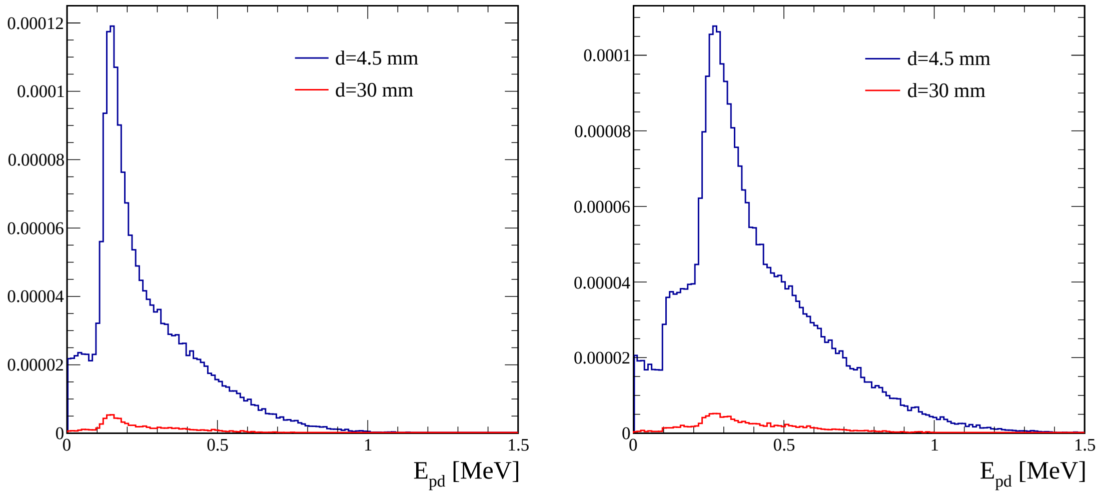

Figure 5.7: Distribution of REPD obtained with simulation for the minimum and maximum source-detector distance, $d = 4.5\,\mathrm{mm}$ and $d = 30.0\,\mathrm{mm}$, respectively for the silicon diode (left) and the diamond sensor (right).

from the minimum to the maximum distance. This effect is mainly due to the geometrical acceptance, since increasing the distance between the source and detector, decreases the number of β particle impinging the detector. The peak of the distribution also move at lower values due to a larger energy loss in air at higher distances.

The REPD for a given detector, $E_{\mathrm{pd}}^{\mathrm{det}}$ ("det" is either the diamond sensor or the silicon diode), is calculated by integrating the energies of the corresponding distribution $(\mathrm{d}n/\mathrm{d}E)|_{\mathrm{det}}$,

$$E_{\mathrm{pd}}^{\mathrm{det}} = \int_{E_{\mathrm{min}}}^{E_{\mathrm{max}}} E \left.\frac{\mathrm{d}n}{\mathrm{d}E}\right|_{\mathrm{det}} \mathrm{d}E\,. \tag{5.8}$$

Figure 5.8 reports the values of REPD as a function of the source distance for the two different detectors. The simulation takes into account the full geometry of the apparatus and indeed the values of REPD found follow the expected trend as a function of the distance, similar to that of the measured current. The simulated data are fit well with Eq. 5.7. The released energies have higher values in the diamond sensors than in those in the silicon diode because of the larger effective volume of the detector.

The uncertainty associated to $E_{\mathrm{pd}}^{\mathrm{det}}$ is calculated assuming that the dominant source of uncertainty is caused by the uncertainty on the active volume of the silicon and diamond detectors. While for the diamond sensor the dominant uncertainty is given by the uncertainty on the thickness, for the silicon diode a not negligible component is given by the uncertainty on the effective area (see Sect. 3.4). On the basis of these considerations, the uncertainty associated to $E_{\mathrm{pp}}^{\mathrm{Di}}$ has been calculated as the maximum difference between $E_{\mathrm{pp}}^{\mathrm{Di}}$ for a thickness x_{Di} and that for $x_{\mathrm{Di}} \pm \Delta x$, where Δx is the x uncertainty. For the silicon diode, since it is necessary to consider also the contribution related to the uncertainty on the effective area, the uncertainty associated to $E_{\mathrm{pp}}^{\mathrm{Si}}$ is given by the maximum difference between $E_{\mathrm{pp}}^{\mathrm{Si}}$ for a thickness x_{Si} and an effective area A_{eff} and that obtained for the four combination of $x_{\mathrm{Si}} \pm \Delta x$ and $A_{\mathrm{eff}} \pm \Delta A_{\mathrm{eff}}$. I estimated an uncertainty on the REPD of 3% for the silicon diode and of 1% for the diamond sensor.

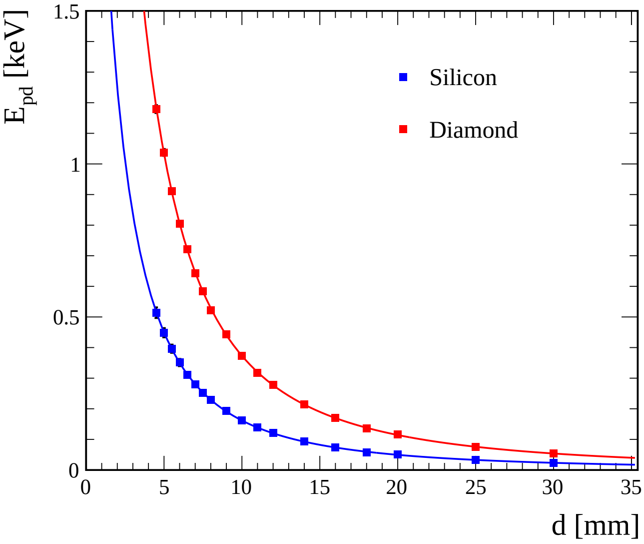

Figure 5.8: Estimated values of REPD for as a function of the detector-source distance for the diamond sensor and the silicon diode. The curve are the result of the fit with Eq. 5.7.

5.7 Comparison of diamond and silicon response

In this Section, I compare the output current from diamond sensors and the silicon diode, used as a reference, to infer information on the diamond-sensor response to the radiation. I study the simplest configuration: the comparison of the output current measured with the two detectors without the aluminium covers. This configuration concerns the measurements done with the sensor DC01, which is the only diamond sensor for which the cover can be removed. The output currents from the I-d measurements are employed in the study. From the stability analysis in Sect. 5.4, the sensor DC01 is expected to show a better response when a negative bias is applied, close to that of an ideal crystal. Therefore, the analysis of the currents measured in that configuration are more reliable. However, measurements with the positive polarisation are also analysed, to gain a complete picture.

The measured output current from a detector at a given distance d of the source with respect the detector can be expressed as

$$I_{\mathrm{det}}^{\mathrm{mis}}(d) = \mathcal{A}\,\frac{E_{\mathrm{pd}}^{\mathrm{det}}(d)}{\epsilon_{\mathrm{det}}}\,\mathcal{E}_{\mathrm{det}}\,e\,, \tag{5.9}$$

where $\mathcal{A}$ is the source activity, *i.e.* the number of β decay per second; $E_{\mathrm{pd}}^{\mathrm{det}}$ is the REPD for the given distance of the source; ϵ_{det} is the energy to create a $e^{-}h^{+}$ pair; e is the elementary charge; and $\mathcal{E}_{\mathrm{det}}$ is an efficiency factor. Such a factor depends on the detector considered and the operational conditions, as it could vary according to the generated charge in the detector volume and also according to the bias voltage applied to the detector, which change the charge-carriers mobility and the charge-collection efficiencies. For the currents generated by the β radiation, and the bias voltage applied, the silicon diode can be considered fully efficient, and so $\mathcal{E}_{\mathrm{Si}}$ can be set to 1.

For a diamond sensor, this factor comprises different contributions: a charge collection efficiency, and a photoconductive gain $\mathcal{G}$ (as explained in Sect. 3.3). For bias voltages greater than 50 V, the charge collection efficiency can be assumed 1. Then, $\mathcal{E}_{\mathrm{Di}} = \mathcal{G}$.

This gain can widely changes from sensor to sensor as it ultimately related to the crystal features, such as trapping from impurities. In Ref. [39] values ranging from 1 up to 5 are reported. In addition, different gain can be observed on the same crystal when different polarisation biases are applied. For a sensor like the DC01, we indeed expect a variation of the gain for opposite polarisation biases, as highlighted from the stability measurement (see Fig. 5.3).

By comparing the output current measured with the diamond sensor and that with the silicon diode at the same source conditions, *i.e.* at the same source distance d, the dependence on the source activity cancels out,

$$\left.\frac{I^{\rm mis}_{\rm Di}}{I^{\rm mis}_{\rm Si}}\right|_d = \left.\frac{E^{\rm Di}_{\rm pd}}{E^{\rm Si}_{\rm pd}}\right|_d \frac{\epsilon_{\rm Si}}{\epsilon_{\rm Di}}\,\mathcal{G}\,. \tag{5.10}$$

The edge of this ratio is two folds: it allows to be independent on the source activity; it suppresses systematic uncertainty that are common to numerator and denominator, either in the measurements of the output currents (*e.g.* the dependence on the source-detector distance) or in the estimate of the REPD with simulation. Thus, Eq. 6.6 provides a way to infer information on the diamond-sensor gain. This can be expressed as

$$\mathcal{G} = \mathcal{F}(d)\,K\,, \tag{5.11}$$

where

$$\mathcal{F}(d) = \left.\frac{I^{\rm mis}_{\rm Di}}{I^{\rm mis}_{\rm Si}}\right|_d \left.\frac{E^{\rm Si}_{\rm pd}}{E^{\rm Di}_{\rm pd}}\right|_d \quad \text{and} \tag{5.12}$$

$$K = \frac{\epsilon_{\rm Di}}{\epsilon_{\rm Si}}\,. \tag{5.13}$$

With this writing, I decoupled the factor $\mathcal{F}(d)$, function of the source distance, from the factor K, which is a corrective constant.

First, I check any dependence of the gain on the source distance, *i.e.* varying the flux of β particles on the detector. The values of $\mathcal{F}$ as a function of d are reported in Figure 5.9 (top row). The results obtained with a negative bias polarisation are shown on the left side, while those with a positive bias polarisation on the right side. The two plots show an opposite trend of the values of $\mathcal{F}$ as a function of the source distance. The negative polarity presents a variation of the values of $\mathcal{F}$ of about 10% as a function of the source distance. However, the variation is generally smaller than 10%, and for the positive polarisation the values of $\mathcal{F}$ are roughly constant up to the measurements performed with a distance of 14 mm. The largest variation (19%) is present in this case for the set of measurements at distances higher than 14 mm. Given possible instability of the output current observed with the positive bias, and the smaller values of the current at largest distances, we cannot exclude a systematic bias causing the trend. In the following, we consider no dependence of $\mathcal{F}$ with the source distance.

The bottom row of Fig. 5.9 presents the values of $\mathcal{F}$ as a function of the expected current of the diamond sensor, which, assuming a unity gain, can be estimated as

$$I^{\rm Di}_{\rm exp} = \mathcal{A}_{\rm mis}\frac{E^{\rm Di}_{\rm pp}}{\epsilon^{\rm Di}_{eh}}\,, \tag{5.14}$$

where

$$\mathcal{A}_{\rm mis} = \frac{I^{\rm Si}_{\rm mis}}{e}\frac{\epsilon^{\rm Si}_{eh}}{E^{\rm Si}_{\rm pp}}\,. \tag{5.15}$$

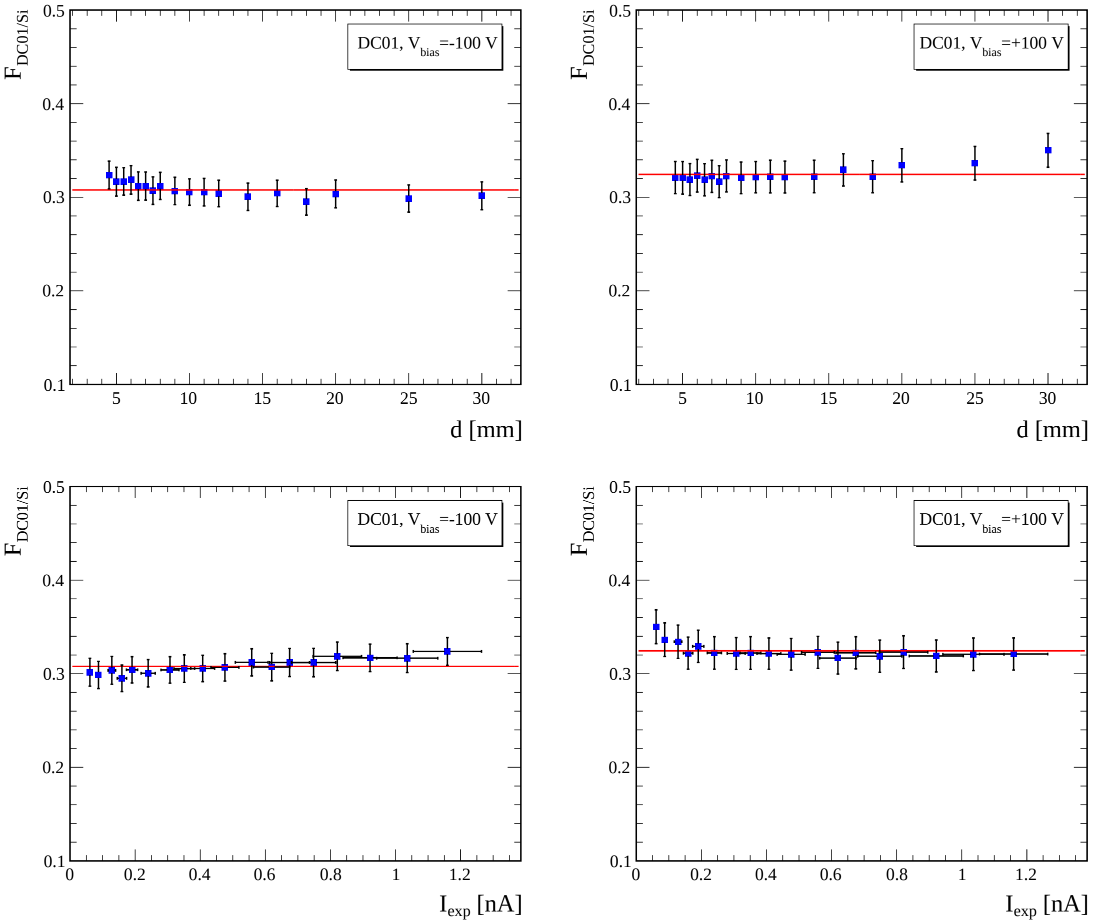

Figure 5.9: Sensor DC01, $\mathcal{F}$ as a function of: (top row) source distance d; (bottom row) expected current. Plots on the left are obtained with negative bias, those in the right for the positive bias.

is the measured activity, estimated from the silicon-diode current. The results with a negative polarisation show an increase of about 10% of the value of $\mathcal{F}$ in the interval of the expected currents considered, while the measurement with the positive bias presents stable values of $\mathcal{F}$ for expected currents higher than 200 pA. These trends follows those already highlighted for the dependence on d.

I consider the factor $\mathcal{F}$ approximately constant in the range of currents probed and I average all values of $\mathcal{F}(d)$ obtained for each polarisation bias. The resulting values are

$$\mathcal{G}^- = 1.11 \pm 0.08$$
$$\mathcal{G}^+ = 1.17 \pm 0.08$$

for the negative and positive polarisation, respectively. To obtain these values, I used $\epsilon^{\mathrm{Di}}_{e/h} = 13.1 \pm 0.1\,\mathrm{eV}$, as measured with the radiation α in Chapter 4.[3] For the silicon diode, I used $\epsilon^{\mathrm{Si}}_{e/h} = 3.6\,\mathrm{eV}$, according to the precise known value, and no uncertainty is associated.

---

[3] The uncertainty on $\epsilon^{\mathrm{Di}}_{e/h}$ has been inflated by a factor 2 to account for possible systematic effect that are neglected in the measurement of $\epsilon^{\mathrm{Di}}_{e/h}$.

The gains obtained with the opposite polarisation biases are found to be compatible between each other. They agree with 1, and are smaller than those observed in Ref. [39] for different diamond sensors irradiated with the very same source used here. Compared to that work, I used a novel method, based on the use of the silicon diode as a reference, to obtain the estimate of the gain. This same method is used in the next Chapter, where the photoconductive gain is estimated from the irradiation with X rays.

Chapter 6

Characterisation with X radiation

This Chapter describes the characterisation of the diamonds sensors using a X-ray source. This is the first time that this source is used in this respect. The study follows the pattern of the characterisation with the β radiation to make a comparison of the results. I measure the stability of the output current generated by a constant flux of X-rays. I study the dependence of the output current on the intensity of the X radiation and its energy, and I compare the current with that from a silicon diode, used as a reference, to characterise the response.

6.1 Motivation for a study with X rays

The reason to study the response of diamond sensors to the X radiation stems from an anomaly of the Belle II radiation monitor observed during operations. This anomaly consists in the blindness of the monitor system to occasional high occupancy signals observed in some regions of the first layer of PXD detector and associated to $\mathcal{O}(10\,\mathrm{keV})$ synchrotron radiation from the accelerator. It is therefore necessary to understand the reasons of this blindness to develop possible countermeasures to protect the inner detectors from potential damages related to the synchrotron radiation. The monitor blindness can be explained by different hypotheses: (i) diamond sensors are more transparent than silicon sensors to $\mathcal{O}(10\,\mathrm{keV})$ photons; or/and (ii) most of the synchrotron photons are stopped in the aluminium packaging of the diamonds sensors; or/and (iii) the location of the diamonds sensors does not allow for an efficient detection of the synchrotron radiation.

In what follows, I present an analysis of the response of diamond sensors irradiated with a X-ray source that mimics the synchrotron radiation, to give information about points (i) and (ii). Taking from this motivation, this analysis allows to characterise the diamond sensors using a source that was never employed before for the calibration of the monitor's sensors. The same method presented in Chapter 5.7, where the silicon diode is used as a reference, is employed. The results of the two characterisation, with the X rays and the β radiation, can be compared to build confidence on the method. In particular, it is interesting to check the compatibility of the results obtained from the irradiation with the two sources for the measurement of the stability of the output current, and for the measurement of the photoconductive gain of the sensors.

First, a few words on the potential damage of the synchrotron radation to the silicon detectors to understand why a protection mechanism triggered by the monitor system is important. Since the maximum energy transfer from $\mathcal{O}(10\,\mathrm{keV})$ photons is far below the threshold energy for a bulk damage, no damage of this kind is expected in the silicon detectors. However, interacting with the insulating layer of the silicon detector (silicon

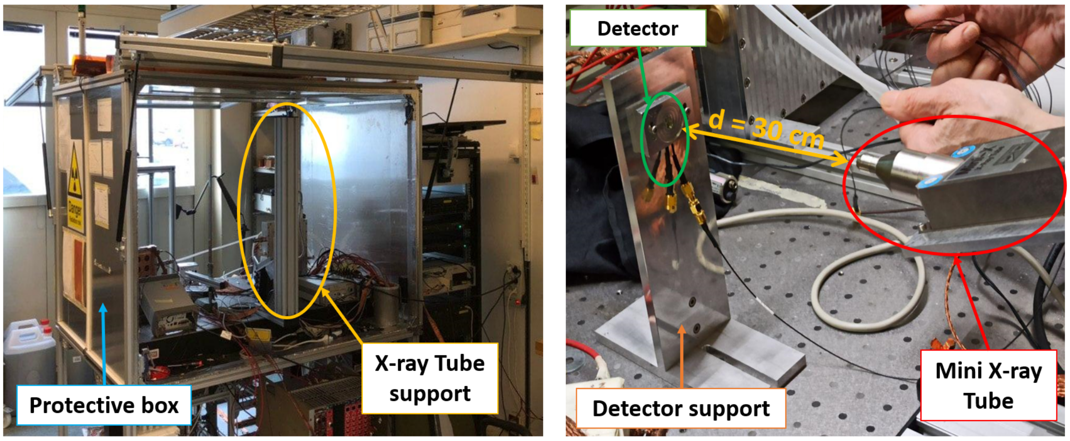

Figure 6.1: Pictures of the apparatus: (left) the protective box and the X-ray source support; (right) the X-ray source and the detector placement.

oxide, SiO_2), X rays generate electron-hole pairs, some of which remain in the insulating layer without recombining. Once holes come close to the Si-SiO_2 interface, a fraction of them are trapped in the oxide close to the interface, generating fixed oxide charges. In addition, border and interface traps originate. These fixed oxide charges and interface traps change the performance of the silicon sensors. The main effects are: a shift in the full depletion voltage to larger values; an increase of the leakage current and the inter-pixel capacitance; a decrease of the inter-pixel resistance; and an electron accumulation layer which may cause charge losses at the interface.

6.2 Experimental setup

All four diamonds DC00, DC01, DC15, and DC25, and the silicon diode are used in the characterisation. The experimental setup is composed of:

- a radiation source provided by the “Amptek Mini X-2”, a very compact X-ray tube [54];
- a power supply [45] used to apply a bias voltage to the sensors;
- the 4-channels picoamperometer used also in the characterisation with the β radiation and presented in Sect. 5.2.

The apparatus is shown in Fig. 6.1. The X-ray tube and the sensor support are placed inside a protective box made of aluminium and lead layers. The source and the sensor are located on the same horizontal plane at a relative distance of 30 cm to obtain a uniform irradiation of the detector. This distance is chosen to reproduce the same conditions at which the energy spectra of the X-ray radiation were measured by the producer.

6.2.1 The X-ray source

The X-ray tube emits photons in an energy range from a few keV to 50 keV, by exploiting bremsstrahlung radiation emitted by electrons interacting with a 1.0-μm-thick gold target. These electrons are emitted from a tungsten filament by thermionic effect generated with a

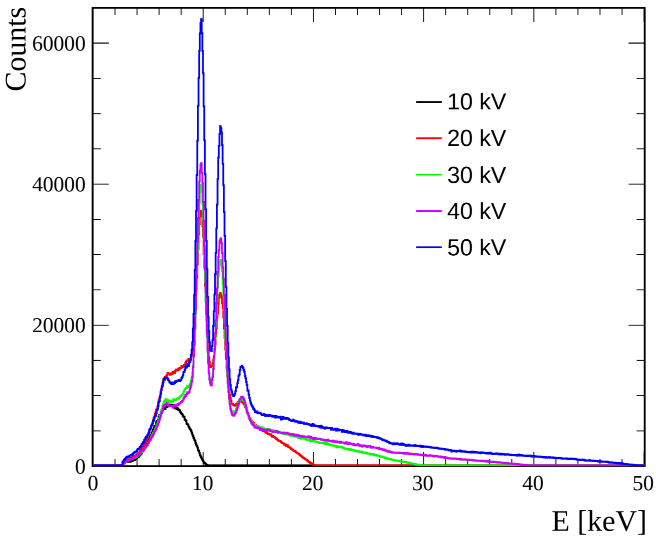

Figure 6.2: Efficiency-corrected energy spectra of the X-ray after 30 cm of air for the five voltages V_{set} used.

current (I_{set}), and they are accelerated by a voltage difference (V_{set}) between the filament and the gold target. Interacting with the target, electrons decelerate by the emission of bremsstrahlung X rays in the direction of a berilium window. The emitted photons have an output spectrum which is the superposition of a continuous component due to the bremsstrahlung radiation and some peaks corresponding to the energy levels of gold atomic shells. The parameters V_{set} and I_{set} can be set via software to vary the energy spectrum and the flux of the radiation. Since the voltage V_{set} determines the energy of the electrons interacting with the gold target, different voltages correspond to different energy spectra. Instead, varying the current I_{set} changes the number of electrons emitted by thermionic effect, hence the resulting photons flux. At the same value of I_{set}, the photon flux is not constant for different value of V_{set}. Unfortunately, the producers does not provide a measurement of the photon flux at some given values of $(I_{\text{set}}, V_{\text{set}})$. The angular spread is provided: the flux is almost constant in a cone of ±30 degrees centred on the symmetry axis of the tube.

Five energy spectra are provided, one for each voltage $V_{\text{set}} = \{10, 20, 30, 40, 50\}$ kV that can be set at the source. These spectra have been measured by the producer using a 1-mm-thick CdTe detector, placed in air at 30 cm from the X-ray source. I obtain the energy spectra of the X-ray source using the data and the detector efficiency as provided by the producer. The efficiency-corrected spectra for the five different voltages V_{set} are shown in Fig. 6.2. These spectra are used in the analysis of the measurements as described later in Sect. 6.7.

6.3 Measurement methods

The characterisation of the diamond sensors consists in two different set of measurements, dubbed *stability* and *linearity* measurements. The stability measurements have the same goal of those performed with the β radiation reported in Sect. 5.3.

The linearity measurements target to check the expected linear relation between the output current and the current I_{set} of the X-ray tube, which is proportional to the intensity of the radiation. The slope parameters determined from these measurements are employed for the characterisation of the diamond sensors using the silicon diode as a reference, as explained in Sect. 6.7.

All measurements are done using two polarisation biases, +100 V and −100 V, with the same configuration used in the other characterisations (the bias applied to the back side; the other side set to ground). The measurements with opposite biases are done to test a symmetric response of the sensors. The silicon diode is used only in the linearity measurements with a 100 V bias applied. For all measurements, the output current is measured with the picoamperometer using a sampling time of 1 s.

The procedure for the two sets of measurements are briefly outlined as follows:

Stability The sensor to be studied is placed inside the protective box on the support and the bias voltage is applied. The hermetic box guarantees minimum light conditions such that the only source of radiation is given by the X-ray tube.[1] Before switching on the X-ray tube, a measurement of the dark current is performed by sampling the output current for a period of time between 10 and 20 minutes. The X-ray tube is switched on, setting constant values of $I_{\text{set}} = 50\,\mu\text{A}$ and $V_{\text{set}} = 50\,\text{kV}$, while the sampling of the output current continues. The output current is measured for at least 2 hours or more in this fixed conditions.

Linearity After applying the bias voltage, a measurement of dark current is done sampling the output current from the sensor for a time period between 3 and 5 minutes. Then, the X-ray tube is switched on. Setting the voltage V_{set} to a fixed value, the output current is measured for 2 minutes for different values of I_{set}. The X-ray tube is switched off, and a second measurement of the dark current is performed. This procedure is iterated for different values of V_{set}, for all the detectors. For the diamond sensors DC01 and the silicon diode, the measurements are done both with and without the aluminium cover. As a reminder, the aluminium cover is permanently glued to the detector package for all the other diamond sensors.

6.4 Analysis of the stability measurements

The values of the measured output current, I_{diam}, are plotted as a function of the irradiation time, t, and they are shown in Figs. 6.3 and 6.4 for all diamond sensors.[2]

In all plots, an initial value of the output current distributed around zero, corresponding to the dark current measurements, is visible; after a certain time (between 500 and 1000 s, changing for each measurement), the output currents suddenly have nonzero values, and this corresponds to the turning on of the X-ray source. The results are very similar to those observed for the stability measurements done with the β radiation for all sensors. Also in this case, the sensor DC01 reaches a stable value of the output current with the negative bias (Fig. 6.3, top-right), while with a positive bias it delivers an unstable current (Fig. 6.3, top-left). This test confirms the preferred configuration with negative biases for

---

[1] Shielding from visible light is actually relevant only for the silicon diode. In this case, all light sources in the lab must be turn off and blinds on the windows must be used.

[2] In these plots, the uncertainty associated to each value of the output current is measured from the distribution of the values of I_{diam} in the stabilisation range, where present, or in a range of roughly constant values of I_{diam}. The standard deviation of this distribution is preferred to the uncertainty associated by the picoamperometer because the fluctuations of the output current are dominated by electronic noise associated to the acquisition setup.

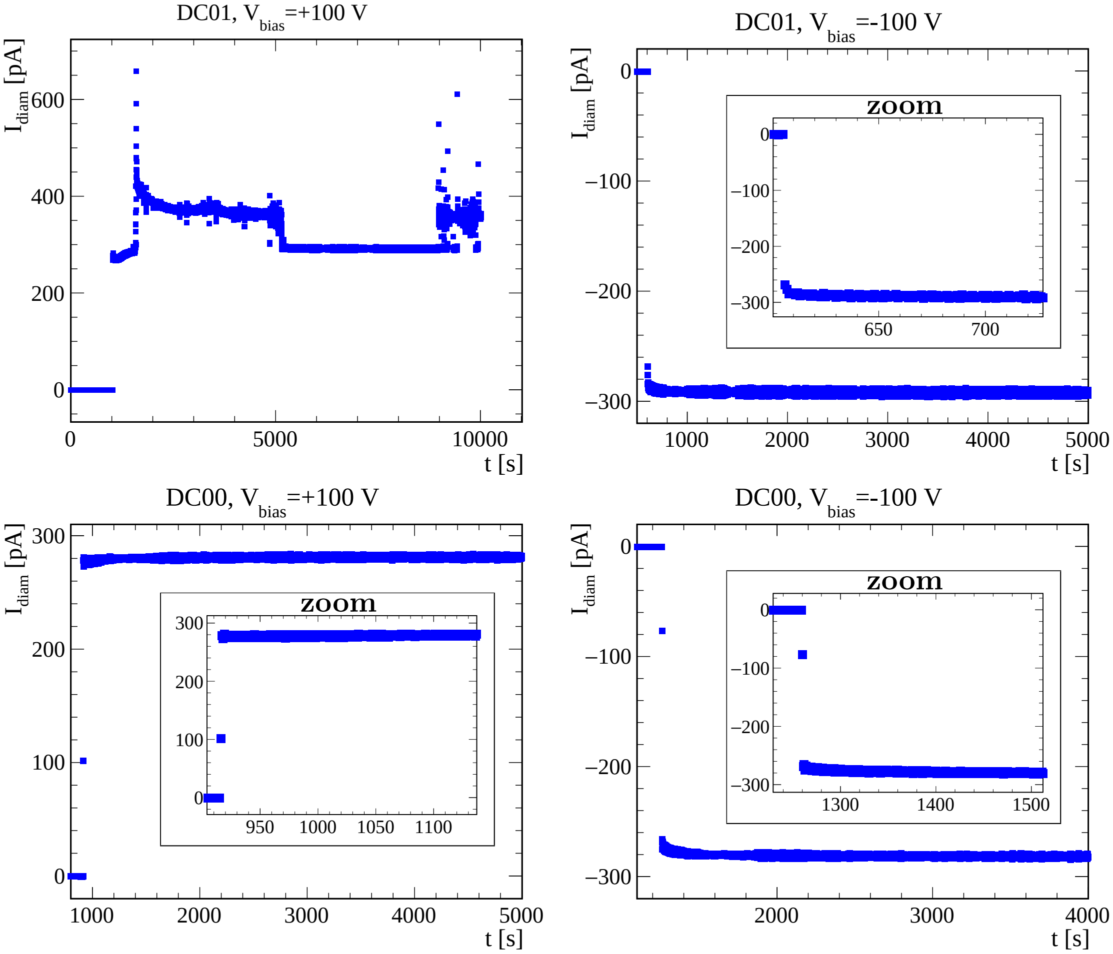

Figure 6.3: Output current I_{diam} as a function of the irradiation time t for (first row) the sensor DC01 and (second row) DC00, with the X-ray source set parameters $V_{\text{set}} = 50\,\text{kV}$ and $I_{\text{set}} = 50\,\mu\text{A}$. On the left plots, a bias $V_{\text{bias}} = +100\,\text{V}$ is applied; on the right plots, the bias is $V_{\text{bias}} = -100\,\text{V}$. The box plots show a zoom of the transient region of the output current.

this sensor. The of the sensor DC00 shown in the second row of Fig. 6.3 present a response close to that of an ideal crystal also in this case for both polarisation biases.

Fig. 6.4, first row, reports the case of the sensor DC15 where the long transient time to reach stable currents are observed like for those presented in Sect. 5.4. This sensor presents more than one transient times, for both bias polarisations, for different time intervals. These might be due to the presence of traps at different depths inside the diamond bulk [34]. Fits of the data are done in different region of time using Eq. 5.3. The transient time take values of the order of $10^3\,\text{s}$ for the long-time constant, and of order $10\,\text{s}$ for the short-time constant.

Finally, on the second row of Fig. 6.4, the measurements shows that the sensor DC25 does not present a good stability of the output current for both bias polarisations. For this reason, the sensor DC25 is discarded in the rest of the analysis.

The results are summarised for each sensor:

DC00 very stable output current and sharp transient time on both bias polarisation; very

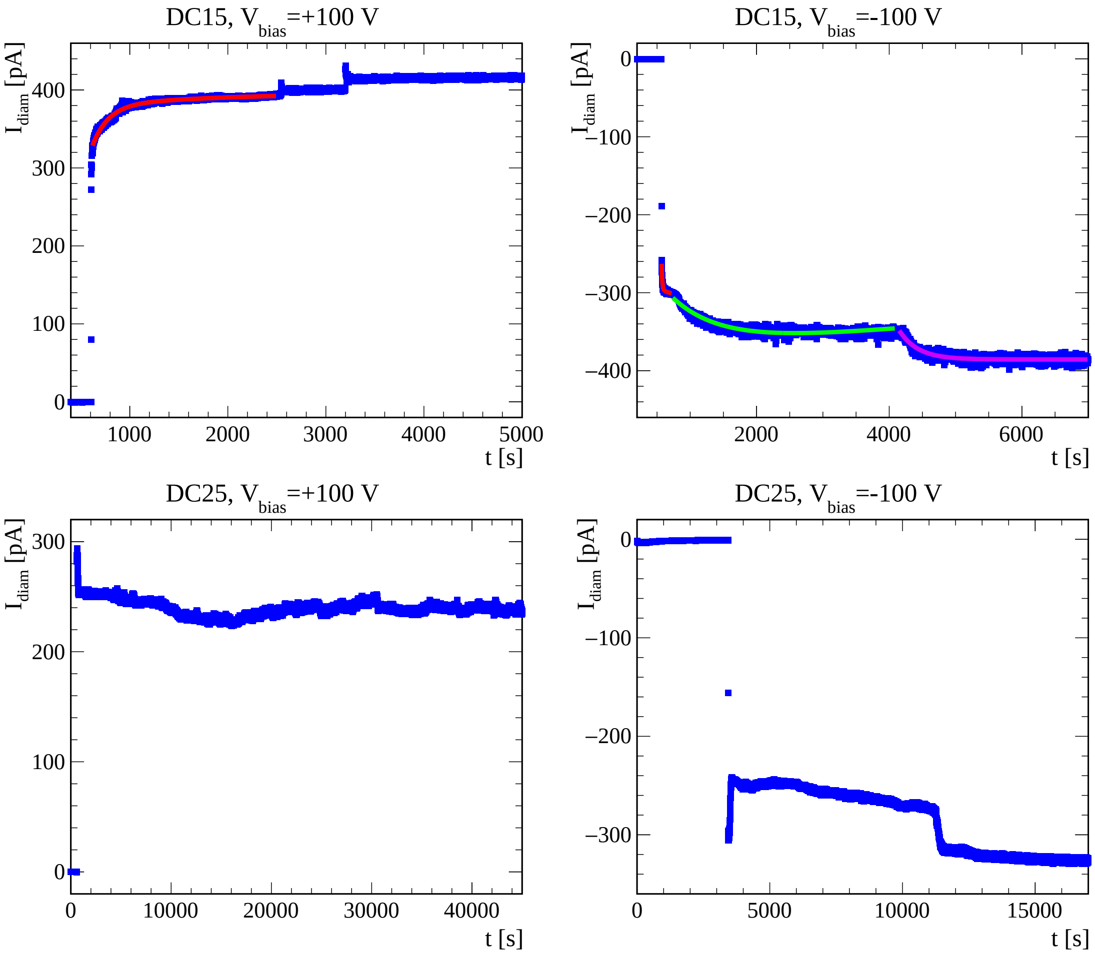

Figure 6.4: Output current I_{diam} as a function of the irradiation time t for (first row) the sensor DC15 and (second row) DC25, with the X-ray source set parameters $V_{\text{set}} = 50\,\text{kV}$ and $I_{\text{set}} = 50\,\mu\text{A}$. On the left plots, a bias $V_{\text{bias}} = +100\,\text{V}$ is applied; on the right plots, the bias is $V_{\text{bias}} = -100\,\text{V}$. The current profile of the sensor DC15 are fit using Eq. 5.3.

symmetric response; close to an ideal crystal;

DC01 negative bias preferred: sharp transient time and stable output current with this polarisation; unstable output current with a positive bias;

DC15 long transient time and different *plateau* of stable output current; similar trend for both polarisation;

DC25 very unstable output currents with both bias polarisation; discarded for future analysis.

6.5 Analysis of the linearity measurements

In the linearity measurements, the output current is measured for about 2 minutes, yielding about 100 values for a given current I_{set} at the source. For each sample, the mean output current, I_{mean}, and the associated uncertainty, the error on the mean $\sigma_{I_{\text{mean}}}$, are calculated. With the same method, the mean dark current and its uncertainty, $I_{\text{dark}} \pm \sigma_{I_{\text{dark}}}$, are calculated from the currents measured without any radiation. This offset, which is generally around 2 pA, is subtracted to each value to obtain the current I^*_{mis}. For each energy spectrum, *i.e.* for a fixed voltage V_{set} on the X-ray tube, the measured current I^*_{mis} are plotted as a function of I_{set}. A fluctuation of $0.1\,\mu$A of the value of I_{set} has been observed during the measurements. This fluctuation is assigned as an uncertainty to I_{set}.

A fit with a linear function is done to verify the dependence of I^*_{mis} on I_{set} and to determine the slope and intercept parameters. The top row of Fig. 6.5 shows the measurements and the fit for the diamond sensor DC01 and for the silicon diode, both without aluminium cover. The results show the expected linear response for both detectors. The current measured with the silicon diode is about five times higher than that measured with the diamond sensor, because, for the same energy spectrum of the incident photons, the attenuation length is higher for silicon than diamond.

Overall, the sensors present good linear relations for each energy spectrum of the source and polarisation bias. All fit results are reported in Appendix A. The output currents measured in same conditions present similar values for the different diamond sensors. An attenuation of a factor between 2 and 7 of the output current is observed in the diamond sensors with the aluminium cover applied. The intercepts parameters of the fits are of the order of a few pA, compatible with zero within uncertainty for most of the cases. It is interesting to note the very symmetric response of the diamond sensor DC00 when changing the polarisation of the bias applied. The plots are shown in the middle row of Fig. 6.5, bottom row. This is in agreement with the results from the stability measurements observed in Fig. 6.3 (bottom row).

The linear fit present a poor quality for the measurements collected with the sensors DC15 and DC01 at $V_{\text{set}} = 10\,\text{kV}$, as shown in Fig 6.5. By inspecting the distribution of the output currents for each value of I_{set}, an unstable profile as a function of the acquisition time is observed. The instability of the output current could be explained by a phenomenon of hysteresis, as highlighted also in the stability measurement shown in the top row of Fig. 6.4. In addition, the intercept of the two fits are not compatible with zero, and the values are comparable with the current measured at low I_{set}, although the dark-current offset is subtracted. Such trends are present only at $V_{\text{set}} = 10\,\text{kV}$ and they might be related to low and unstable flux from the source for $V_{\text{set}} = 10\,\text{kV}$. Since the response on the diamond is unstable at this source voltage, all measurements at $V_{\text{set}} = 10\,\text{kV}$ are not considered for the rest of the analysis.

6.6 Released energy per photon

In this Section, I estimate the energy released by the X rays in the diamond sensor and in the silicon diode considering the different energy spectra set by the voltage V_{set} at the source. This energy is calculated per single photon, hence it is called “released energy per photon” (REPP), such that the total energy absorbed by the sensor is the REPP multiplied by the total number of incident photons. This number is not know, since there is no measurement of the flux from the X-tube. However, by using the silicon diode as a reference, only an estimate of the REPP is needed. This is explained in Sect. 6.7, where the REPP, combined with the slope parameters measured in the linearity measurements, is used to study the response of the diamond sensors in a similar manner of what is done in Sect. 5.6 for the β radiation.

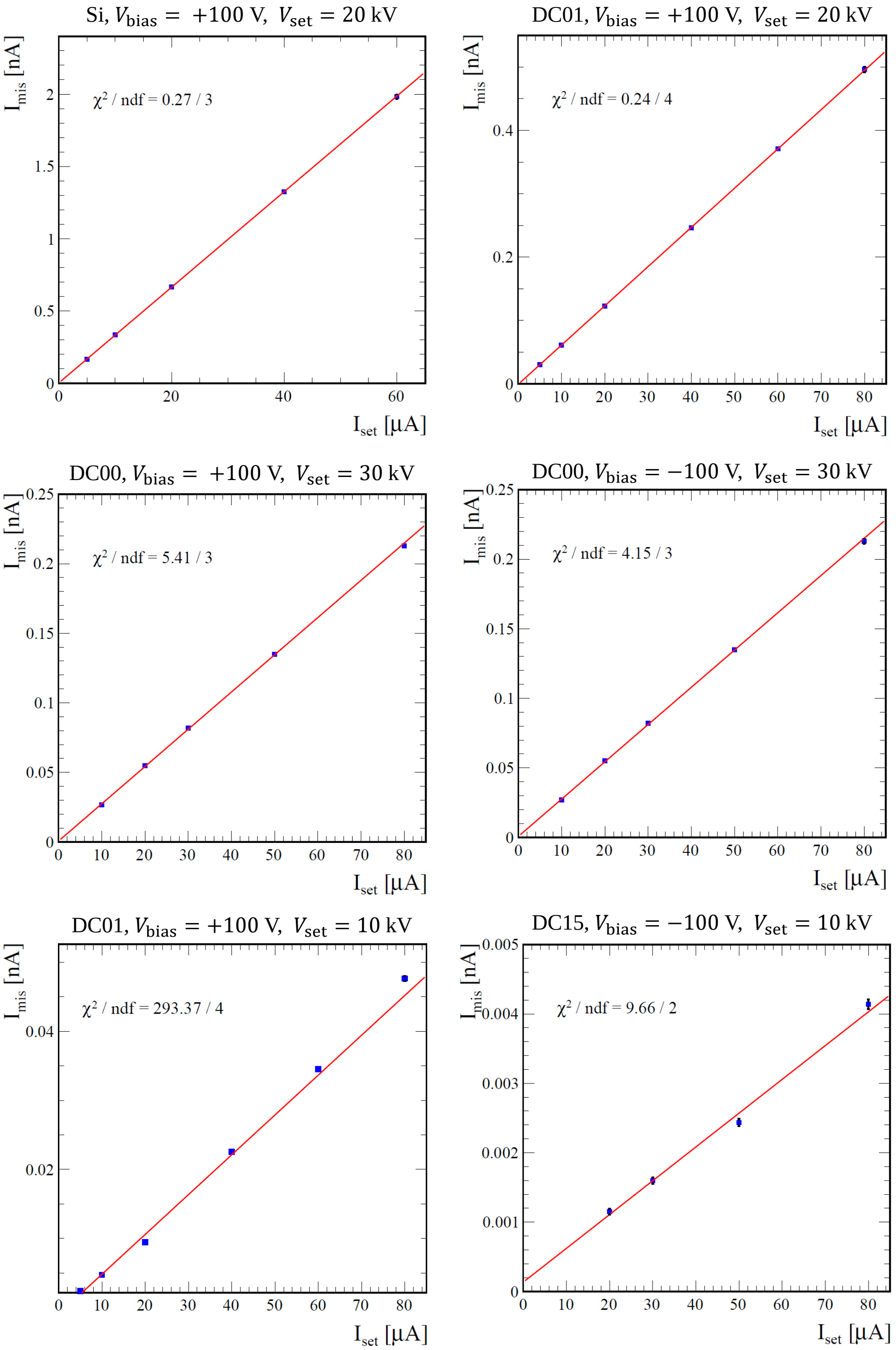

Figure 6.5: Example of linearity plots. On the top row: the silicon diode (left) and the diamond DC01 (right) with a bias voltage of +100 V, measured with a source voltage V_{set} = 20 kV. Both sensor are without aluminium cover. Middle row: the diamond DC00 with a bias voltage of (left) +100 V and (right) −100 V, measured with a source voltage V_{set} = 30 kV. Bottom row: example of the bad-quality fit of the measurements at V_{set} = 10 kV, for the diamond sensors DC01 without cover (left) and DC15 (right) with a bias voltage of +100 V.

6.6.1 Spectrum of the released energy

The estimate of the REPP exploits a simulation of the experimental setup. The simulation is done with Fluka [51].

All four configurations used in the measurements are considered for the detectors: silicon diode, diamond sensor; the same detectors with the aluminium cover applied. These four configurations are named: “Si” for silicon diode; “Di” for the diamond sensor; “Si+Al” for the silicon diode with the aluminium cover; “Di+Al” for the diamond sensor with the cover. The silicon diode and the diamond sensor are configured as explained in Sect. 3.4. For both detectors, the configuration with the aluminium cover is defined by adding a 190-μm-thick aluminium layer at a distance of 0.2 mm from the sensor surface.

The source is simulated as a square of $(0.4 \times 0.4)\,\mathrm{mm}^2$, located at 0.4 mm from the sensor surface in vacuum. This definition guarantees that all generated photons impact on the surface of the sensor. The distance between the source and the sensor in vacuum is fake: the photon-energy spectrum used in input for the source is that shown in Fig. 6.2, which already account for the passage of the photons through 30 cm of air. For each generated photon from the source, the simulation return the energy released inside the detector volume, taking into account all cross sections for the interaction with the different materials along the path (mainly photoelectric effect and a small fraction of Compton scattering).

A weighting method is used to account for the different energy spectra produced by the voltages V_{set} at the source. The range 0–50 keV is split in intervals of equal width (bins), each corresponding to a bin of the histograms of the spectrum in Fig. 6.6. For each bin, 5×10^4 photons are generated with a flat energy distribution in the interval, and the results of the interaction of these photons are saved independently for each detector configuration. The released energies from all photons in a bin are weighted with a scaling factor to obtain the distribution of the released energy for a given source-energy spectrum. This scaling factor is the content of the bin of the histogram of the source-energy spectrum. The source-energy histogram is normalised such that the sum of all bin contents is one. The resulting distribution of the weighted released energies is normalised to represent the distribution of the REPP, by dividing the integral with the total number of generated photons.

Figure 6.6 reports the distribution of the REPP obtained for all detector configurations with the different energy spectra of the source. Without the aluminium cover, photons of the same energy have a lower probability to interact with diamond than silicon. Moreover, the REPP spectrum for the diamond sensor has an higher number of events with energy lower than 1 keV. This is explained by an higher contribution of the Compton scattering in this case, for which photons loose part of their initial energy. With the aluminium cover, the REPP spectra show no events between 1 and 6 keV, since low energy photons have a high probability to interact in the aluminium and are stopped by this shielding.

To check the simulation results, I compare the interaction probability determined from the simulated data and that calculated analytically from known attenuation lengths of X-ray photons. These probabilities are calculated as a function of the photon energy as follows. For the simulated data, the interaction probability is calculated in each energy interval as the number of photons that released energy in the detector divided by the total number of generated photons. The interaction probability as a function of the photon energy E is analytically calculated as the product of the probability of interaction, $P_{\mathrm{int}}(E)$, inside the active volume of the sensor and the probability of no-interaction, $1 - P_{\mathrm{int}}(E)$, in the materials in front of the active volume (electrodes for the diamond sensor; aluminium for the detectors with the cover). The probability of interaction in a material of thickness

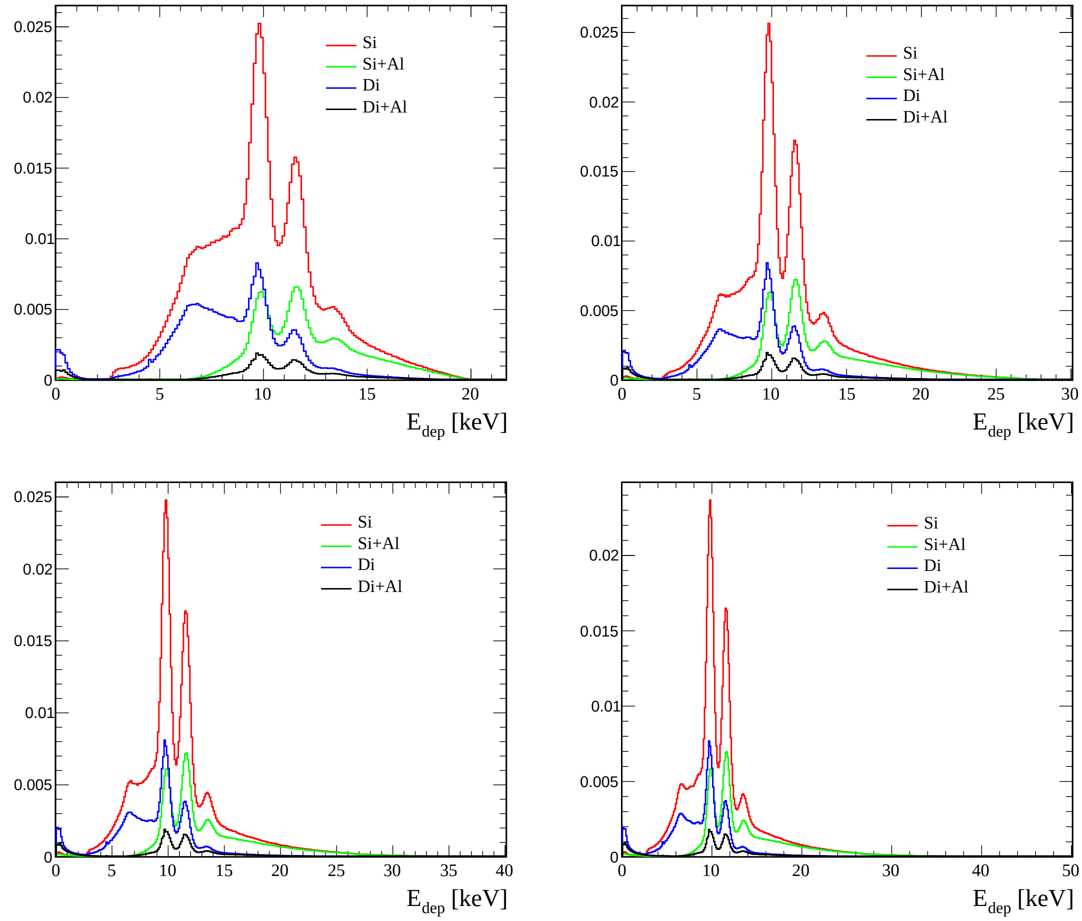

Figure 6.6: Distributions of REPP obtained with simulation for the four detector configurations (Si, Si+Al, Di, Di+Al), for a source voltage V_{set} of (top-left) 20 kV, (top-right) 30 kV, (bottom-left) 40 kV, (bottom-right) 50 kV.

x_{mat} for a photon with energy E is

$$P_{\mathrm{int}}(E) = 1 - e^{\frac{x_{\mathrm{mat}}}{\lambda_{\mathrm{mat}}(E)}} \tag{6.1}$$

where $\lambda_{\mathrm{mat}}(E)$ is the attenuation length of the material provided by data from the Centre for X-Ray Optics of the Lawrence Berkeley National Laboratory (LBNL) [55]. Figure 6.7 shows the probability of interactions for the four detector configurations as a function of the photon energy. The agreement is satisfactory, as the small differences are due to the approximation of the analytic calculation.

6.6.2 Estimate of the REPP

The REPP for a given detector configuration, $E_{\mathrm{pp}}^{\mathrm{det}}$, is calculated by integrating the energies of the corresponding distribution $(\mathrm{d}n/\mathrm{d}E)|_{\mathrm{det}}$ shown in Fig. 6.6,

$$E_{\mathrm{pp}}^{\mathrm{det}} = \int_{E_{\mathrm{min}}}^{E_{\mathrm{max}}} E \left.\frac{\mathrm{d}n}{\mathrm{d}E}\right|_{\mathrm{det}} \mathrm{d}E \,. \tag{6.2}$$

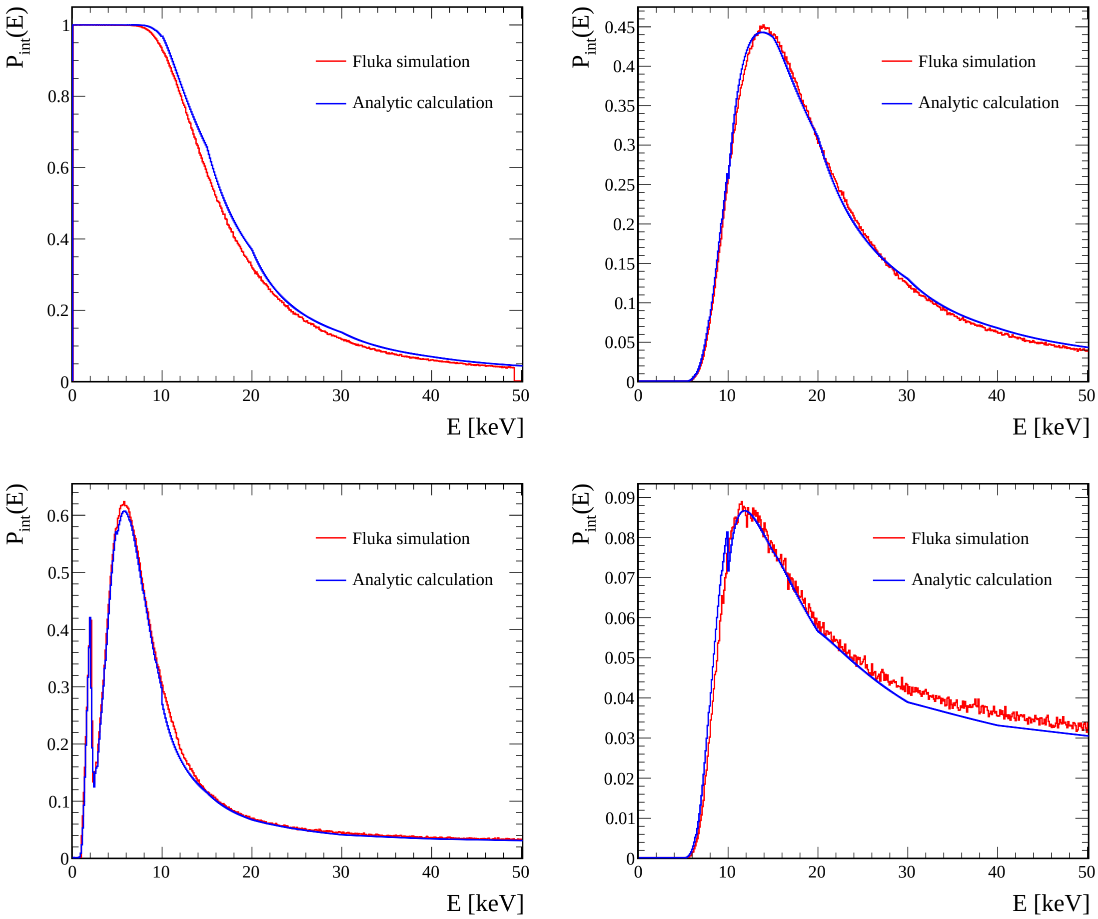

Figure 6.7: Interaction probability as a function of the photon energy for the four detector configurations. The two rows represents the probability of interaction in the silicon diode (top) and the diamond sensor (bottom), for both the configuration without (left) and with (right) the aluminium cover.

The dominant uncertainty in the calculation of $E_{\text{pp}}^{\text{det}}$ is assumed to be caused by the uncertainty on the thickness of the layers of silicon, diamond and aluminium in the detector configurations. Any uncertainty due to the electrodes thickness is negligible since these layers are thinner than the sensor volume, and the photons have a very low interaction probability there.

In the configuration without aluminium cover, the uncertainty associated to $E_{\text{pp}}^{\text{det}}$ has been calculated as the maximum difference between $E_{\text{pp}}^{\text{det}}$ for a thickness x and that for $x \pm \Delta x$, where Δx is the x uncertainty:

$$\Delta E_{\text{pp}}^{\text{det}} = \max\left\{ \left| E_{\text{pp}}^{\text{det}}(x) - E_{\text{pp}}^{\text{det}}(x+\Delta x) \right| \; ; \; \left| E_{\text{pp}}^{\text{det}}(x) - E_{\text{pp}}^{\text{det}}(x-\Delta x) \right| \right\} . \tag{6.3}$$

In the configuration with the aluminium cover, it is necessary to consider also the contribution related to the uncertainty on the aluminium thickness. Since a higher variation of $E_{\text{pp}}^{\text{det}}$ is expected either for an higher sensor thickness and a lower cover thickness, and *vice*

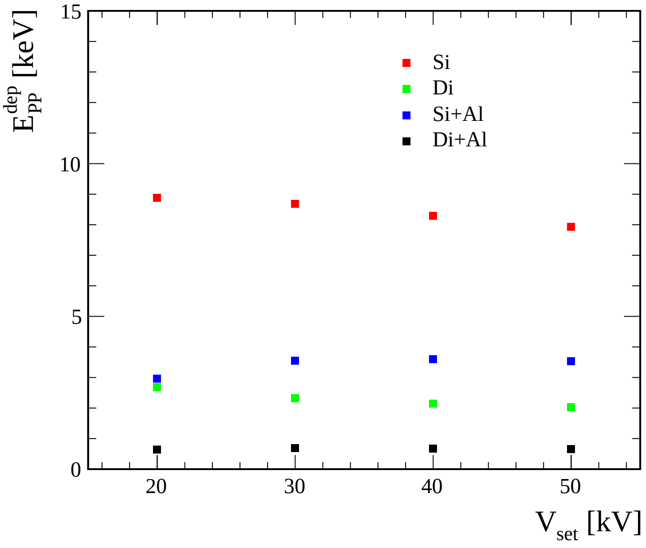

Figure 6.8: Estimated values of REPP for the four different detector configurations as a function of the source voltage V_{set}.

versa, the uncertainty is calculated as

$$\begin{aligned}\Delta E_{\mathrm{pp}}^{\mathrm{det}} = \max \Big\{ & \left|E_{\mathrm{pp}}^{\mathrm{det}}(x_{\mathrm{Si/Di}}, x_{\mathrm{Al}}) - E_{\mathrm{pp}}^{\mathrm{det}}(x_{\mathrm{Si/Di}} + \Delta x_{\mathrm{Si/Di}}, x_{\mathrm{Al}} - \Delta x_{\mathrm{Al}})\right| ; \\ & \left|E_{\mathrm{pp}}^{\mathrm{det}}(x_{\mathrm{Si/Di}}, x_{\mathrm{Al}}) - E_{\mathrm{pp}}^{\mathrm{det}}(x_{\mathrm{Si/Di}} - \Delta x_{\mathrm{Si/Di}}, x_{\mathrm{Al}} + \Delta x_{\mathrm{Al}})\right| \Big\} .\end{aligned} \tag{6.4}$$

Figure 6.8 reports the values of REPP for the four different configurations, as a function of the source voltage V_{set}.

6.7 Comparison of diamond and silicon response

I compare the output current from diamond sensors to that from the silicon diode to infer information on the diamond response, using a similar method as that I employed for the study with the β radiation in Sect. 5.7. I first investigate the simplest configuration: the comparison of the current measured with the two detectors without the aluminium covers. This configuration can be compared directly with the results obtained with the β radiation.This concerns the measurements done with the sensor DC01, which is the only diamond sensor for which the cover can be removed. The study of the detector without the aluminium cover reduces also the uncertainty budget of the model, having a simpler configuration to simulate and analyse. Once the analysis is fully detailed in this configuration, the method is applied to study the detectors with the aluminium cover.

From the stability analysis in Sect. 6.4, the sensor DC01 is expected to show a better response when a negative bias is applied, close to that of an ideal crystal. Therefore, the analysis of the currents measured in that configuration are more reliable. However, measurements with the positive polarisation are also analysed, to compare with the results of Sect. 5.7.

The output current from a detector (det), which can be either the diamond sensor (Di) or the silicon (Si), for a given energy spectrum of the source, can be expressed as

$$I_{\mathrm{det}}^{\mathrm{mis}}(V_{\mathrm{set}}, I_{\mathrm{set}}) = \Phi(V_{\mathrm{set}}, I_{\mathrm{set}})\, A_{\mathrm{det}}^{\mathrm{eff}} \frac{E_{\mathrm{pp}}^{\mathrm{det}}(V_{\mathrm{set}})}{\epsilon_{\mathrm{det}}} \mathcal{E}_{\mathrm{det}}\, e\,, \tag{6.5}$$

where $\Phi(V_{\mathrm{set}}, I_{\mathrm{set}})$ is the photon flux, which is proportional to the X-ray tube current I_{set} and varies also with the energy spectrum through V_{set}; $A_{\mathrm{det}}^{\mathrm{eff}}$ is the detector effective area; $E_{\mathrm{pp}}^{\mathrm{det}}$ is the REPP for the given energy spectrum of the source; ϵ_{det} is the energy to create a e^-h^+ pair; e is the elementary charge; and $\mathcal{E}_{\mathrm{det}}$ is an efficiency factor. As described in Sect. 3.3, the silicon diode can be considered fully efficient, and so $\mathcal{E}_{\mathrm{Si}}$ can be set to 1. For a diamond sensor, this factor is given by the photoconductive gain $\mathcal{G}$, as the bias voltage applied guarantees a full charge-collection efficiency. Then, $\mathcal{E}_{\mathrm{Di}} = \mathcal{G}$.

By comparing the output current measured with the silicon diode and the diamond sensor at the same source conditions, *i.e.* at the same values $(V_{\mathrm{set}}, I_{\mathrm{set}})$, the dependence on the X-ray flux cancels out,

$$\left.\frac{I_{\mathrm{Di}}^{\mathrm{mis}}}{I_{\mathrm{Si}}^{\mathrm{mis}}}\right|_{(V_{\mathrm{set}}, I_{\mathrm{set}})} = \left.\frac{E_{\mathrm{pp}}^{\mathrm{Di}}}{E_{\mathrm{pp}}^{\mathrm{Si}}}\right|_{V_{\mathrm{set}}} \frac{A_{\mathrm{Di}}^{\mathrm{eff}}}{A_{\mathrm{Si}}^{\mathrm{eff}}} \frac{\epsilon_{\mathrm{Si}}}{\epsilon_{\mathrm{Di}}}\, \mathcal{G}\,. \tag{6.6}$$

This last equation provides a way to infer information on the diamond sensor gain, which can be expressed as

$$\mathcal{G} = \mathcal{F}(V_{\mathrm{set}}, I_{\mathrm{set}})\, K\,, \tag{6.7}$$

where

$$\mathcal{F}(V_{\mathrm{set}}, I_{\mathrm{set}}) = \left.\frac{I_{\mathrm{Di}}^{\mathrm{mis}}}{I_{\mathrm{Si}}^{\mathrm{mis}}}\right|_{(V_{\mathrm{set}}, I_{\mathrm{set}})} \left.\frac{E_{\mathrm{pp}}^{\mathrm{Si}}}{E_{\mathrm{pp}}^{\mathrm{Di}}}\right|_{V_{\mathrm{set}}}\,, \text{ and} \tag{6.8}$$

$$K = \frac{\epsilon_{\mathrm{Di}}}{\epsilon_{\mathrm{Si}}} \frac{A_{\mathrm{Si}}^{\mathrm{eff}}}{A_{\mathrm{Di}}^{\mathrm{eff}}}\,, \tag{6.9}$$

and the constant factor K is decoupled from $\mathcal{F}(V_{\mathrm{set}})$, function of the source parameters.

First, I check any dependence of the gain on the source settings. Figure 6.9 reports the values of $\mathcal{F}$, for different source-energy spectra, as a function of the source intensity expressed by the current I_{set} (top row). The results of the negative bias polarisation are shown on the left side, while those with a positive bias polarisation on the right side. In both cases, the values of $\mathcal{F}$ at the same energy-spectrum are roughly constant within a few percent. The largest variation (5%) is present in the positive polarity for the set of measurements at $V_{\mathrm{set}} = 20\,\mathrm{kV}$. Given possible instability of the output current observed with the positive bias, we consider no dependence of $\mathcal{F}$ on I_{set}. The same trend is shown in the middle row of Fig. 6.9, where $\mathcal{F}$ is shown as a function of the expected current of the diamond sensor ($I_{\mathrm{exp}}^{\mathrm{Di}}$), assuming unit gain. The expected current is derived from that measured with the silicon diode as

$$I_{\mathrm{exp}}^{\mathrm{Di}} = \Phi_{\mathrm{mis}} \frac{E_{\mathrm{pp}}^{\mathrm{Di}}}{\epsilon_{eh}^{\mathrm{Di}}} A_{\mathrm{eff}}^{\mathrm{Di}}\,, \tag{6.10}$$

where

$$\Phi_{\mathrm{mis}} = \frac{I_{\mathrm{mis}}^{\mathrm{Si}}}{e} \frac{\epsilon_{eh}^{\mathrm{Si}}}{E_{\mathrm{pp}}^{\mathrm{Si}}} \frac{1}{A_{\mathrm{eff}}^{\mathrm{Si}}}\,. \tag{6.11}$$

is the estimated photon flux.

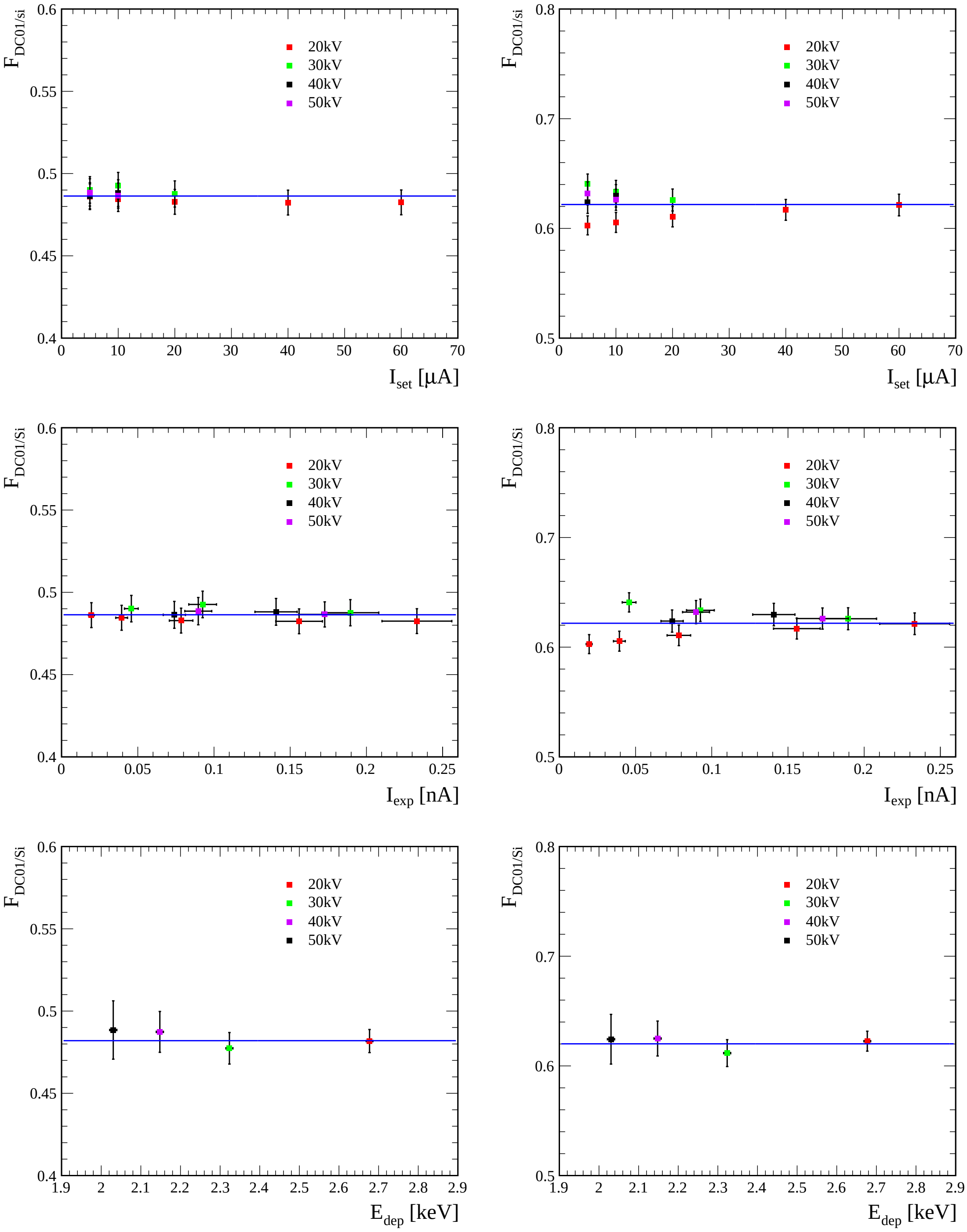

Figure 6.9: Sensor DC01, $\mathcal{F}$ as a function of: (top row) source current I_{set}; (middle row) expected raw diamond current; (bottom row) as a function of the REPP of the diamond sensor. Plots on the left are negative bias, those in the right for the positive bias.

As the factor $\mathcal{F}$ is approximately constant with I_{set}, it can be obtained by the ratio of the slope of the linearity measurement at a fixed source voltage V_{set}

$$\mathcal{F}|_{V_{\text{set}}} = \left.\frac{m_{\text{Di}}}{m_{\text{Si}}}\right|_{V_{\text{set}}} \left.\frac{E_{\text{pp}}^{\text{Si}}}{E_{\text{pp}}^{\text{Di}}}\right|_{V_{\text{set}}} , \tag{6.12}$$

where m_{det} is the slope measured from the linear fits in Sect. 6.5, neglecting the small values (compatible with zero) of the intercept parameters. Figure. 6.9 (bottom row) shows the values of $\mathcal{F}|_{V_{\text{set}}}$ obtained: they are all compatible and average to 0.48 ± 0.01 and 0.62 ± 0.02 for the negative and positive polarisation, respectively. The resulting photoconductive gains are

$$\begin{aligned} \mathcal{G}^- &= 1.06 \pm 0.05 \\ \mathcal{G}^+ &= 1.36 \pm 0.06 \,, \end{aligned}$$

for the negative and positive polarisation, respectively. The value of the gain obtained with the negative polarisation bias is compatible with unity; that with the positive polarisation is larger than 1, but it should be reminded that this polarisation present unstable output current values. They are both consistent with corresponding gains obtained in Sect. 5.7 with the β radiation.

6.7.1 Configuration with the aluminium cover

The good agreement between the values of the gain measured with β and X radiations builds confidence on the novel method to study the sensor response. The measurement has been carried out for the sensor DC01 in the simple configuration without aluminium cover. It can be extended to estimate the gain of the other diamond sensors (which have the aluminium cover glued on the surface). I use Eq. 6.12 to calculate the gain. In this case, I consider as a reference the silicon diode equipped with the same cover shielding of the diamond detectors, to ensure similar configurations. This should reduce the dependence on potential systematic uncertainty introduced by the additional aluminium layer. The gain is estimated for the sensors DC01 (adding the aluminium cover) and DC00. I exclude the sensor DC25 because it is affected by large hysteresis effects, as shown in the stability tests, which make the measurement of the gain not possible. Despite a better behaviour, also the sensor DC15 presents some hysteresis (see Fig. 6.4) and the output currents in the linearity measurements have large fluctuations due to instabilities. The data collected with this sensor in the linearity measurements are not enough for a complete analysis, and additional samples at different values of V_{set} should be collected. For this reason, it's not possible to compute a value of the gain also for this sensor.

Figure 6.10 shows the values of $\mathcal{F}$ for the sensor DC01 and DC00 as a function of the voltage V_{set} applied to the X-ray source. I split the results according to the polarisation bias. The results are roughly constant as a function of V_{set} for both polarisation biases, although for the sensor DC01 the values group into two pairs at low and high V_{set}, which differ by about 10% between them. The spread could be due to instabilities of the output currents with the positive polarisation bias observed for the sensor DC01 (see Fig. 6.3). Unfortunately, the measurements with the aluminium cover have been carried out only with this polarisation bias, and no comparison can be done with the other polarisation, which should have a more stable response.

The results at different V_{set} are averaged for each sensor and they are shown as lines in Fig. 6.10. From these averages of $\mathcal{F}$, I calculated the gain shown in Fig. 6.11. I observe that:

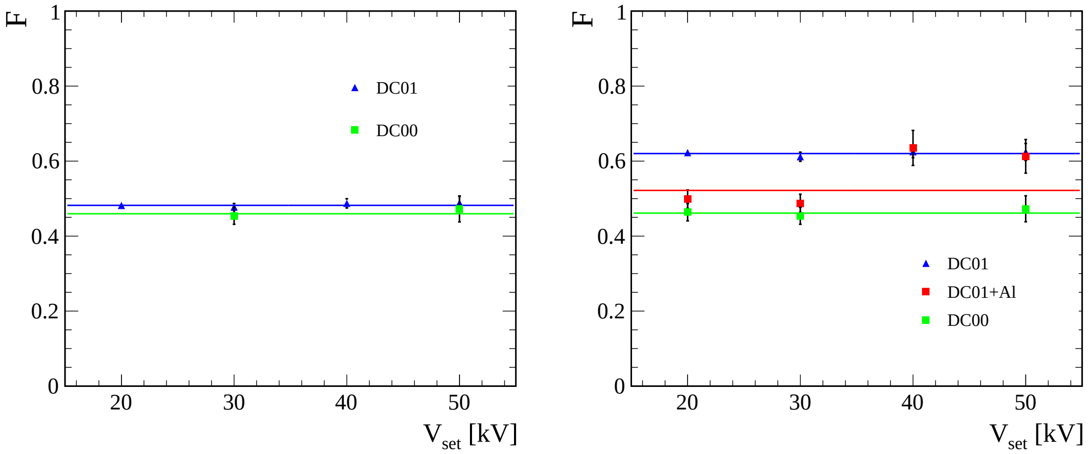

Figure 6.10: Measured values of $\mathcal{F}$ for the different diamond sensors as a function of V_{set} of the X-ray source, for the (left) negative and (right) positive polarisation. The triangular marker corresponds to the sensor DC01 without the aluminium cover; square markers are used for the sensors with the aluminium cover.

DC01 the measurement of the gain in the configuration with the aluminium cover is compatible with the value obtained without the cover. The measured gains agree with those obtained from the irradiation with the β source. The gains measured using a positive bias voltage are larger than one, and they differ from that obtained with a negative polarisation bias. With this latter polarisation, the measured gain is compatible with one.

DC00 the values of the gain obtained with opposite polarisation biases is the same, and this confirms the very symmetric response of this sensor. The gain agrees with one.

The value of the gains obtained with the sensor equipped with the aluminium cover are reported in the Table. 6.1.

Sensor	Bias [V]	$\mathcal{G}$
DC01 (with cover)	+100	1.18 ± 0.07
DC00	+100	1.02 ± 0.07
	−100	1.02 ± 0.08

Table 6.1: Estimated photo-conductive gains for the diamond sensors DC00 and DC01 in the configuration with the aluminium cover.

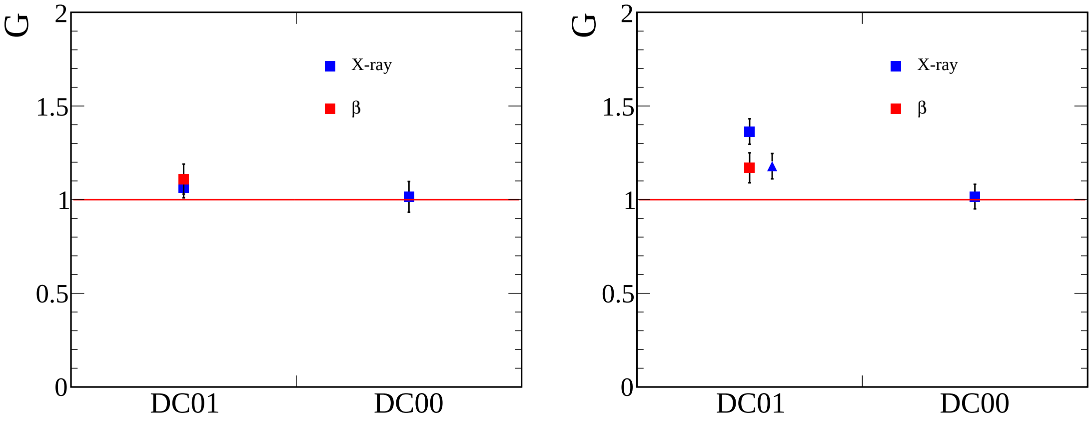

Figure 6.11: Measured values of gain for the different diamond sensors, for the negative (left) and positive (right) polarisation. The red marked represents the measurement performed with β radiation, while the blue marker the measurements performed with X-ray radiation. The triangular marker represents the value of gain obtained for the DC01 with the aluminium cover.

Chapter 7

Summary of the characterisation

This chapter summarises the main results of the characterisation of the diamond sensors with the three types of radiation used in my work. First, I draw some general considerations; then, I gather together the results for each sensor.

7.1 General considerations on the diamond-sensor response

In general, I observed that the sensors present a variety of responses, which ultimately strongly depend on the features of each specific crystal, such as its purity and defects. Surface effects and metal contacts might play an important role too, but are more difficult to investigate.

With the α radiation, I observed a "trap polarisation" effect pointed out by a deviation of the pulse-shape from that expected. This is the consequence of a "trapping" of the charge carriers at local defects of the crystal, which deforms the electric field inside the diamond bulk and sculpt the pulse shape.

Trapping effect are also observed in the analysis of the output current from the sensors irradiated with the β and X radiation. Measurements carried out with these two types of radiation, despite the different mechanism of charge-carrier generation, highlight a coherent picture and give consistent results. From the the test of the stability of the output current, the sensors can be classified in three categories according to their response with a given polarisation bias: class A, B and C.

Class A sensors are those that present a stable output current at least with a polarisation bias of a given sign, that is defined as its best polarisation. When the response is symmetric for both polarisation signs, the diamond sensor is close to an ideal crystal.

Class C sensors deliver an unstable current, which depends on the previous history of applied biases and of irradiation, and varies according to different hysteresis loops. Such hysteresis effects might be due to energy levels in the band gap that act as capture and emission centers, enhancing or decreasing the output current as they trap or release charge carriers.

Class B sensors present an intermediate behaviour, delivering quasi-stable currents after absorbing a certain amount of radiation. This type of sensors, when irradiated with a continuous flux of particles, present a transient time to converge to a stable value, attributed to the trapping centers in the band gap. Therefore, to study sensors proprieties, a stability measurement must be performed first.

7.2 Summary by diamond sensor

The results from the characterisation is summarised for each diamond sensor. All studies with β and X radiation are done with $V_{\text{bias}} = \pm 100\,\text{V}$.

DC01 I carried out a complete characterisation of this sensor. With the TCT method, I obtained an average energy to create an electron-hole pair of $\epsilon_{e/h} = 13.1 \pm 0.1\,\text{eV}$, which is in very good agreement with the known value for diamond (13 eV). I also measured the mobility and drift velocity of electrons and holes and I found values consistent with those present in literature. Stability measurements show that this is a reliable sensor (class A) when a negative bias is applied. The gain in this case is $\mathcal{G} = 1.06 \pm 0.05$.

DC00 This sensor shows very stable output current and a symmetric response for bias voltages of opposite sign. It is classified as a class A sensor for both polarities. The measured gain, average of the values obtained with the opposite polarisation biases, is $\mathcal{G} = 1.02 \pm 0.06$.

DC15 This sensor presents sizeable hysteresis effects with polarisation biases of both sign. However, it is classified as a class B sensor since for both polarisation it delivers a stable current after being irradiated for a certain period of time (typically $\mathcal{O}(100\,\text{s})$). It was not possible to estimate its gain because further measurements are necessary.

DC25 This sensor is classified as unreliable (class C), since the delivered output current is very unstable and strongly depends on the bias voltage. No analysis to measure the gain has been carried out for this sensor.

Table 7.1 summaries these results.

	DC00	DC01	DC15	DC25
Class	A	A	B	C
Best polarisation	symmetric	negative	–	–
Gain at $\lvert V_{\text{bias}}\rvert = 100\,\text{V}$	1.02 ± 0.06	1.06 ± 0.05	–	–

Table 7.1: Summary of the characterisation for all tested diamond sensors. The gain is reported for the best polarisation; if the response is symmetric, the average is computed.

Conclusions

The Belle II experiment will be soon one of the leading facilities at the intensity frontier: collecting data for about 10 years, it will accumulate 50 times more particle collisions than its predecessor, the Belle experiment. The large data set, containing about 50 billion B-meson pairs and similar numbers of charm mesons and tau leptons, will enable Belle II to test the flavour sector of the standard model at a much deeper level than was previously possible. To achieve such an ambitious target, the SuperKEKB accelerator is designed to reach unprecedented peak luminosities. High beam intensities are needed to maximise particle-production rates, generating high-radiation backgrounds from the machine as a drawback. This harsh environment may degrade the reconstruction performances of the vertex detector, the Belle II core. In order to protect the silicon detector from high-radiation doses, the Trieste Belle II group developed and installed a system based on single-crystal artificial-diamond detectors that monitors the radiation doses near the interaction region, triggering protective actions when needed. This system has been proving itself crucial for running the experiment in safe conditions while enhancements of the accelerator performance are underway. The collaboration intends to upgrade the monitoring system in 2022, and between 8 and 10 new diamond detectors has to be assembled and characterised by then.

My thesis represents a preparatory work in view of this upgrade. I deepened and improved the methods used to characterise the diamond sensors for the upgrade, by performing an in-depth study of four detectors (DC00, DC01, DC15, DC25). I exploited three types of radiation: α and β particles, and X-rays. This is the first time that X-rays are used in such a characterisation. I employed a novel method to characterise the diamond-sensor response to β and X radiation, which exploits a silicon diode used as a reference to minimise systematic uncertainties due to the poor knowledge of the radiation sources. In each study with the different radiations, I wrote a detailed simulation of the experimental setup to be compared with data.

With α particles, I determined the transport properties of the charge carriers using the transient-current-technique. Comparing data and simulation, I estimated the mean energy to create an electron-hole pair. I improved over the simulation model previously used in this respect. With β and X radiations, I inferred specific information on each sensor, such as the dependence on hysteresis loops and trapping effects. Studying the output current as a function of irradiation time for opposite polarisation biases, I classified the diamond detectors in three categories, according to the stability of the response and the best polarisation bias.

The sensor DC00 presents a very stable output current, symmetric for opposite biases of same magnitude, with a response close to that of an ideal crystal. The sensor DC01 delivers a stable output current only for a negative polarisation bias. The sensors DC15 and DC25 are instead affected by instabilities which depend on the previous irradiation history and on the bias voltage applied. Further measurements are envisioned to complete the picture for these sensors.

For the sensor DC00 and DC01, I estimated the photoconductive gain for a bias voltage of ±100 V, assuming a full charge-collection efficiency. This gain is defined as the ratio between the charge collected at the electrodes and the charge generated by radiation inside the active volume of the detector. I found values consistent with one, smaller than those observed in Ref. [39] for other diamond sensors irradiated with the same β source, and with the same bias voltages applied. I performed the study with α particles with the sensor DC01, the sole detector for which this source can be employed (all others are shielded from α radiation by the packaging cover glued on the surface). All results found for the charge-carriers mobility and drift velocity, and for the average electron-hole-creation energy, are consistent with those present in literature.

These results represent important steps forward in the characterisation techniques for diamond sensors to be used for the upgrade of the Belle II radiation monitor.

Appendices

Appendix A

Linearity fit results

Configuration	V_{set} [kV]	$m(\times 10^{-6})$	q [pA]
silicon diode witout cover	10	2.03 ± 0.01	0.52 ± 0.32
	20	33.1 ± 0.3	3.23 ± 5.82
	30	90.7 ± 1.4	-6.44 ± 2.07
	40	139 ± 3	14.1 ± 33.9
	50	165 ± 6	65.2 ± 48.5
silicon diode with cover	10	0.119 ± 0.002	0.47 ± 0.12
	20	8.67 ± 0.06	2.1 ± 1.4
	30	30.7 ± 0.7	-7.98 ± 8.04
	40	48.1 ± 2.9	26.5 ± 22.2
	50	62.5 ± 3.7	27.9 ± 28.9

Table A.1: Results of the fit with the function $y = mx + q$ on the silicon diode linearity plot.

Configuration	V_{set} [kV]	Polarity	$m(\times 10^{-8})$	q [pA]
DC00 with cover	10	−100 V	1.6 ± 0.1	0.54 ± 0.13
	20	+100 V	86.3 ± 0.7	0.52 ± 0.20
	30	−100 V	268 ± 2	0.8 ± 0.7
		+100 V	268 ± 2	0.6 ± 0.6
	50	−100 V	548 ± 5	3.8 ± 1.3
		+100 V	548 ± 5	3.0 ± 1.3

Table A.2: Results of the fit with the function $y = mx + q$ on the diamond DC00 linearity plot.

Configuration	V_{set} [kV]	Polarity	$m(\times 10^{-8})$	q [pA]
DC01	10	-100 V	46.7 ± 0.3	-0.0009 ± 0.0082
		$+100$ V	55.7 ± 0.3	-0.96 ± 0.06
	20	-100 V	480 ± 3	0.7 ± 0.8
		$+100$ V	619 ± 4	-0.9 ± 0.8
	30	-100 V	1159 ± 8	1.1 ± 1.9
		$+100$ V	1485 ± 10	2.42 ± 2.44
	40	-100 V	1753 ± 12	2.91 ± 2.95
		$+100$ V	2249 ± 15	4.4 ± 3.7
	50	-100 V	2069 ± 14	8.8 ± 3.5
		$+100$ V	2645 ± 18	13.1 ± 4.4
DC01 with cover	10	$+100$ V	2.22 ± 0.02	-0.003 ± 0.009
	20	$+100$ V	92.8 ± 0.6	0.21 ± 0.15
	30	$+100$ V	287 ± 2	-0.26 ± 0.48
	40	$+100$ V	570 ± 4	-0.33 ± 0.95
	50	$+100$ V	711 ± 5	2.5 ± 1.2

Table A.3: Results of the fit with the function $y = mx + q$ on the diamond DC00 linearity plot, for the configuration with and without cover.

Configuration	V_{set} [kV]	Polarity	$m(\times 10^{-8})$	q [pA]
DC15 with cover	10	-100 V	4.87 ± 0.13	0.13 ± 0.06
	30	-100 V	329 ± 3	8.27 ± 0.8
	50	-100 V	644 ± 7	13.8 ± 1.8
		$+100$ V	865 ± 7	6.6 ± 2.0

Table A.4: Results of the fit with the function $y = mx + q$ on the diamond DC15 linearity plot.

Bibliography

[1] Particle Data Group, M. Tanabashi *et al.*, *Review of particle physics*, Phys. Rev. D **98** (2018) 030001.

[2] M. Thompson, *Modern particle physics*, Cambridge University Press, (2013).

[3] M. S. Sozzi, *Discrete symmetries and $\mathcal{CP}$ violation: from experiment to theory*, Oxford University Press, 1st ed., 2008.

[4] M. S. Sozzi, *Lectures on $\mathcal{CP}$ violation*, Università di Pisa, 2010.

[5] G. Raven, *Lectures on $\mathcal{CP}$ violation*, CERN Summer student lectures, 2010.

[6] J. H. Christenson *et al.*, *Evidence for the 2π decay of the k_2^0 neson*, Phys. Rev. Lett. **13** (1964) 138.

[7] N. Cabibbo, *Unitary symmetry and leptonic decays*, Phys. Rev. Lett. **10** (1963) 531.

[8] M. Kobayashi and T. Maskawa, *$\mathcal{CP}$-violation in the renormalizable theory of weak interaction*, Prog. Theor. Phys. **49** (1973) 652.

[9] CKMfitter Group, J. Charles *et al.*, *$\mathcal{CP}$ violation and the CKM matrix: assessing the impact of the asymmetric B factories*, Eur. Phys. J. C **41** (2005) 1, `arXiv:hep-ph/0406184`, updated plots available at: `http://ckmfitter.in2p3.fr/www/html/ckm_results.html`.

[10] E. Kou *et al.*, *The Belle II physics book*, arXiv e-prints (2018) 574, `arXiv:1808.10567`.

[11] LHCb Collaboration, *Letter of intent for the LHCb upgrade*, CERN-LHCC-2011-001 (2011).

[12] Y. O. et al. *Accelerator design at SuperKEKB*, Prog. Theo. Exp. Phys. **2013** (2013) 03A011.

[13] Raimondi *et al.*, *Beam-beam issues for colliding schemes with large Piwinski angle and crabbed waist*, arXiv e-print (2007) `arXiv:physics/0702033`.

[14] Belle II Collaboration and B2TiP theory Community, *The Belle II physics book*, Prog. Theor. Exp. Phys., 1st ed., 2018.

[15] Belle II Collaboration, T. Abe *et al.*, *Belle II Technical Design Report*, ArXiv e-prints (2010) `arXiv:1011.0352`.

[16] Belle-II SVD Collaboration, K. Adamczyk *et al.*, *The Belle II silicon vertex detector assembly and mechanics*, Nucl. Instrum. Meth. **A845** (2017) 38.

[17] DEPFET, C. Marinas, *The Belle II pixel detector: high precision with low material*, Nucl. Instrum. Meth. **A731** (2013) 31.

[18] Belle II Collaboration, N. Taniguchi, *Central Drift Chamber for Belle-II*, JINST **12** (2017) C06014.

[19] K. Inami and I. Belle, *Top counter for particle identification at the belle ii experiment*, Nuclear instruments and methods in physics research section A: accelerators, spectrometers, detectors and associated equipment **766** (2014) 5.

[20] S. Iwata *et al.*, *Particle identification performance of the prototype aerogel RICH counter for the Belle II experiment*, PTEP **2016** (2016) 033H01, `arXiv:1603.02503`.

[21] V. Aulchenko *et al.*, *Electromagnetic calorimeter for Belle II*, J. Phys. Conf. Ser. **587** (2015) 012045.

[22] Belle Collaboration, A. Abashian *et al.*, *The K-L/mu detector subsystem for the BELLE experiment at the KEK B factory*, Nucl. Instrum. Meth. **A449** (2000) 112.

[23] P. M. Lewis *et al.*, *First measurements of beam backgrounds at SuperKEKB*, arXiv e-prints (2018) `arXiv:1802.01366`.

[24] The momentum acceptance is defined as the maximum energy excursion that an accelerated particle can have before it is lost from the machine. .

[25] The equation that describes the scattering probability is known as Bruck's formula and it is derived in H. Bruck, *Circular Particle Accelerators*, Los Alamos Scientific Laboratory, 1st ed., 1972.

[26] L. Vitale, *The Belle II Silicon-strip Vertex Detector*, in *Vertex 2014*, 017, 2015.

[27] G. Lindström, *Radiation damage in silicon detectors*, Nucl. Instrum. Meth. A **512** (2003) 30.

[28] The dependence on the type and energy of particle is partially smoothed out by secondary interactions of primary knock-on atoms. .

[29] G. Lutz *et al.*, *Semiconductor radiation detectors*, Springer, 2nd ed., 1999.

[30] T. I. Meyer, *PIN photodiodes for radiation monitoring and protection in the BABAR Silicon Vertex Tracker*, Int. J. Mod. Phys. **A16S1C** (2001) 1084.

[31] V. Re *et al.*, *Radiation damage studies for the babar silicon vertex tracker*, Nucl. Instrum. Meth. A **549** (2005) 11 .

[32] D. Zontar, *Radiation monitoring at Belle*, Nucl. Instrum. Meth. **A501** (2003) 164.

[33] For a consistent derivation of a radiation hardness parameter that reflects the diamond radiation hardness capabilities see V. Grilj and others, *The evaluation of radiation damage parameter for CVD diamond*, Nucl. Instrum. Meth. B **372** (2016) 161.

[34] P. Bergonzo *et al.*, *Particle and radiation detectors based on diamond*, Phys. Status. Solidi A **185** (2001) 167.

[35] S. Koizumi *et al.*, *Physics and applications of CVD diamond*, Wiley, 1st ed., 2008.

[36] Diamond crystals are produced by *Element 6* while electrodes by *Cividec.*

[37] K. C. Kao, *Dielectric phenomena in solids*, Elsevier, 1st ed., 2004.

[38] S. M. Sze and K. K. Ng, *Physics of semiconductor devices, third edition, p. 669*, Wiley, 2007.

[39] G. Bassi, *Radiation monitor with diamond sensors for the Belle II experiment at SuperKEKB*, A. A. 2017–2018.

[40] P. W. May, *Diamond thin films: a 21st-century material*, Philos. T. R. Soc. A **358** (2000) 473.

[41] R. S. Muller and T. I. Kamins, *Device electronics for integrated circuits*, Wiley, 3rd ed., 2002.

[42] E. Berdermann, in *Diamond for particle and photon detection in extreme conditions*, p. 407–467, Elsevier Science, 2014.

[43] R. S. Sussmann, *CVD diamond for electronic devices and sensors*, Wiley, 1st ed., 2009.

[44] H. Pernegger *et al.*, *Charge-carrier properties in synthetic single-crystal diamond measured with the transient-current technique*, J. Appl. Phys. **97** (2005) 073704.

[45] Caen, *CAEN DT5521HM*, 2015.

[46] Particulars, *Particulars Bias-T*, 2015.

[47] Particulars, *Particulars wide band current amplifiers*, 2015.

[48] LeCroy, *LeCroy Wavepro 960*, 2002.

[49] W. Shockley, *Currents to conductors induced by a moving point charge*, J. Appl. Phys. **9** (1938) 635.

[50] M. Rebai *et al.*, *Time-stability of a single-crystal diamond detector for fast neutron beam diagnostic under alpha and neutron irradiation*, Diamond and related materials **61** (2016) 1 .

[51] A. Ferrari *et al.*, *FLUKA: a multi-particle transport code*, CERN, program version 2005 ed., 2005.

[52] E. Konorova and S. Kozlov, *Nuclear radiation detector made of diamond*, Sov. Phys. Semicond. **4** (1971) 1600.

[53] Elettra Sincrotrone Collaboration, *Ah501b picoammeter*, `http://ilo.elettra.trieste.it/index.php?page=_layout_prodotto&id=394&lang=en`.

[54] Amptek, Inc. , *Mini-x2 user manual*, `https://www.amptek.com/products/x-ray-sources/mini-x2-ray-tube`.

[55] The Center for X-Ray Optics - Lawrence Berkeley National Laboratory, `https://www.nist.gov/`.